ROOM SOUND FIELD PREDICTION BY ACOUSTICAL RADIOSITY

by

Eva-Marie Nosal

B.Sc. (Pure Mathematics), The University of Calgary, 2000
B.Sc. (Applied Mathematics), The University of Calgary, 2000
B.Mus. (Piano performance), The University of Calgary, 2000

A THESIS SUBMITTED IN PARTIAL FULFILLMENT OF
THE REQUIREMENTS FOR THE DEGREE OF

MASTER OF SCIENCE

in

THE FACULTY OF GRADUATE STUDIES

(Department of Mathematics)

We accept this thesis as conforming
to the required standard

THE UNIVERSITY OF BRITISH COLUMBIA

December 2002

Eva-Marie Nosal

Department of Mathematics

The University of British Columbia
Vancouver, Canada

Date December 19, 2002

ABSTRACT

Acoustical radiosity is a technique based on assumptions of diffuse reflection and incoherent phase relationships that has been used to predict room sound fields. In this research, the background to acoustical radiosity is given, the integral equation (on which the technique is based) is derived, and a numerical solution is detailed for convex rooms of arbitrary shape. Several validations are made by comparison of the numerical solution to (1) analytical solutions for a sphere; (2) results from a ray tracing algorithm in cubical enclosures, and; (3) measurements in three real rooms.

TABLE OF CONTENTS

LIST OF TABLES

LIST OF FIGURES

To my parents.

Who gave me music and who gave me math.

But most beautifully -

Who let me play!

CHAPTER 1

Introduction

1.1 Room sound field prediction

People have been attempting to understand and predict the behavior of sound in rooms for nearly a hundred years. The prediction of sound fields in enclosures is needed for design purposes, such as the adjustment of classrooms and lecture halls for intelligibility, of concert halls, recording studios, and theatres for sound quality, of workrooms for minimized noise levels, of offices for privacy, and so on. Also, as computer simulations become increasingly popular for entertainment and training purposes, fast and accurate room acoustical modeling techniques are required.

Initial attempts at understanding room acoustics used physical models (including ultrasonic, ripple tank, and optical methods) and scale models [51]. The wave equation model, in which the wave equation is solved for boundary conditions imposed by the enclosure, gives very accurate results. Typically, finite element methods and boundary elements methods are used in the solutions. Unfortunately, the wave equation method is often impractical, particularly for large and/or irregularly shaped rooms with complex boundary conditions and at high frequencies (due to an increase in the number of modal frequencies). A greatly simplified approach to room acoustics is through 'geometrical-acoustics' models, according to which sound waves are replaced by sound rays which have energy but not phase [13,36]. They can be accurate at middle and high frequencies. Because of the relatively good trade-off between accuracy and complexity (particularly with the use of computers) and the fact that many important perceptual effects mainly involve mid to high frequencies, geometrical models have been used extensively in room acoustics over the past forty years. Geometrical room acoustics includes statistical models (notably diffuse field theory), the image source model, particle, ray, cone, and beam tracing

models, acoustical radiosity, and hybrid models (which combine two or more models). Information on all of these models is readily available in the literature on acoustics.

The key concern of any sound field prediction method is the prediction of the impulse response at a given receiver position. This is just the output signal at the receiver position to an impulsive sound signal radiated from a source in the room (see definition in Appendix A). Once the impulse response is known, the response to any other input signal can be found. The first non-zero peak of the impulse response normally corresponds to the direct sound – that is, the sound that propagates from the source directly to the receiver without interaction with any surfaces in the enclosure. The direct signal is usually followed by several smaller signals, called low-order reflections, that correspond to sound that has reflected one or more times from the boundaries of the enclosure. After these initial signals, a multitude of signals that have been repeatedly reflected from the boundaries arrive at the receiver. This is called reverberation. As time progresses, arriving signals have decreasing amounts of energy, causing sound decay. If the signals are plotted against time by horizontal lines with length corresponding to the magnitude of the signal, we can visualize the impulse response. If the plotted magnitude is scaled or squared to represent squared pressure, such visualization is known as an echogram. The echogram contains much of the significant information about the sound field for the receiver position in the room. From the echogram, numerous room acoustical parameters can be found. Examples of such room acoustical parameters are steady state sound pressure level (*SPL*), strength (*G*), reverberation time (*RT*), early decay time (*EDT*), center time (*TS*), clarity (C_{80}), and definition (D_{50}), all of which are defined in Appendix A. These parameters have been developed by researchers in room acoustics as quantitative measures that correlate [8] with subjective judgment of sound fields. They are often used in the evaluation of room acoustical predictions methods.

To predict impulse responses, a room acoustical mode relies on knowledge about the physical characteristics of the enclosure. One such characteristic is the absorptive properties of the surfaces, which are described by their absorption coefficient. This coefficient is just the proportion of sound energy incident on the surface that is absorbed. As we shall see in the experimental section of this thesis, absorption coefficients are often difficult to estimate. Energy that is not absorbed is either transmitted through the surface or reflected back into the enclosure. Reflection can occur specularly, semi-diffusely, or diffusely. Specular reflection describes the case in which sound energy incident on a surface is reflected at an angle equal to the angle of

Figure 1.1. Specular, semi-diffuse, and diffuse reflection.

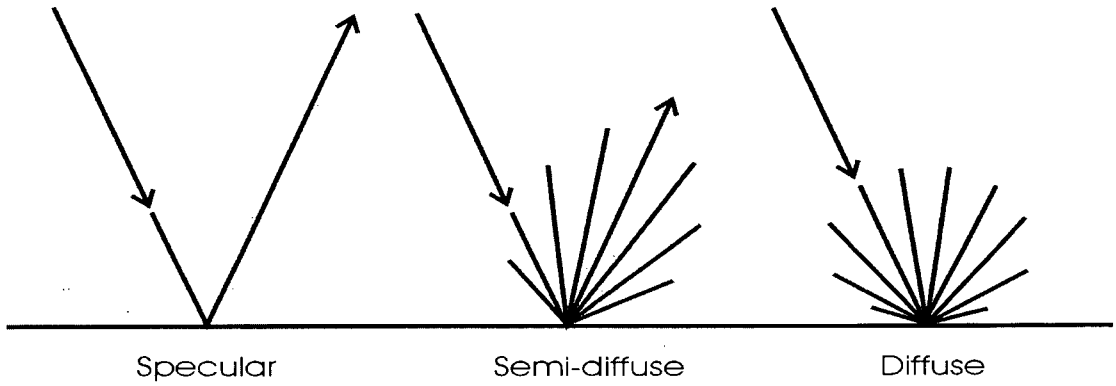

incidence, as might be expected for smooth, hard surfaces. For surfaces with irregularities, such as bumps or grooves that are of similar or smaller size than the wavelength of sound in question, sound will be scattered in many directions upon incidence. If it is reflected completely randomly, the reflection is called diffuse; otherwise, it is semi-diffuse. See Figure 1.1. Assumptions about the way sound is reflected from the surfaces must be made, and different methods of prediction make different assumptions.

This thesis explores a geometrical sound field prediction method that assumes perfectly diffuse reflection. We call this method acoustical, or time-dependent, radiosity. The method has been previously called in various ways, including 'the integral equation method' [36], 'radiant exchange' [41], and 'an intensity-based boundary element method' [17]. The name 'acoustical radiosity' is taken from a similar (time-independent) technique used in computer graphics, where it is simply called radiosity.

1.2 History and literature review

Called 'radiative transfer theory', radiosity was initially introduced in illumination engineering in the 1920's by photometric theorist, Yamauti [65]. Without computers to carry out the lengthy calculations, however, the potential of the method could not be realized at that time. The technique was rediscovered and further developed by the thermal engineering community in the 1950s and 1960s [57,62]. It was referred to as 'radiosity' or 'radiation heat transfer' (among other names). Radiosity was introduced as a technique in computer graphics in the 1980's and has since become one of the leading global illumination techniques for realistic image synthesis [2,12]. The computer graphics community has developed many efficient methods for

implementing radiosity, and the success of the technique in that field has prompted the use of radiosity in other fields.

The first formulation of the radiosity technique in acoustics was made by Kuttruff in the early 1970's [30,31,36] in the form of an integral equation (see Section 2.3). In the late 1970's, some of the first papers published on acoustical radiosity developed the theory and presented analytical solutions in spheres, both for the steady state sound field [11] and for sound decay [10,28].

A fast, iterative method for finding reverberation time from the integral equation and the assumption of exponential decay was proposed in 1980 by Gilbert [18], and implemented by Schroeder and Hackman [54]. In 1995, Kuttruff presented an even easier approach [34,35] and also developed a method, based on the integral equation, to find the sound absorption coefficient of a test sample from reverberation time [33]. In the same year, Kuttruff [32] published the solution to his steady-state integral equation for flat enclosures (in which side walls are neglected). Also included were comparisons to experimental data.

In 1984, Miles [45] was the first to apply a numerical solution of the integral equation to rectangular rooms. In his paper, Miles gives a detailed account of his iterative solution, and deals with both steady state and time-varying sources. Moreover, by finding poles and zeros of the Laplace transform of the integral equation, Miles proved that decay curves in rooms with diffusely reflecting boundaries are exponential. Moore's Ph.D. thesis, entitled "An approach to the analysis of sound in auditoria" (Cambridge, UK, 1984) is referred to by several authors [9,41] as containing a theoretical development of acoustical radiosity, but the thesis could not be obtained for reference. A 1993 paper by Lewers [41] used acoustical radiosity to model the diffuse reverberant tail of the impulse response in a hybrid model. Some details are given in his paper, as well as minimal results. Another 1993 paper, by computer scientists Shi, Zhang, Encarnação, and Göbel [56], outlined an algorithm for acoustical radiosity, although no details were given. Two comparisons of predicted with measured reverberation times were found to be close, but no other comparisons were made. More recently, Tsingos [63] used acoustical radiosity to simulate sound fields for interactive graphics applications. Tsingos used hierarchical methods from radiosity in computer graphics, suggested the incorporation of specular reflection into the model, and gave results for a validating case.

In 2000, Le Bot and Bocquillet [40] did a thorough comparison of steady state sound pressure level predictions by acoustical radiosity and ray by tracing with diffuse reflection. Their work included numerical comparisons and an analytical proof of the equivalence of the two methods. Also in 2000, Kuttruff [37] combined the image source method and analytical solutions to the integral equation to explore the steady state sound propagation in non-empty, flat rooms. Kang's work [29] used radiosity to investigate the propagation of sound in long enclosures with diffusely reflecting boundaries. Franzoni, Bliss, and Rouse [16,17] gave a theoretical development of acoustical radiosity with a slightly different approach. Validations for a steady-state, two-dimensional model problem were given by comparison to exact solutions found by solving the wave equation. Other recent work relevant to acoustical radiosity includes that by Alarcão and Coelho [1].

An interesting paper by Rougeron, Gaudaire, Gabillet, and Bouatouch [52] from 2002 describes a time-dependent radiosity method to simulate the propagation of a 60 GHz electromagnetic wave in an enclosure. Their method is fast, requires little memory, and was validated in two rooms. A similar approach might be applied to acoustical radiosity. Very recently, Le Bot [39] published a paper, in which the integral equation is replaced by a functional equation, which aims to model specular reflection with an adapted radiosity method.

1.3 Why acoustical radiosity?

Even though several authors have explored some of the problems and potential of acoustical radiosity, the technique has never become popular in room acoustics. Possible reasons for the poor reception of radiosity into the acoustical community include the seemingly prohibitive computational costs and the limiting assumption of diffuse reflection. These limitations are discussed below.

The key difference between radiosity in acoustics and radiosity in computer graphics (or in any of the other fields in which it has been used) is time-dependence. Because sound, unlike light, travels so slowly through air that the time delay cannot be ignored, any model of sound in rooms must incorporate time. As we will see, the introduction of time dependence into radiosity is one of the limiting aspects of acoustical radiosity because of the high computational cost. Nevertheless, acoustical radiosity is promising in that the computational costs are incurred only in the initial 'rendering' of a room. In particular, once a room has been rendered for a given

Figure 1.2. Conversion of specularly to diffusely reflected sound energy.

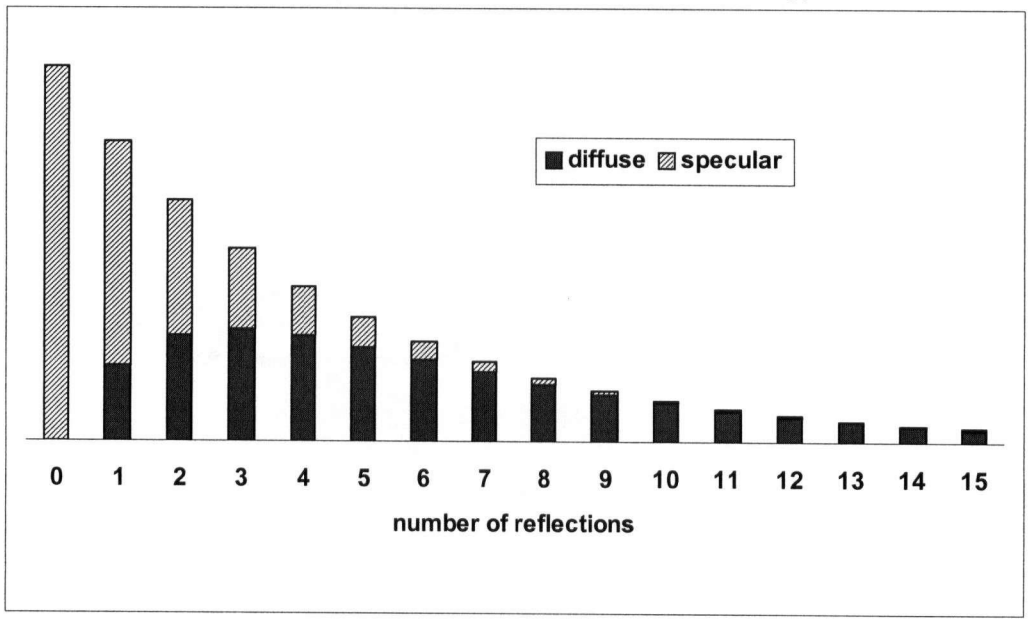

source, the remaining costs are low enough to enable real-time sound field simulation for moving receivers. This 'view-independence' is the major advantage of radiosity, particularly for interactive simulations. Furthermore, there are possible methods to accelerate the initial rendering [52,63]. If they can be developed, such methods would certainly make acoustical radiosity much more accessible to room acousticians.

The assumption of diffuse reflection may not be as limiting as it initially seems. It has been suggested [34,35] that the assumption of diffuse reflection is less restrictive than the assumption of specular reflection that is commonly made in geometric-acoustical prediction methods. It is definitely less restrictive than the assumption of a diffuse field that is still so popular among room acousticians (because of its simplicity). Further, it is not clear how the assumption of diffuse reflection actually affects a sound field, and indeed some characteristics of the field may not be sensitive to a change from specular to diffuse reflection [21]. Acoustical radiosity may be an effective predictor of such characteristics.

Certainly, it is likely that acoustical radiosity is highly effective in predicting the late part of a decay curve. It has been shown that the conversion of specular energy into diffuse energy is irreversible and that all walls produce some diffuse reflection [22]. Hence, though the initial reflections in a room may be more specular than diffuse, most of the energy in the sound decay of a room will consist of higher-order, diffuse reflections. As effectively shown in Figure 1.2

[34], after several reflections, nearly all energy has become diffusely reflecting. For this reason, there is strong reason to believe that the late part of decay curves should be well predicted by radiosity. For the figure, 75% and 25% of reflection were assumed to be specular and diffuse, respectively, and the boundary had a uniform absorption coefficient of 0.2.

Initial evidence for the effectiveness of radiosity in predicting the late part of decay curves has already been presented (for spherical [28] and rectangular [38] enclosures) by comparison of decay curves for rooms with relatively small amounts of diffuse reflection and diffusely reflecting walls. If radiosity is indeed effective in this regard, hybrid methods that account for the specular component by another method (such as ray tracing or the method of images) and the diffuse component by radiosity may be highly successful in predicting room sound fields. Such a model has been suggested by Lewers [41] and for rectangular enclosures by Baines [4]. Still, the effectiveness of radiosity in the prediction of the late part of the decay curve, as well as the prediction of other room characteristics, remains to be explored.

It should further be recognized that it may be possible to extend the acoustical radiosity methods outlined in this thesis to non-diffuse reflection. Such extensions have been made in computer graphics (for the time-independent cases) [53,58,59] and have been applied in a few time-dependent cases [22,52,63]. Such an extension was beyond the scope of this thesis, but is certainly of great interest.

1.4 Organization of thesis

Upon reviewing literature on acoustical radiosity, it became quite clear that a unified, consistent approach to the technique is not available. Indeed, there is not even a consensus about what the technique should be called, nor is it anywhere fully outlined. It was evident that the most beneficial starting point of this thesis would be a clear and thorough development of acoustical radiosity, starting from the basic definitions and derivations. This was done and is presented in Chapter 2.

A basic numerical algorithm relying on the discretization of the boundary and of time is developed and presented in Chapter 3. Solutions to some problems regarding the implementation of acoustical radiosity in non-rectangular enclosures are investigated in this chapter. Chapter 4 deals with the methods used to predict impulse responses, echograms, and room-acoustical parameters from the solutions.

The algorithm and methods presented in Chapters 3 & 4 were programmed and initial investigations into the applicability and validity of acoustical radiosity for predicting room sound fields were performed. Such validations are, for most part, absent from the literature, despite the fact that they are vital to our confidence in predicting sound fields in enclosures. The investigations are presented in Chapter 5. Chapter 6 is gives a summary of the work done and gives suggestions for future work.

CHAPTER 2

Theoretical development

2.1 Assumptions

Acoustical radiosity relies on several assumptions that are outlined in this section.

2.1.1 Diffuse reflection

The main assumption of acoustical radiosity is that all boundaries are diffusely reflecting. Diffuse reflection has been introduced in Chapter 1 and will be further discussed in Section 2.2. The assumption of diffuse reflection allows for major simplifications in the development of acoustical radiosity because it is 'memoryless'. In particular, the way that a ray is reflected is not dependent on the direction from whence it came. It has been shown that diffuse reflection is the only such memoryless reflection law [27].

2.1.2 Incoherent phase relationships

Another assumption on which acoustical radiosity depends (as do all geometric-acoustical prediction methods) is that of incoherent phase relationships between propagating waves [35]. In room acoustics, this assumption is usually sufficient, and may be justified when the wavelengths are small compared to the dimensions of the room. In particular, we consider Schroeder's 'large room limit' [55]

$$f_s = 2000\sqrt{\frac{RT}{V}} \qquad \text{(Hz)}$$

where RT is the reverberation time in seconds and V is the room volume. Above this limit, the density of eigen-frequencies is so high that a strong overlap of normal modes results. As a consequence, many modes are stimulated simultaneously. A nearly random distribution of phase

effects among the stimulated modes means that their phase effects will cancel when they are superimposed [35].

For large halls, f_s is typically around 20 – 30 Hz, with only 20 – 30 eigen-frequencies below f_s. In a small room, f_s is typically around 100 – 200 Hz, with 60 – 100 eigen-frequencies below f_s. Because the frequency range of interest is usually above Schroeder's limit, it is usually possible to neglect phase effects.

With this assumption, acoustical radiosity traces energy and neglects the effects of phase. As pointed out by Kuttruff [35], this does not unduly restrict prediction accuracy, because almost all common parameters in room acoustics - such as reverberation time, early decay time, clarity index, definition, center time, strength, and lateral energy fraction - are based on energy (or pressure squared) instead of on pressure. Echograms, decay curves, and steady state sound pressure levels are also functions of energy. An important exception is the inter-aural cross-correlation coefficient, which cannot be predicted by radiosity.

2.1.3 Other assumptions

In this thesis, several further simplifying assumptions are made, most of which would not be prohibitively difficult to relax. Reflection coefficients are taken to be independent of their angle of incidence, and diffraction effects are neglected. Also, the method is developed only for empty, convex enclosures. In addition, sources are assumed to be omni-directional (that is, they radiate sound with equal intensity in all directions) point sources.

2.2 Diffuse reflection

Diffuse reflection has been introduced in Chapter 1 and in Section 2.1.1 as one of the main assumptions of acoustical radiosity. In this section, we discuss Lambert's Law, which governs diffuse reflection. Then we develop formulas based on diffuse reflection that will be used to derive the integral equation in the next section.

2.2.1 Lambert's (Cosine) Law

Suppose a sound ray strikes an infinitesimally small, perfectly diffuse reflector, dS. If $I(\theta, R)$ is the intensity of the sound which is scattered by dS, in direction θ ($0 \le \theta \le \pi/2$) from the surface normal measured at distance R from the reflector, then

$$I(\theta, R) = I(0, R)\cos\theta . \tag{2.1}$$

In words, Lambert's Law states that the intensity transmitted in any direction varies as the cosine of the angle between the direction and the normal vector to the surface. We can think of Lambert's Law as forcing the 'viewed' intensity of the element dS to be constant with varying viewing direction. As θ increases, the observer (at angle θ and distance R from dS) 'sees' less of dS. In particular, the area seen (the projected area) varies as $\cos\theta$ (see Figure 2.1 for the two dimensional analogy), so it to appear that the intensity coming from the element is constant with varying θ, $I(\theta, R)$ must also vary as $\cos\theta$.

Note that the direction of the incident ray is not a variable in Lambert's Law, as stated above. This is what makes diffuse reflection 'memoryless', as discussed in Section 2.1.1. Also, it may be helpful to realize that this formulation of Lambert's Law may be different that that found in other sources (in particular, the formulation found in computer graphics). This can be explained by the different way in which intensity is defined in different fields, where it is sometimes defined using solid angles rather than using projected areas.

2.2.2 Intensity from radiation density

If we know the radiation density, B_0 (defined as the rate at which energy leaves a unit area of surface), of the differential element dS, then, from Lambert's Law, we can find $I(\theta, R)$ for any θ and R. Consider a hemisphere of radius R centered over dS. If no energy is lost

Figure 2.1. Projected length.

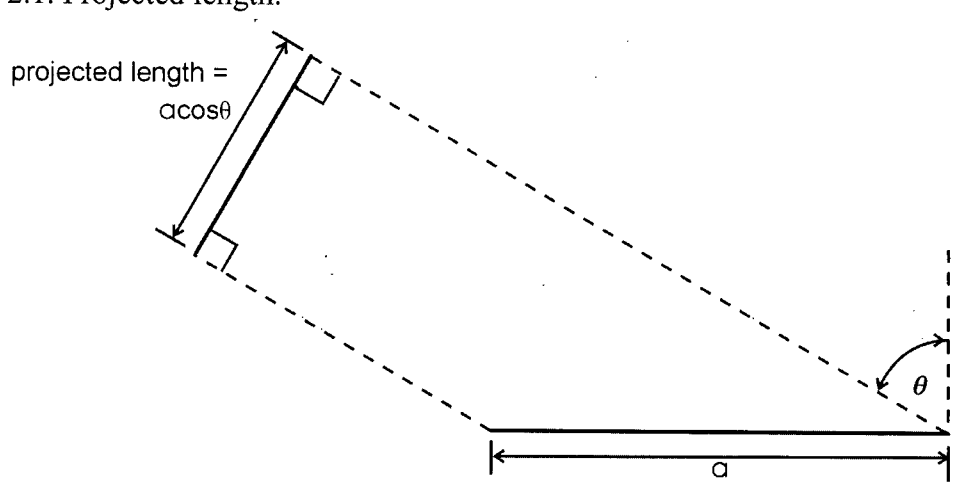

in propagation, then the rate of energy incident on this hemisphere from dS must equal the radiation density, B_0. In particular, we require that the surface integral of $I(\theta, R)$ over the hemisphere be equal to $B_0 dS$. In equations, we have

$$B_0 dS = \int_S I(\theta, R) d\sigma \tag{2.2}$$

where S is the hemisphere. We introduce a Cartesian coordinate system $\{(x,y,z)$ such that x, y, z are real$\}$ so that the wall element is centered at (0,0,0) and has normal (0,0,1), and note that all energy is emitted into the top half of the space ($z \geq 0$). Then

$$\cos\theta = \frac{z}{R}$$

so that, by Lambert's Law,

$$I(\theta, R) = \frac{I(0,R)z}{R}.$$

S can be parameterized by

$$s(u,v) = (R\cos u \cos v,\ R\sin u \cos v,\ R\sin v)$$

with $0 \leq u \leq 2\pi$ and $0 \leq \mathrm{v} \leq \pi/2$. We call this parameter set Ω. See Figure 2.2 [14]. We get

$$B_0 dS = \int_S I(\theta, R)\, d\sigma = \frac{I(0,R)}{R} \int_S z\, d\sigma = \frac{I(0,R)}{R} \int_\Omega z(u,v) \| N(u,v) \| du\, dv \tag{2.3}$$

Figure 2.2. Parametrization of a sphere.

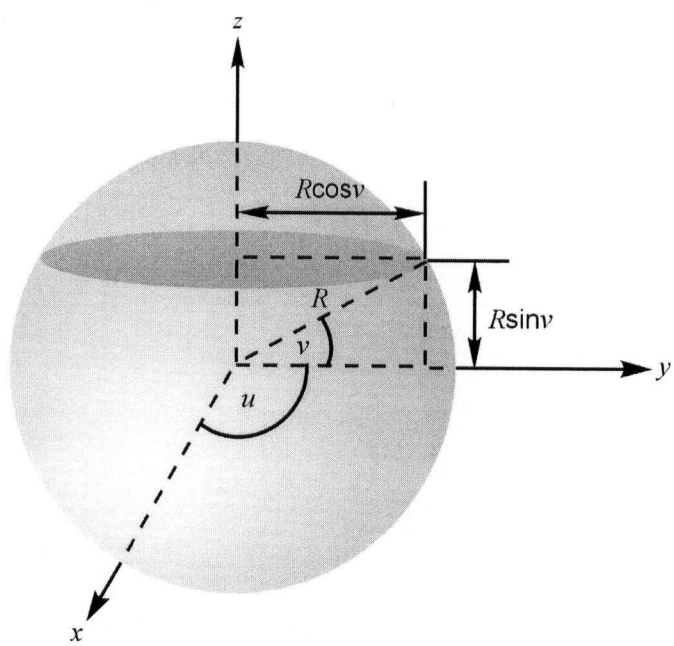

where $\|N(u,v)\|$ is the norm of $N(u,v)$, the fundamental vector product of *S*. - i.e.

$$N(u,v) = s_u' \times s_v' \ .$$

Here,

$$s_u' = \left(\frac{\partial x}{\partial u}, \frac{\partial y}{\partial u}, \frac{\partial z}{\partial u}\right) = \left(-R\sin u\cos v, R\cos u\cos v, 0\right)$$
$$s_v' = \left(\frac{\partial x}{\partial v}, \frac{\partial y}{\partial v}, \frac{\partial z}{\partial v}\right) = \left(-R\cos u\sin v, -R\sin u\sin v, R\cos v\right)$$

so that

$$N(u,v) = R\cos v(R\cos u\cos v, R\sin u\cos v, r\sin v) = R\cos v\ s(u,v)$$
$$\Rightarrow \quad \|N(u,v)\| = R^2\left|\cos v\right| = R^2\cos v$$

since $\left|\cos v\right| = \cos v$ for $0 \le \mathrm{v} \le \pi/2$. Hence, Eq. (2.3) becomes

$$B_0 dS = \frac{I(0,R)}{R}\int_{\Omega} z(u,v)R^2\cos v du dv$$
$$= \frac{I(0,R)}{R}\int_0^{2\pi}\left(\int_0^{\pi/2}(R\sin v)(R^2\cos v)du\right)dv$$
$$= 2\pi\frac{I(0,R)}{R}R^3\int_0^{\pi/2}\sin v\cos v dv$$
$$= \pi I(0,R)R^2 .$$

It follows that

$$I(\theta,R) = B_0\frac{\cos\theta}{\pi R^2}dS .$$

To account for air absorption, we need to include an air absorption term, $\exp(-mR)$, in the above equation above to get

$$I(\theta,R) = B_0 e^{(-mR)}\frac{\cos\theta}{\pi R^2}dS . \tag{2.4}$$

2.2.3 Intensity from incident intensity

Suppose that a bundle of parallel rays is incident on the differential wall element *dS*. If this bundle makes angle θ_0 to the element normal and has intensity I_0, then the irradiation density, defined as the rate at which energy is incident on a unit area of surface, is simply

$I_0 \cos\theta_0$. This is obvious from the definition of intensity, since a unit area normal to the direction of flow of energy projects an area of $1/\cos\theta_0$ onto the plane containing *dS*.

Assuming that the element *dS* has reflection coefficient ρ (assumed independent of incidence angle), the radiation density corresponding to the incident bundle of rays is

$$B_0 = \rho I_0 \cos\theta_0 . \tag{2.5}$$

Combining Eq. (2.4) and (2.5), we get

$$I(\theta, R) = I_0 e^{(-mR)} \rho \frac{\cos\theta \cos\theta_0}{\pi R^2} dS . \tag{2.6}$$

2.3 Integral equation

For completeness, the derivation of the integral equation for acoustical radiosity will be outlined here. It has been previously been derived by Kuttruff [36]; his work is the basis of the present derivation. However, this development differs from Kuttruff's in the definition of $B(r,t)$ (see below) and in the inclusion of air absorption.

2.3.1 Explanation and derivation

Consider an enclosure in which the whole boundary reflects diffusely. Within this enclosure, place a sound source and a receiver. We wish to predict the sound field at the receiver position. To do so, we mesh the boundary into differential elements, each of which is itself a diffuse reflector. Energy from the source propagates to the wall elements, and the radiation density due to the source is found for each element. The surface elements are considered to be secondary sources, each emitting energy diffusely to all of the other elements. This process continues, with elements receiving and emitting energy. The process can be modeled by an integral equation, from which the total intensities at the wall elements can be found. Once the element intensities are known, the sound field at the receiver can be found by propagating the energy 'emitted' by the patches to the receiver.

As was discussed in the introduction, an essential difference between radiosity in acoustics and radiosity in thermal heat transfer or in graphics is that the process is time dependent. The time that it takes for sound to travel from one element to another is not negligible, and it must be accounted for. As a result, our integral equation will be time dependent.

Figure 2.3. Illustration for the derivation of the integral equation.

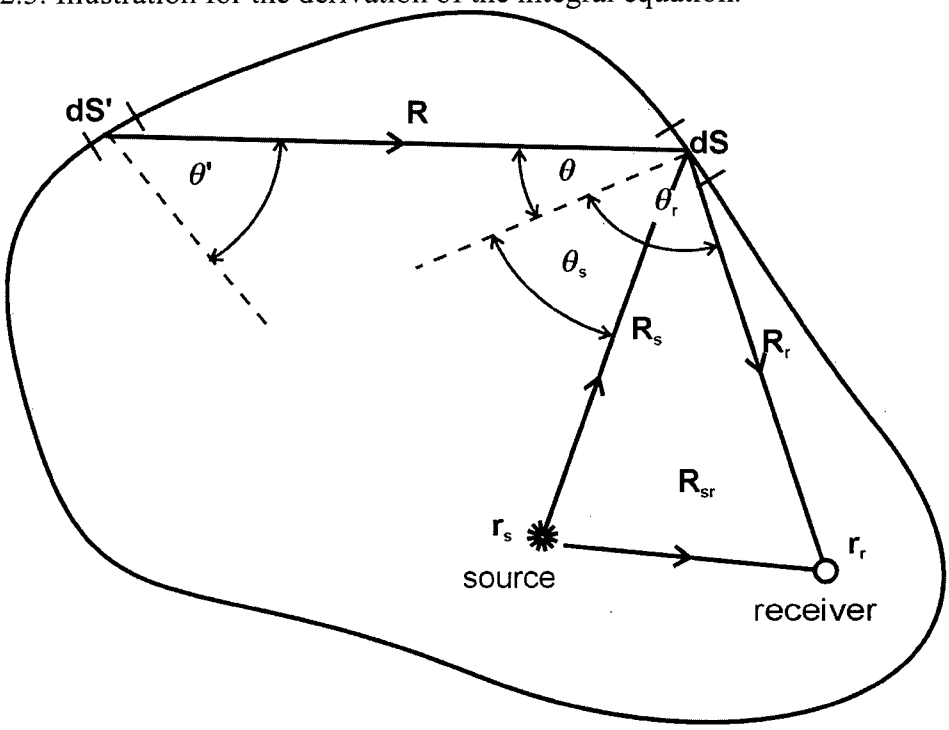

To derive the integral equation, consider two of the wall elements, dS and dS' (see Figure 2.3). By the assumption that the enclosure is empty and convex (see Section 2.1.3), we do not need to determine visibility between wall elements. We characterize the locations of dS and dS' by the vectors r and r'. Let R be the length of the line joining dS and dS', and let θ and θ' be the angles between the line and the normals of dS and dS', respectively. Note that R, θ and θ' are all functions of r and r'.

Let $B(r',t)$ be the radiation density of dS' at time t. The energy radiated from dS' that hits dS has intensity given by Eq. (2.4)

$$B(r',t)e^{(-mR)}\frac{\cos\theta'}{\pi R^2}dS'.$$

Sound takes R/c seconds to travel from dS' to dS (where c is the speed of sound in air), and since it is incident at an angle of θ to the normal of dS, the radiation density of dS due to $B(r',t)$ is, according to Eq. (2.5),

$$B_{dS'}(r,t+R/c)=B(r',t)\rho(r)e^{(-mR)}\frac{\cos\theta\cos\theta'}{\pi R^2}dS'$$

where $\rho(r)$ is the reflection coefficient of dS (recall the assumption of reflection coefficient independent of angle of incidence angle). We can equivalently write

$$B_{dS'}(r,t) = B(r',t-R/c)\rho(r)e^{(-mR)}\frac{\cos\theta\cos\theta'}{\pi R^2}dS'.$$

To get the total radiation density, $B(r,t)$, of dS at time t, we integrate this equation over all wall elements dS' and add the direct contribution $B_d(r,t)$ from the sound source to get:

$$B(r,t) = \frac{\rho(r)}{\pi}\int_S B(r',t-R/c)e^{-mR}\frac{\cos\theta\cos\theta'}{R^2}dS' + B_d(r,t)$$

$$= \frac{\rho(r)}{\pi}\int_S B(r',t-R(r,r')/c)e^{-mR(r,r')}\frac{\cos(\theta(r,r'))\cos(\theta'(r,r'))}{R(r,r')^2}dS' + B_d(r,t). \qquad (2.7)$$

The second formulation is included to emphasize that R, θ and θ' are functions of r and r'. It is important to realize that the assumption of phase independence underlies this step. Without this assumption, we could not simply integrate over radiation densities to find the total radiation density. Eq. (2.7) is what is commonly referred to as the 'integral equation', and is the basis for acoustical radiosity.

2.3.2 Simplifications

If the sound source ceases to radiate and sufficient time passes so that there is no longer any contribution of the source to the boundary, the direct contribution term of Eq. (2.7), $B_d(r,t)$ drops out to give a homogeneous integral equation. Other such simplifications can be made, with two listed below.

2.3.2.1 Impulsive sound sources

If the source is impulsive, and we let $t = 0$ be the time of generation of the impulse, then we can simplify the equation by neglecting air absorption until the end. We get

$$B(r,t) = \frac{\rho(r)e^{(-mtc)}}{\pi}\int_S B(r',t-R/c)\frac{\cos\theta\cos\theta'}{R^2}dS' + B_d(r,t). \qquad (2.8)$$

The term $\exp(-mtc)$ can simply be incorporated this way because all energy in the system was introduced at time $t = 0$ and has thus traveled tc meters through the air at time t.

The air absorption term could also be incorporated even after finding the total intensity at the receiver. To do so, the method outlined in the next section is used to find the intensity at the

receiver without air absorption, $I_0(r,t)$. Then the intensity with air absorption, $I_m(r,t)$ is given by

$$I_m(r,t) = e^{-mtc} I_0(r,t) . \tag{2.9}$$

Another simplification here is that $B_d(r,t)$ is zero except at a unique value of t for each r. This value of t is simply the distance between the source and the wall element, divided by the speed of sound.

2.3.2.2 Continuous sound sources

For a steady continuous (not changing with time) source, we can eliminate the time dependence to get a time-independent integral equation:

$$B(r) = \frac{\rho(r)}{\pi} \int_S B(r') e^{-mR} \frac{\cos\theta \cos\theta'}{R^2} dS' + B_d(r) . \tag{2.10}$$

In discrete form, this is simply a set of linear, inhomogeneous equations that can be solved by iteration or by standard methods. This is the form that is found in computer graphics, and which is thoroughly discussed in the computer graphics literature.

2.3.3 Direct radiation density

Suppose the sound source is omni-directional with power $W(t)$ at time t. If the distance between the source and wall element dS is R_s and the line between the source and dS makes angle θ_s with the normal to dS (see Figure 2.3), then the radiation density of dS due to the source is

$$B_d(r, t + R_s / c) = \frac{W(t)\cos\theta_s}{4\pi R_s^{\,2}} \rho(r) e^{(-mR_s)} . \tag{2.11}$$

The $\cos(\theta_s)$ term is needed for the same projection of area reasons as before; the $4\pi R_s^2$ term accounts for the spherical divergence of the sound, and the absorption of the wall and the air are accounted for. Once again, it should be noted that R_s and θ_s are functions of r and the position of the source.

2.3.4 Sound pressure at the receiver

Once $B(r,t)$ is known for all r and t - that is, once the radiation density of all elements on the boundary for $t \geq 0$ is known - we can find the intensity and, hence, the energy density and the sound pressure, at the receiver. For a given wall element dS, characterized by r, the resulting intensity at the receiver at time t is, by Eq. (2.4),

$$I_{dS}(r_r,t) = \frac{B(r,t-R_r/c)\cos\theta_r}{\pi R_r^{\,2}} e^{(-mR_r)} dS$$

where r_r is the position of the receiver, R_r is the distance between the receiver and dS, and θ_r is the angle between the line joining the receiver to dS and the normal to dS (R_r and θ are both functions of r). Assuming incoherent phase relationships, the total intensity at the receiver is obtained by integrating the above equation over all wall elements and adding the direct contribution $I_d(r,t)$ from the source. This gives

$$I(r_r,t) = \frac{1}{\pi}\int_S \frac{B(r,t-R_r/c)\cos\theta_r}{R_r^{\,2}} e^{(-mR_r)} dS + I_d(r_r,t) \tag{2.12}$$

with

$$I_d(r_r,t) = \frac{W(t-R_{sr}/c)}{4\pi R_{sr}^{\,2}} e^{(-mR_{sr})} \tag{2.13}$$

where R_{sr} is the distance between the source and the receiver.

Given $I(r_r,t)$, the energy density $E(r_r,t)$ and the square of the average sound pressure $p^2(r_r,t)$ are found by

$$E(r_r,t) = I(r_r,t)/c \qquad \text{and} \qquad p^2(r_r,t) = I(r_r,t)\rho_0 c \tag{2.14}$$

where ρ_0 is the static value of the medium density. For air under normal conditions, $\rho_0 c = 414\,\text{kg m}^{-2}\,\text{s}^{-1}$ [36].

2.3.5 Note on view independence

One of the unique features of radiosity is that once $B(r,t)$ is known, the intensity at any receiver position is found relatively easily. $B(r,t)$ is defined by the enclosure and the source and is independent of the receiver. This feature gives radiosity an advantage over more traditional room acoustical models such as ray tracing or the method of images, in which the entire process

must be repeated for different receiver positions. An example of a situation where this would be an advantage is in walk-through simulations, where the environment is constant, and only the receiver position changes.

2.4 Analytical solutions of the integral equation

The inhomogeneous, time dependent integral equation, Eq. (2.7), must, in most cases, be solved numerically. The method used to do so in this research is outlined in the next chapter. Before that, however, it is useful, both for understanding and validation of the algorithms, to look at several cases for which closed form, analytical solutions do exist. Two such cases are the sphere and the infinitely long and wide, flat room.

2.4.1 Sphere

There are several papers [10,11,28,35,36] that explore solutions to the integral equation in spherical enclosures. Some of the main results are given here for use in validations of the numerical approach and algorithm used in this thesis. The reader is referred to the papers for details and for other useful results.

For a spherical enclosure of radius a, uniform absorption coefficient α, with a continuous omni-directional point source of power W located at the center of the sphere, and neglecting air absorption, Carrol & Miles [11] found the radiation density of the boundary (Eq. (34) of their paper) to be

$$B = \frac{W(1-\alpha)}{4\pi a^2 \alpha}. \tag{2.15}$$

Here $B = B(r,t)$ is constant over the boundary of the sphere for all times (due to the continuous sound source). (This formula differs from that of Carrol & Miles in the inclusion of the $(1-\alpha)$ term, because their I is irradiation density while our B is radiation density).

From this, and recalling that the integral over the solid angle over the entire sphere is just 4π, it follows easily from Eq. (2.12) and (2.13) that

$$I(r_r) = \frac{W(1-\alpha)}{\pi a^2 \alpha} + \frac{W}{4\pi R_{sr}^{\ 2}} \tag{2.16}$$

where R_{sr} is the distance between the source and the receiver (see also Eq. (39) of Carrol & Miles), and r_r characterizes the position of the receiver.

By definition, then, the steady state sound pressure level is simply

$$SPL(R_{sr}) = 10\log\left(\frac{I(R_{sr})\rho_0 c}{p_0^{\ 2}}\right) \approx 10\log\left(\frac{I(R_{sr})414}{4\times10^{-10}}\right) dB. \tag{2.17}$$

It is important to notice that the reverberant intensity, the first term in Eq. (2.16), is constant throughout the sphere. In particular, the reverberant sound field is fully diffuse (see Appendix A for definition of a diffuse field).

For the same spherical enclosure, Carrol & Chien [10] and Joyce [28] found the following equation relating decay time T_0, diameter transit time $\tau = 2a/c$, and absorption coefficient α

$$1 = 2(1-\alpha)\left(\frac{T_0}{\tau}\right)\left\{\left(1-\frac{T_0}{\tau}\right)e^{\tau/T} + \frac{T_0}{\tau}\right\}. \tag{2.18}$$

Air absorption can be incorporated into the decay time expression by assuming exponential decay. If $E_m(t)$ and $E(t)$ denote the energy in the room at time t with and without accounting for air absorption, respectively, and T denotes the decay time including air absorption, then

$$E(t) = E(0)e^{-t/T_0} \quad \text{and} \quad E_m(t) = E(0)e^{-t/T}.$$

Adding the air absorption term to $E(t)$, we get

$$E_m(t) = E(t)e^{-mtc}$$

$$\Rightarrow E(0)e^{-t/T} = E(0)e^{-t/T_0}e^{-mct}$$

$$\Rightarrow \qquad \frac{1}{T} = \frac{1}{T_0} + mc \tag{2.19}$$

Having found the decay time, reverberation time can be found using Eq. (B.1).

2.4.2 Flat room

Kuttruff [32,36] solved the integral equation for the case of a flat room consisting of two unbounded parallel planes (floor and ceiling). Both surfaces were assumed to have the same, uniform reflection coefficient, ρ. If an omni-directional point source with power W is located half way between the planes, and if the height of the room is h, then the steady state solution of Eq. (2.12) is

$$I(r) = \frac{W}{4\pi}\left(\frac{1}{r^2} + \frac{4\rho}{h^2}\int_0^\infty \frac{e^{-z}J_0(rz/h)z}{1-\rho z K_1(z)}dz\right)$$

$$\approx \frac{W}{4\pi}\left\{\frac{1}{r^2} + \frac{4\rho}{h^2}\left[\left(1+\frac{r^2}{h^2}\right)^{-3/2} + \frac{b\rho}{1-\rho}\left(b^2+\frac{r^2}{h^2}\right)^{3/2}\right]\right\} \tag{2.20}$$

where r is the horizontal distance from the point source, J_0 is the Bessel function of order zero and K_1 is a first order modified Bessel function. Kuttruff goes on to approximate Eq. (2.20) by a much simpler formula. The reader is referred to the literature for more on this.

CHAPTER 3

Numerical solution

3.1 Discretization

Due to the mathematical difficulty in finding analytical solutions to the integral equation derived in the previous chapter, we will seek numerical solutions. These involve discretization of the enclosure and of time.

3.1.1 Enclosure discretization

Following Miles [45], we discretize the room interior into small patches, S_i. From Eq. (2.7) we obtain the average radiation density of the ith patch, given by

$$B_i(t) = \frac{1}{A_i}\int_{S_i}\rho(r)\int_S F(r,r')B(r',t-R/c)e^{-mR}dS'dS + \frac{1}{A_i}\int_{S_i}B_d(r,t)dS$$

where A_i is the area of patch i and

$$F(r,r') = \frac{\cos\theta\cos\theta'}{\pi R^2}.$$

Let N be the number of patches, and assume that the reflection coefficient is constant over each patch, with ρ_i the reflection coefficient of patch i. For r and r' representing some central point and on patches S_i and S_j, respectively, we replace $B(r',t-R/c)$ by $B_j(t-R_{ij}/c)$, where R_{ij} is the distance between r and r'. We also replace e^{-mR} by $e^{-mR_{ij}}$ to get

$$B_i(t) = \frac{\rho_i}{A_i}\int_{S_i}\sum_{j=1}^{N}\int_{S_j}F(r,r')B_j(t-R_{ij}/c)e^{-mR_{ij}}dS'dS + B_{di}$$

where

$$B_{di} = \frac{1}{A_i} \int_{S_i} B_d(r,t)dS \,. \tag{3.1}$$

We can interchange the order of summation and integration over S_i, and take the constant $B_j(t - R_{ij}/c)e^{-mR_{ij}}$ out of the integrals to get

$$\begin{aligned} B_i(t) &= \rho_i \sum_{j=1}^{N} B_j(t - R_{ij}/c)e^{-mR_{ij}} \left(\frac{1}{A_i} \int_{S_i}\int_{S_j} F(r,r')dS'dS \right) + B_{di}(t) \\ &= \rho_i \sum_{j=1}^{N} B_j(t - R_{ij}/c)e^{-mR_{ij}} F_{ij} + B_{di}(t) \end{aligned} \tag{3.2}$$

where

$$F_{ij} = \frac{1}{A_i} \int_{S_i}\int_{S_j} F(r,r')dS'dS = \frac{1}{A_i} \int_{S_i}\int_{S_j} \frac{\cos\theta\cos\theta'}{\pi R^2} dS'dS \,. \tag{3.3}$$

F_{ij} is known as the form factor between patch i and patch j. Physically, F_{ij} is the fraction of energy leaving patch i that is incident on patch j. Finding form factors is one of the more difficult aspects of radiosity, as will be discussed in the next section.

3.1.2 Direct contribution

Assume a point source with power output $W(t)$. Then from Eq. (2.11), the direct contribution is

$$B_{di}(t) = \frac{1}{A_i} \int_{S_i} B_d(r,t)dS = \frac{\rho_i}{A_i} \int_{S_i} \frac{W(t - R_s/c)\cos\theta_s}{4\pi R_s^{\,2}} e^{-mR_s} dS \tag{3.4}$$

where R_s is the distance between the wall element and the source, and θ_s is the angle between the normal to S_i and the line joining the source and the wall element. Replacing R_s with R_{si}, the distance between the source and r, we get

$$B_{di}(t) = \frac{W(t - R_{si}/c)\rho_i}{4\pi A_i} e^{-mR_{si}} \int_{S_i} d\Omega \tag{3.5}$$

where

$$\int_{S_i} d\Omega = \int_{S_i} \frac{\cos\theta_s}{R_s^{\,2}} dS \tag{3.6}$$

is the integral over the solid angle subtended by S_i and the source. Solid angles and the evaluation of the integral over them are discussed in Section 3.3.

3.1.3 Sound pressure at the receiver

If we discretize Eq. (2.12) in the same way as we did Eq. (2.7), we get

$$I(r_r,t) = \frac{1}{\pi}\sum_{i=1}^{N}\int_{S_i}\frac{B_i(t-R_{rj}/c)\cos\theta_r}{R_r^{\,2}}e^{-mR_{ri}}dS + I_d(r_r,t)$$

$$= \frac{1}{\pi}\sum_{i=1}^{N}B_i(t-R_{ri}/c)e^{-mR_{ri}}\int_{S_i}d\Omega + I_d(r_r,t) \tag{3.7}$$

where $I_d(r_r,t)$ is as in Eq. (2.13), R_{rj} is the distance between the receive and r, and

$$\int_{S_i}d\Omega = \int_{S_i}\frac{\cos\theta_r}{R_r^{\,2}}dS\,.$$

Again, this integral is dealt with in Section 3.3. Once $I(r_r,t)$ is known, Eq. (2.14) gives

$$p^2(r_r,t) = I(r_r,t)\rho_0 c\,.$$

3.1.4 Time discretization

The final step to be made in the numerical solution of the integral equation is to discretize time. This idea of discretizing time has been previously applied to acoustical radiosity by several authors (Shi and Zhang [56], Miles [10]), although our approach differs slightly in several respects.

To discretize time, we split time into equal time steps,

$$t_0 = 0,\ t_1 = \Delta t,\ t_2 = 2\Delta t,\ldots,\ t_n = n\Delta t = t_{\max} \tag{3.8}$$

where $n = t_{\max}/\Delta t$ is the number of time steps and is dependent on the length of the time interval, Δt, and on the maximum time for which the predictions are to be carried out, $t_{\max}$. The choice of Δt and $t_{\max}$ are affected by various considerations, such as room dimensions, frequency of the sound source, absorption coefficients, desired accuracy and speed of predictions, and so forth. This will be investigated in the next chapter. For notational purposes, we note the following property:

$$t_a + t_b = a\Delta t + b\Delta t = (a+b)\Delta t = t_{a+b}\,. \tag{3.9}$$

We may now follow energy through the room from one time step to the next. The sound is generated at $t_0 = 0$ and is propagated thought the room according to Eq. (3.2). Now, however, any energy that arrives at a patch between time steps is pushed forward and added to the later time step. In this way, the radiation densities of the patches, B_i become discrete functions, with their domain being the set of all time steps. In a similar way, sound pressure at the receiver becomes a discrete function.

Time and enclosure discretization are incorporated into the radiosity algorithm outlined in Section 3.4. First, however, if is necessary to find the form factors and solid angles, as given by Eq. (3.3) and (3.6), respectively. These are dealt with in the next two sections.

3.2 Form factors

This section deals with the evaluation of form factors as given by Eq. (3.3) (see Figure 3.1):

$$F_{ij} = \frac{1}{A_i} \int_{S_i} \int_{S_j} \frac{\cos\theta \cos\theta'}{\pi R^2} dS' dS \,. \tag{3.10}$$

The evaluation of form factors can be an extremely difficult problem. For most pairs of surfaces S_i and S_j there is no analytical solution to the form factor equation.

Figure 3.1. Form factor geometry.

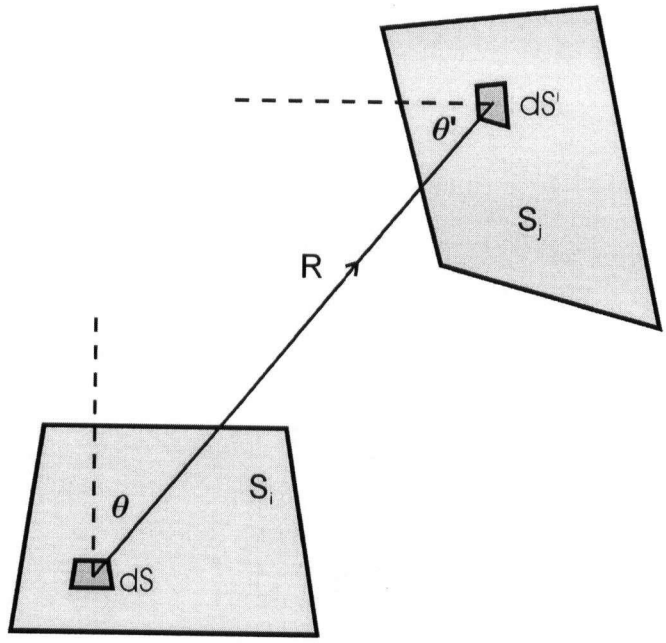

3.2.1 Literature on form factors

The evaluation of form factors has been well researched in other fields where radiosity is used - in particular, in illumination engineering, thermal radiation heat transfer, and, most notably, in computer graphics. Form factors in acoustics are the same as form factors in these other fields, hence the many methods developed in these fields are applicable to acoustical radiosity. Howell [24] published a catalog of radiation configuration factors (form factors) for use in thermal radiation heat transfer, that gives some useful references, although most of the configurations that are dealt with are not likely to help in room acoustics (notably, that between a differential element and a cow!). Any text on radiosity in computer graphics [2,12,15,60] will deal extensively with an overwhelming number of techniques for form factor evaluation and give references to a large body of literature on the topic.

Researchers in acoustical radiosity have applied various approaches in the evaluation of form factors. For rectangular, perpendicular and parallel patches, Miles [45] reduced the equation integrals to ones that may be calculated numerically by standard methods. Lewers [41] applied a discrete approximation.

More recently, Tsingos [63] estimated form factors by point-to-polygon form factors (or 'configuration factors' – see Section 3.2.4.2), which were estimated over a sampling of the receiver patch. The sampling method is very popular in the computer graphics community, and can be extended to find area-to-area form factors using a technique known as Monte Carlo Integration [12]. This method can be highly effective, particularly in the case of occlusions, and has been extensively researched in computer graphics. In this research, however, other methods were employed, and they are outlined below.

3.2.2 Form Factor Algebra

A few properties of form factors of interest for reducing computation times are explored here. Many other properties can be found in the thermal engineering literature, in which the topic is called 'form factor algebra'. Perhaps the most important property is that of reciprocity. Notice that F_{ji} can be found by simply reversing the patch subscripts, i and j, of F_{ij}. This gives the 'reciprocity relation':

$$A_i F_{ij} = A_j F_{ji}. \tag{3.11}$$

Furthermore, a planar patch cannot 'see' itself, thus

$$F_{ii} = 0 . \tag{3.12}$$

Moreover, for a closed environment with N patches, no energy can escape the environment so all energy leaving one patch must be received by the patches in the environment (conservation of energy). This gives the 'summation relation':

$$\sum_{j=1}^{N} F_{ij} = 1 . \tag{3.13}$$

3.2.3 Analytical form factors for rectangular rooms

In the initial stages of this research, when only rectangular patches in rectangular rooms were being considered, form factors were found using the analytical formulas from Hahne et al. [19](see also references [9] and [25]). These formulas allow for very simple and fast computation of form factors for rectangular patches. Because of their lengths, the formulas are not reproduced here.

3.2.4 *HeliosFF*

It was of interest to generalize the algorithms to non-rectangular rooms discretized by non-rectangular patches. To do this, the original code used in this research was modified to incorporate the form factor output from the software *HeliosFF* [20]. *HeliosFF* is a modified version of *Helios32*, a commercial graphics radiosity renderer. Ian Ashdown of *byHeart Consultants*, creator of *Helios32*, adapted his code to create *HeliosFF* for use in this research. Given a room and the reflection coefficients of its surfaces, *HeliosFF* meshes the room, and outputs form factors along with other pertinent data, such as patch vertices, centers, areas, normals, and reflection coefficients. The room is specified by an ordered listing of the vertices for each of its surfaces, and the user has basic control over the number of patches into which the room is meshed. *HeliosFF* uses a two-level hierarchical, cubic tetrahedral algorithm to compute form factors.

3.2.4.1 Two-level hierarchy

In radiosity, we can think of the patches in a room as having two functions - first as receivers, receiving energy from the source and from other patches, and then as sources, emitting towards other patches. The main idea behind a two-level hierarchy is that when the patches are

behaving as sources, it is sufficient to have a coarser meshing than when the patches are behaving as receivers (see later in this section) [12]. In a two-level hierarchy, the N patches are subdivided into M smaller elements ($N < M$), with each patch composed of the union of a subset of the elements. The patches act as sources and the elements act as receivers. The radiation density of a patch is then the weighted average of the radiation densities of the elements forming the patch.

To account for two-level hierarchy, we modify Eq. (3.2) as

$$B_{E_i}(t) = \rho_{E_i} \sum_{j=1}^{N} B_{P_j}(t - R_{E_iP_j}/c) e^{-mR_{E_iP_j}} F_{E_iP_j} + B_{dE_i}$$

with

$$B_{P_j}(t) = \frac{1}{A_{P_j}} \sum_{i \in \mathrm{E}} A_{E_i} B_{E_i}(t) \tag{3.14}$$

where E_i and P_j denote element i and patch j, respectively and E is the set of all i such that element i is contained in patch j - i.e. $\mathrm{E} = \left\{ i = 1, 2, \ldots, M \middle| E_i \subseteq P_j \right\}$.

The reason for a two-level hierarchy in computer graphics is intuitive [12]. When the patches are emitting energy to a distant receiver, the assumption of diffuse reflection effectively averages the energy arriving over a solid angle. Hence, the small details of the energy leaving the patch are lost, and a coarser meshing is sufficient. When an image is rendered, however, the details of its surface are crucial, so a finer meshing is needed. Since the number of patches required is less than the number of elements, a two-level hierarchy may considerably improve computational efficiency. More on two-level hierarchies (as well as extended hierarchical representations) may be found in books dealing with radiosity in computer graphics [2,12].

In acoustics, the benefit of a two-level hierarchy is questionable and remains to be explored. Here, we are trying to reproduce the impulse response at some point in the room, and are not so interested in the details of the sound field at the surfaces. In particular, since the sound field may not depend significantly on the exact detail of the surface, further subdivision of the patches into elements may not improve the model to the same extent that it does in graphics. In other words, if we have enough patches to correctly model the room, then perhaps more elements will not significantly improve the model (the effect of surface discretization is studied in Section 5.3.1.1). Since *HeliosFF* uses a two-level hierarchy, since the approach can only make

predictions more accurate, and since computing efficiency is not the main objective of this research, we will use two-level hierarchy.

3.2.4.2 Cubic tetrahedral algorithm

Because it is quite complicated, rather than trying to explain the cubic tetrahedral algorithm in detail here, we refer the reader to the computer graphics literature, where it is well documented [2,6,7,12]. It is a Gaussian quadrature method popular in computer science for its computational efficiency and accuracy. The method involves centering a tetrahedron over a differential element on patch i, meshing the tetrahedron into cells, and finding the form factors between the differential element and the cells. The form factors are stored in a look-up table. Patch j is then projected onto one or more of the cells of the tetrahedron. The sum of the form factors of the cells covered by the patch is approximately F_{ij}.

It is important to note that the cubic tetrahedral algorithm makes one underlying assumption that may affect predictions by the radiosity algorithm. This main assumption is that the form factor, F_{ij}, from patch i to j can be approximated by the form factor between one point on patch i and patch j. In equations:

$$F_{ij} \approx \int_{S_j} \frac{\cos\theta \cos\theta'}{\pi R^2} dS$$

at some sample point x_i on S_i (this is also called a 'configuration factor'[2]). (The generalization for element-to-patch form factors for a two-level hierarchy is straightforward and is left to the reader). What is really being assumed is that the inner integral is constant over patch i. Such an assumption may be reasonable if the distances between the patches are much greater than the size of patch i, but may be questionable for large or near patches. Obviously, what makes a patch 'large' or 'near' is important to investigate. In illumination engineering, a 'five-times' rule is used which states that a patch can be modeled as a point source only when the distance to the receiver is at least five times the maximum projected dimension of the patch [2]. Detailed studies by researchers in illumination engineering and in computer graphics have investigated the errors introduced by the approximation. For sound sources, Rathe [48] has shown that for a receiver located on the vertical line of symmetry of a rectangular source, the

source can be modeled as a point source if the distance to the receiver is at least the maximum dimension of the receiver divided by π.

For patches that are too large and too close, it is possible to reduce the error introduced by this assumption by subdividing the patch areas. Criteria governing when to stop subdividing (i.e. when further subdivision has insignificant effect on the rendered image) are available in the literature on computer graphics. Such criteria will probably be different in acoustics than in graphics - likely, they will be less stringent.

Several tests were carried out to compare the form factors given by *HeliosFF* to analytical form factors for rectangular rooms and rectangular patches [19]. For all cases considered, the maximum difference between the analytical form factors and those predicted by *HeliosFF* was 15%. For example, for an 8 by 4 by 2 room with 160 patches, the maximum difference between corresponding form factors was 14%; Helios gave a form factor of 0.073 when, analytically, it should have been 0.064. In general, finer subdivisions resulted in less error in the form factors predicted by *HeliosFF*. Further tests to establish the applicability of form factors found by *HeliosFF* are discussed in Section 5.3.4. Because a full investigation of form factors and their effect was beyond the scope of this research, we will satisfy ourselves with the subdivisions and calculations carried out by *HeliosFF*.

3.3 Integrals over solid angles

In Section 3.1 we were twice faced with the problem of finding the integral over the solid angles subtended by a point r and a surface S_i. In our case, the point was either the source or the receiver, and the planar surface was one of the patches. We need to find

$$\int_{S_i} d\Omega = \int_{S_i} \frac{\cos\theta}{R^2} dS$$

where θ is the angle between the surface normal and the line joining r and the surface element, and R is the distance between r and the surface element. In this section, we discuss possible approaches to evaluating the integral.

3.3.1 Possible approaches

Miles [45] gives a simple, closed form expression for a rectangular surface. In the present work, however, we wish to be able to work with non-rectangular patches, hence we need to find

a more general approach to finding the integrals. We will, however, assume planar, convex surfaces with straight edges (convex polygons).

One obvious approach is to approximate the integral by the value of $A_i \frac{\cos\theta_0}{R_0^2}$ where A_i is the area of S_i and θ_0 and R_0 are defined for some central point on the surface. Unfortunately, this is an unacceptable approximation, particularly for points that are close to the surface. Another approach that has been suggested [3] is to convert the integral to a contour integral using Stoke's theorem, but this is quite complicated.

3.3.2 Spherical triangle method

The developed and approach taken here, which we call the 'spherical triangle method' was not found elsewhere in the literature. It was developed to quickly and accurately find integrals over solid angles subtended by polygonal planar patches. The idea is to recognize that the integral is simply the area of the unit-spherical polygon (see Appendix A) subtended by the planar polygon and r (the unit sphere is centered at r) (see Figure 3.2(a)). To understand this, we consider an infinitesimally small differential element of S with area dS, at a distance R from r. We find the area it subtends on the unit sphere, $d\omega$. Consider the conical solid **S** with vertex at r and the differential element as base (see Figure 3.2 (b)). The area of the cross section of **S** at distance R from r is the area that the differential element projects in the direction θ - i.e. $\cos\theta dS$ (refer to Figure 2.1). Keeping the ratio of distance from r to cross-sectional area constant, the area of the cross section of **S** at unit distance from r must be $\cos\theta dS / R^2$ (since the

Figure 3.2. Illustrations for the spherical triangle method.

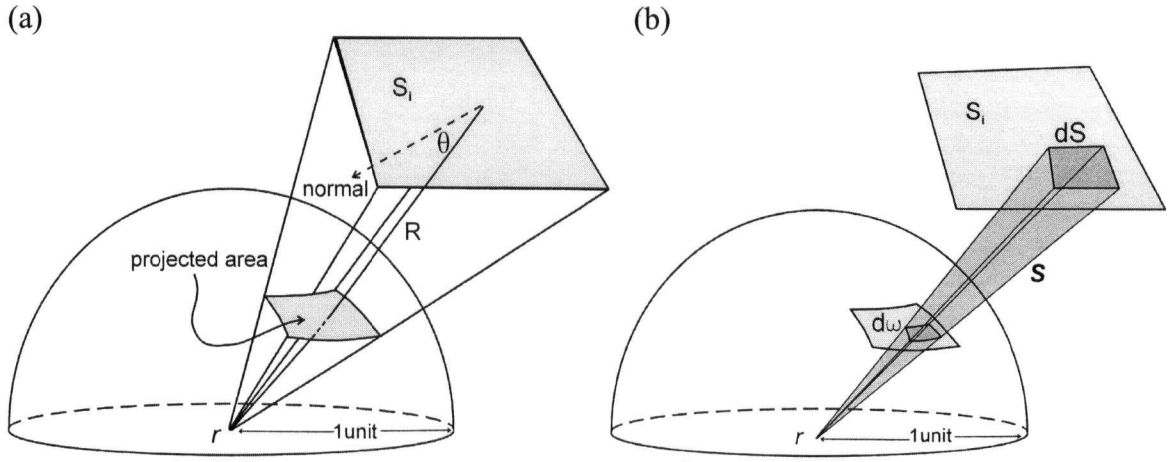

cross sectional area is proportional to the square of the distance from the vertex). Since dS is a differential area, $d\omega$ is precisely this cross sectional area at unit distance from r - i.e.

$$d\omega = \frac{\cos\theta}{R^2} dS .$$

Then $\int_{S_i} d\Omega$ is just the integral over S_i of infinitesimally small areas on the unit-sphere, so is itself the area of the unit-spherical polygon subtended by S_i and r, as required.

It follows that, to find $\int_{S_i} d\Omega$, we need only find the surface area of a spherical polygon. To do this, we apply the generalization of Girard's theorem as outlined in Appendix C. It follows from this theorem that, to find the surface area of a spherical polygon, we need only find the sum of all angles between planes formed by adjacent edges of the polygon and the center (source/receiver) point. Call this sum α. Then, by Eq. (C.3) (with $a = 1$),

$$\int_{S_i} d\Omega = \alpha + (2 - N)\pi \tag{3.15}$$

where N is the number of edges of the polygon. α can be easily found given the vertices of the polygon and the central point by taking cross products and using the cosine law as follows. Let $v_1, v_2, \ldots, v_N$ be the vertices of the polygon listed in clockwise (or counter-clockwise) order around the polygon and let p be the central point. Define $v_{N+1} = v_1$. Then, for $i = 1, 2, \ldots, N$, the normal to the plane P_i passing through v_i, v_{i+1}, and p is

$$n_i = (v_{i+1} - p) \times (v_i - p) .$$

Let α_i be the angle between P_i and P_{i+1} where $P_{N+1} = P_1$. Then, by the cosine law,

$$\cos\alpha_i = \frac{-n_{i+1} \cdot n_i}{\|n_{i+1}\| \|n_i\|}$$

where we take $-n_{i+1}$ to get the interior angle. Then

$$\alpha = \sum_{i=1}^{N} \alpha_i .$$

3.4 Algorithm

In this section, we outline the basic algorithm used in the implementation of the numerical solution, as discussed in the previous three sections. First, a basic outline is given for finding the numerical solution without further approximation, then an averaging technique is introduced for use in finding the later part of the decay.

3.4.1 Basic algorithm

First, we define

$$T_{E_iP_j} = \left\lceil \frac{R_{E_iP_j}}{c\Delta t} \right\rceil \tag{3.16}$$

as the number of time steps (rounded up to the nearest integer) between element E_i and patch P_j, where Δt is the time interval between time steps, as in Section 3.1.4 . The time, rounded to the nearest time step, taken for sound to travel from element i to patch j is simply $t_{T_{E_iP_j}} = T_{E_iP_j}\Delta t$. We similarly define the time steps for source-to-element, receiver-to-element, and source-to-receiver, T_{sE_i}, T_{rE_i}, and T_{sr}, respectively. To reduce the number of operations, we also define

$$K_{E_iP_j} = \rho_{E_i} F_{E_iP_j} . \tag{3.17}$$

Now, consider an omni-directional, impulsive sound source of power W that emits energy at time t_0 (time varying and steady state sound source responses can be found from impulsive source responses – see Appendix A). We will use the simplification suggested in Section 2.3.2.1 for impulsive sources to deal with air attenuation. In particular, we will neglect air attenuation until the end of our calculations, and add it according to Eq. (2.9). By Eq. (3.5), the direct contribution to element E_i is given by:

$$B_{dE_i}(t_{T_{rE_i}}) = \frac{\rho_{E_i} W}{A_{E_i} 4\pi} \int_{E_i} d\overline{\Omega} \tag{3.18}$$

where A_{Ei} is the area of element i and the integral is as in Eq. (3.6) and can be found by methods discussed in the previous section.

If n is the number of time steps, M is the number of elements, and N is the number of patches, then the time-discretized radiosity algorithm is as follows:

for $q = 1$ to $q = n$,

for $i = 1$ to $i = M$, where

$B_{E_i}(t_q) = B_{E_i}(t_q) + B_{dE_i}(t_q)$ % adding direct contribution

end

for $j = 1$ to $j = N$

$$B_{P_j}(t_q) = \frac{1}{A_{P_j}} \sum_{i \in \mathrm{E}} A_{E_i} B_{E_i}(t_q) \quad \text{where } \mathrm{E} = \left\{ i \middle| E_i \subseteq P_j \right\}$$

% by Eq (3.14)

for $i = 1$ to $i = M$,

$$B_{E_i}(t_{q+T_{E_iP_j}}) = B_{P_j}(t_q) K_{E_iP_j} + B_{E_i}(t_{q+T_{E_iP_j}})$$

% by Eq (3.2)

end

end

end

3.4.2 Averaging

Because the above process is very costly in the case of many time steps (i.e. large n), it may be desirable to estimate the late radiation densities rather than calculate them explicitly. A method for doing this, slightly modified from a suggestion by Rougeron et al. [52], is as follows. First, we note that the above algorithm traced element radiation density for more that the maximum time-step, t_n. Indeed, $q + T_{E_iP_j}$, the subscript in the last 'for' loop, may be greater than n (for $q = n$, for example). Let n' be the maximum such subscript. Then $B_{E_i}(t_q)$ for $n < q \le n'$ is the 'un-shot' instantaneous radiation density of element E_i at time t_q (where 'un-shot' means that it has not yet propagated to other elements). Define:

$$B_{avg}(t_q) = \frac{\sum_{i=1}^{M} A_{E_i} B_{E_i}(t_q)}{\sum_{i=1}^{M} A_{E_i}} \qquad \text{for } n < q \le n' \tag{3.19}$$

as the average un-shot radiation density at time t_q. B_{avg} for other time steps is zero,

$$\rho_{avg} = \frac{\sum_{i=1}^{M} A_{E_i} \rho_{E_i}}{\sum_{i=1}^{M} A_{E_i}} \tag{3.20}$$

as the average reflection coefficient, and

$$R_{avg} = \frac{4V}{\sum_{i=1}^{M} A_{E_i}} \tag{3.21}$$

where V is the volume of the enclosure. R_{avg} is the mean free path length of sound in the room. (See Kuttruff [36] for a derivation of $4V/S$ as the mean free path length in a room of arbitrary shape and with diffusely reflecting boundaries, where S is the surface area). Then define

$$q_{avg} = \left\lceil \frac{R_{avg}}{c\Delta t} \right\rceil \tag{3.22}$$

as the average number of time steps between elements. From this, we find the estimated radiation densities at time t_q, for $n+1 < q \le n' + q_{avg}$, as

$$\begin{aligned} B_{est}(t_q) &= B_{avg}(t_q - t_{q_{avg}}) + \rho_{avg} B_{avg}(t_q - 2t_{q_{avg}}) + \rho^2{}_{avg} B_{avg}(t_q - 3t_{q_{avg}}) + \ldots \\ &= \sum_{i=1} \rho^{i-1}{}_{avg} B_{avg}(t_{q - iq_{avg}}) \end{aligned} \tag{3.23}$$

where the summation is taken to the maximum i such that $q + q_{avg} > n$ and $B_{avg}(t_q) = 0$ for $q > n'$.

Now, let $n_{\max}$ be the maximum time step for which we wish to predict. Then $B_{est}(t_q)$ for $n' + q_{avg} < q \le n_{\max}$ remain to be found. They can be found by Eq. (3.23) above, but, since $B_{avg}(t_q) = 0$ for $q > n'$, it is simpler to find them by

$$B_{est}(t_{n'+i+jq_{avg}}) = \rho^j{}_{avg} B(t_{n'+i}) \tag{3.24}$$

for $i = 1, 2, \ldots, q_{avg}$ and $j \ge 1$ such that $n' + i + jq_{avg} \le n_{\max}$.

Once all B_{est} have been found, we add the estimated radiation densities to the exact ones to get the updated radiation densities,

$$B'_{E_i}(t_q) = B_{E_i}(t_q) + \rho_{E_i} B_{est}(t_q) \tag{3.25}$$

for $1 \le q \le n_{\max}$ (where $B_{E_i}(t_q)$ for $q > n'$ are defined as zero). The applicability of this method will be explored in the Chapter 5.

3.4.3 Sound pressure at the receiver

Having found all $B_{E_i}(t_q)$ (we have dropped the primes in the above expression for convenience), the sound intensity at the receiver (characterized by r) is found, using Eq. (3.7), by the algorithm:

for $q = 1$ to $q = n$,

for $i = 1$ to $i = M$,

$$I(r, t_{q+T_{rE_i}}) = I(r, t_{q+T_{rE_i}}) + \frac{1}{\pi} B_{E_i}(t_q) \int_{E_i} d\Omega$$

end

end

$$I(r, t_{T_{sr}}) = I(r, t_{T_{sr}}) + \frac{W}{4\pi R_{sr}^{\ 2}}$$ % direct contribution.

Finally, it remains to add the air absorption. This is done, very simply, according to Eq. (2.9). We can then find the squared pressure at the receiver from Eq. (2.14). This done, we may find the echogram and room acoustical parameters, as predicted by acoustical radiosity. Methods for doing this are discussed in the next chapter.

CHAPTER 4

Predictions from the solution

In this chapter we outline the methods used to make predictions of the room sound field from the solutions obtained by numerical evaluation of the integral equation (as outlined in the previous chapter). First, we find the impulse response, from which we can find the echogram, steady state sound pressure level (*SPL*), as well as the sound decay curve. From the decay curve, we can find reverberation time (*RT*) and early decay time (*EDT*). The impulse response can also be used to find clarity index (C_{80}), definition (D_{50}) center time (*TS*), and strength (*G*) directly from their definitions.

Based on the numerical methods and algorithms presented in the previous chapter and on the methods discussed here, code was written in *MATLAB* to implement acoustical radiosity. The code is outlined in Appendix D and is validated and investigated in the following chapter.

4.1 Impulse response

4.1.1 Definition

We have already introduced the impulse response in Chapter 1, and a formal definition can be found in Appendix A. In acoustical radiosity, as presented in this research, we are interested in finding an impulse response, $g(t)$, that can be convolved with the source power, $s'(t)$ (possibly varying with time), to give the pressure-squared response at the receiver, $s(t)$ (that is, the square of the pressure arriving at the receiver as a function of time). We refer to this as the 'pressure-squared' impulse response, and it has units Pa^2/W. Often (and ideally) in acoustics, the impulse response is the pressure response, but this is not feasible here because radiosity loses the required phase information by tracing sound intensity. Nevertheless, the

pressure-squared impulse response is sufficient for predicting echograms, decay curves, steady state sound pressure levels, and other common acoustical parameters, such as *RT*, *EDT*, C_{80}, D_{50}, *TS*, and *G* [35].

4.1.2 Prediction

Assume we have predicted $p^2(t)$ at the receiver by the radiosity algorithm outlined in Section 3.4 for an impulsive signal with power W at time $t = 0$ (and 0 for all other times). Then the predicted pressure-squared impulse response of the room for this signal is simply

$$g(t) = \sum_{i=1}^{n} \frac{p^2(t_i)}{W} \delta(t - t_i) \tag{4.1}$$

This predicted squared impulse response is discretized, with all reflections that come between two time steps, t_i and t_{i+1}, having been pushed forward and added to the reflection at t_{i+1}. This is a result of discretizing time in the numerical solution of the integral equation.

The W^{-1} factor is included in Eq. (4.1) to fit our definition of an impulse response. In a sense, our impulse response is 'normalized'. Were the W^{-1} factor not included, $g(t)$ would be the response to $W\delta(t)$ rather than to $\delta(t)$, as defined, and pressure-squared impulse response would be a function of the power of the source; signals would need to be weighed by W^{-1} before convolution with $g(t)$ to get the correct output. This way, convolving with our original signal, $s'(t) = \begin{cases} W & \text{for } t = 0 \\ 0 & \text{for } t \neq 0 \end{cases}$ gives back the output, $p^2(t)$ from the radiosity algorithm, as required.

4.1.3 Consistency check

It is important to confirm that sources of different powers will give the same impulse response when predicted this way (equivalently, that convolution with sources of different powers than the original gives the correct output). Of course, we require that the predictions are for the same room with the same meshing, and that the sources and receivers are in the same position. The confirmation is as follows.

Consider two impulsive sources, $s_1'(t)$ and $s_2'(t)$. Suppose that source i, $(i = 1,2)$ has power W_i, predicted pressure square response $p_i^2(t)$, and corresponding predicted impulse response (by Eq. 4.1)

$$g_i(t) = \sum_{j=1}^{n_i} \frac{p^2(t_{i_j})}{W_i} \delta(t - t_{i_j})$$

where the t_{i_j} are the times for which $p_i^2(t) \neq 0$, and n_i is the number of such times. Clearly, $s_i'(t) * g_i(t) = p_i^2(t)$ (where $*$ denotes convolution). We want to check that $s_2'(t) * g_1(t) = p_2^2(t)$. Carrying out the convolution gives,

$$s_2'(t) * g_1(t) = \frac{W_2}{W_1} p_1^2(t) = kp_1^2(t) \tag{4.2}$$

where $k = \frac{W_2}{W_1}$. So, we need only to show that $p_2^2(t) = kp_1^2(t)$.

In what follows, subscripts 1 and 2 correspond to sound sources 1 and 2, respectively. From Eq. (2.13) it is evident that $I_{d_2}(r_r, t) = kI_{d_1}(r_r, t)$. By the last theorem in Appendix C, it follows from Eq. (2.12) that

$$\begin{aligned} I_2(r_r, t) &= \frac{1}{\pi} \int_S \frac{B_2(r, t - R_r / c) \cos\theta_r}{R_r^2} e^{(-mR_r)} dS + I_{d_2}(r_r, t) \\ &= \frac{1}{\pi} \int_S \frac{kB_1(r, t - R_r / c) \cos\theta_r}{R_r^2} e^{(-mR_r)} dS + kI_{d_1}(r_r, t) \\ &= k\left[\frac{1}{\pi} \int_S \frac{B_1(r, t - R_r / c) \cos\theta_r}{R_r^2} e^{(-mR_r)} dS + I_{d_1}(r_r, t)\right] = kI_1(r_r, t) \end{aligned}$$

What we wanted to show - i.e. $p_2^2(t) = kp_1^2(t)$ - follows directly from Eq. (2.14), so that Eq. (4.1) is indeed consistent.

4.1.4 Integrating the impulse response

For many of the parameters and measures dealt with in the remainder of this chapter, it will often be necessary to integrate the impulse response over some limits. For $a \leq b$: if $b < 0$ or $t_n < a$ then

$$\int_a^b g(t) dt = 0$$

because our impulse response is zero in the interval. Otherwise, by Eq. (4.1),

$$\int_a^b g(t)dt = \int_a^b \sum_{i=0}^{n} \frac{p^2(t_i)}{W_1} \delta(t-t_i)dt$$

$$= \sum_{i=0}^{n} \frac{p^2(t_i)}{W_1} \int_a^b \delta(t-t_i)dt$$

$$= \frac{1}{W_1} \sum_{i=a'}^{b'} p^2(t_i) \tag{4.3}$$

where a' and b' are such that $t_{a'-1} < \max(0,a) \le t_{a'}$ and $t_{b'-1} < \min(b,t_n) \le t_{b'}$. Simply, $t_{a'}$ is the nearest time step above $t = a$, and similarly for b. The 'max' and 'min' are taken because the impulse response is zero for $t < 0$ and for $t > t_n$.

4.2 Signal response

From the pressure-squared impulse response, $g(t)$, the response to any signal, $s(t)$, is found by convolution of the source signal and the impulse response. For the original signal (the one used in the radiosity algorithm to give $p^2(t)$), we have $s(t) = p^2(t)$. From the discussion above, for an impulsive source with power W_2, $s(t) = \frac{W_2}{W_1} p^2(t)$ where W_1 is the power of the original source.

4.3 Echogram

The echogram for an impulsive source of power W_2 can easily be made from the signal response by definition. In particular, at time t_i we mark a vertical line of height $s(t_i) = \frac{W_2}{W_1} p^2(t_i)$ to get the echogram, where $p^2(t_i)$ is found using the radiosity algorithm outlined for an impulsive signal with power W_1.

4.4 Steady state sound pressure level

The steady state sound pressure level for a continuous source of power W_2, $s'(t) = W_2$ for all time t, is found as follows. The squared pressure response after sufficient time (the time needed for the room to reach a steady state, also the length of our impulse response) will be

constant, so that the root-mean squared pressure can be taken at one time, say t_0. Intuitively, the root-mean square pressure is just the sum of all the reflections (non-zero values) of the pressure-squared response of the impulsive signal with power W_2. The steady state sound pressure level is found as:

$$SPL = 10\log\left(\frac{s(t_0)}{p_0^{\,2}}\right) = 10\log\left(\frac{\int_{-\infty}^{\infty} s'(\tau)g(t_0-\tau)d\tau}{p_0^{\,2}}\right), \qquad \text{by convolution}$$

$$= 10\log\left(\frac{W_2\int_{-\infty}^{\infty} g(t)dt}{p_0^{\,2}}\right)$$

$$= 10\log\left(\frac{\frac{W_2}{W_1}\sum_{i=1}^{n} p^2(t_i)}{p_0^{\,2}}\right), \qquad \text{by Eq. (4.3)}$$

$$= 10\log\left(\frac{W_2}{W_1}\right) + 10\log\left(\frac{\sum_{i=1}^{n} p^2(t_i)}{p_0^{\,2}}\right) \tag{4.4}$$

where $p^2(t_i)$ is found using the radiosity algorithm outlined for an impulsive signal with power W_1.

4.5 Sound decay curve

To find the decay curve, suppose a steady source, $s'(t)$, of power W_2 is turned off at time $t = 0$ - i.e. $s'(t) = \begin{cases} W_2 & \text{for } t \le 0 \\ 0 & \text{for } t = 0 \end{cases}$. The decay curve for this source is found as

$$h(t) = 10\log\left(\frac{s(t)}{p_0^{\,2}}\right) - 10\log\left(\frac{s(0)}{p_0^{\,2}}\right) = 10\log\left(\frac{s(t)}{s(0)}\right)$$

$$= 10\log\left(\frac{\int_{-\infty}^{\infty} s'(\tau)g(t-\tau)d\tau}{\int_{-\infty}^{\infty} s'(\tau)g(0-\tau)d\tau}\right)$$

$$= 10\log\left(\frac{W_2\int_{-\infty}^{0} g(t-\tau)d\tau}{W_2\int_{-\infty}^{0} g(-\tau)d\tau}\right)$$

$$= 10\log\left(\frac{\int_{t}^{\infty} g(\tau)d\tau}{\int_{0}^{\infty} g(\tau)d\tau}\right).$$

So, by Eq. (4.3)

$$h(t) \approx 10\log\left(\frac{\sum_{i=a}^{n} p^2(t_i)}{\sum_{i=0}^{n} p^2(t_i)}\right) \tag{4.5}$$

where t_a is the time step with $t_{a-1} < t \le t_a$. $h(t)$ is the amount, in dB, at time t that the sound pressure level has changed from the steady state sound pressure level (at time $t = 0$). Note that this curve is in fact independent of the source power. In particular, the decay curve characterizes the room and its configuration, not the source.

4.6 Reverberation and early decay time

The reverberation time, *RT*, is found by estimating the slope of the decay curve. For this purpose, only part of the decay curve is considered. This is often taken to be the part where the decay curve has fallen to between 5 dB and 35 dB below the initial level. The slope is also often estimated from the decay between 5 dB and 25 dB below the initial level [26]. Once the slope m is found, the reverberation time is simply

$$RT = -60m^{-1}. \tag{4.6}$$

In this research, a line of best fit was fitted (using linear least-squares regression) to the decay curve between –5 dB and –35 dB.

EDT is also found by fitting a line of best fit to the decay curve. The slope is estimated from the decay between 0 and –10 dB.

4.7 Other Parameters

Define d to be the time taken for sound to travel from the source to the receiver. This is the time of arrival of the direct signal. Before $t = d$ the impulse response is zero (the direct signal is the first to arrive at the receiver).

4.7.1 Clarity

$$C_{80} = 10\log\left(\frac{\int_{d}^{d+80ms} g(t)dt}{\int_{d+80ms}^{\infty} g(t)dt}\right) = 10\log\left(\frac{\int_{0}^{d+80ms} g(t)dt}{\int_{d+80ms}^{\infty} g(t)dt}\right), \qquad \text{since } \int_{0}^{d} g(t)dt = 0$$

$$= 10\log\left(\frac{\sum_{i=0}^{a} p^2(t_i)}{\sum_{i=a}^{n} p^2(t_i)}\right) \tag{4.7}$$

where t_a is the time step with $t_{a-1} < d + 80ms \le t_a$.

4.7.2 Definition

$$D_{50} = \frac{\int_{d}^{d+50ms} g(t)dt}{\int_{0}^{\infty} g(t)dt} = \frac{\int_{0}^{d+50ms} g(t)dt}{\int_{0}^{\infty} g(t)dt} = 10\log\left(\frac{\sum_{i=0}^{a} p^2(t_i)}{\sum_{i=0}^{n} p^2(t_i)}\right) \tag{4.8}$$

where t_a is the time step with $t_{a-1} < d + 50ms \le t_a$.

4.7.3 Center time

$$TS = \frac{\int_0^\infty t g(t)dt}{\int_0^\infty g(t)dt} = \frac{\int_0^\infty t \sum_{i=0}^{n} \frac{p^2(t_i)}{W_1} \delta(t-t_i)dt}{\frac{1}{W_1}\sum_{i=0}^{n} p^2(t_i)}, \quad \text{by Eq. (4.1) and (4.3)}$$

$$= \frac{\sum_{i=0}^{n}\left[p^2(t_i)\int_0^\infty t\delta(t-t_i)dt\right]}{\sum_{i=0}^{n} p^2(t_i)} = \frac{\sum_{i=0}^{n} t_i p^2(t_i)}{\sum_{i=0}^{n} p^2(t_i)}. \tag{4.9}$$

4.7.4 Strength

$$G = 10\log\left(\frac{\int_0^\infty g(t)dt}{\int_0^\infty g_A(t)dt}\right) = 10\log\left(\frac{\frac{1}{W_1}\sum_{i=0}^{n} p^2(t_i)}{\left(\frac{e^{-10m}}{4\pi 10^2}\rho_0 c\right)}\right) \tag{4.10}$$

Note that the term in the denominator is just the free field squared sound pressure at 10 meters from an omni-directional point source of unit power. The simplification for this comes from understanding that there will only be one non-zero value in the impulse response in the free field, and that will come directly from the source (see Eq. (2.13)). The source has unit power to be consistent with our impulse response (in the numerator), which has power 'normalized' out (see the discussion after Eq. (4.1)). The strength calculated in this way is indeed independent of power.

4.7.5 Others

Measures of spaciousness, such as the lateral energy fraction (*LF*) and inter aural cross correlation (*IACC*) could also be easily predicted from the calculated wall radiation densities, $B_i(t)$, but are not considered in this research.

CHAPTER 5

Validation and experimentation

5.1 Validation of the numerical solution

As with any numerical solution, it was desirable to validate the numerical solution (both the methods and the algorithms) by comparing them to a known analytical solution. Such a comparison could also reveal possible problems or errors in the coding of the numerical solution. The algorithms developed are valid for (un-occluded) rooms of any shape with planar surfaces. We have analytical solutions for the sphere (Section 2.4.1), so one way to validate is in the case of a spherical enclosure with the curved walls approximated by a sufficiently fine mesh.

Ian Ashdown provided data for a meshed sphere, ready for input into *HeliosFF*. The meshing consisted of 288 patches and 408 elements. Predictions were made for three spheres of varying sizes and absorption coefficients. In all cases, the source was an omni-directional point source of power 0.005 W in the center of the sphere, and the sphere's surfaces had constant absorption coefficient, α . Absorption of air was neglected. The results are given in Table 5.1 . In the table, a is the radius of the sphere and r is the distance between source and receiver, both in meters. The subscripts 'theory' and 'rad' denote predictions by the analytical solution based on formulae from Section 2.4.1 and predictions by the radiosity algorithm, respectively. *RT* is reverberation time in seconds, and *SPL* is steady state sound pressure level in dB. The radiation

Table 5.1. Numerical and analytical predictions for three spheres.

Case	a	α	r	B_{theory}	$\overline{B_{rad}}$	B_{rad}	RT_{theory}	RT_{rad}	SPL_{theory}	SPL_{rad}
1	1	0.05	1/2	0.0076	0.0076	0.0074	1.047	1.044	105.18	105.24
2	2	0.20	$\sqrt{2}$	3.98e-4	4.03e-4	4.11e-4	0.483	0.488	92.68	92.66
3	3	0.50	$\sqrt{2}$	4.42e-5	4.48e-5	4.52e-5	0.242	0.240	85.90	85.90

densities listed (B in W/m^2) are for a steady-state source (with power 0.005 W). For radiosity, these are found by summing radiation densities for each patch (found from Eq. (3.2) for an impulsive source of power 0.005 W) over all time. This is just the radiation density signal response of the patch - the convolution of the radiation density impulse response of the patch convolved with the signal. $\overline{B_{rad}}$ is the average over all patches and B_{rad} is the value for the patch that differed most from B_{theory} (the worst case).

In each case, time was discretized at 24000 samples per second and the impulse response was found up to 'maximum time' seconds. Simulations were run on a Pentium III computer, with speed indicated in the Table 5.2. Run times and memory requirements are given in Table 5.2. Note that the long run times are for Module 2 (finding the radiation densities of the patches – refer to Appendix D for a discussion of the codes and modules). Run times for Module 3 (finding the impulse response at the receiver and making predictions) were always only a few seconds. Furthermore, *HeliosFF* found the form factors within a few seconds.

Clearly, the analytical and numerical solutions are very close, and we can have reasonable confidence in our numerical solution. It would have been interesting to investigate the effect of the resolution of the meshing of the sphere on the prediction. However, in the interest of time, and because the current meshing gave predictions consistent with analytical results, such an investigation was not performed.

5.2 Comparison Preliminaries

In this section we briefly describe the procedures to be used in investigating and evaluating the radiosity algorithm. These procedures will be used to compare radiosity to (1) variations for different predictions (different numbers of patches, differing time resolutions, and so on) by the radiosity algorithm; (2) other prediction methods (in particular, ray tracing); and (3) measurement.

Table 5.2. Time and memory requirement for predictions on three spheres.

Case	Computer speed (MHz)	max. time (s)	CPU time (s)	Memory requirement (MB)
1	1794	1.0	6.33 e4	93
2	2193	0.6	4.20 e2	63
3	2193	0.6	2.40 e2	30

5.2.1 Parameters, echograms, and discretized echograms

Listener perception of a sound field is affected by two main attributes of the field. The first is the arrival time and strength of the direct signal and the first-order reflections. Differences between sound fields with respect to these reflections can be seen in the comparison of echograms, which is perhaps the most fundamental way to compare prediction and measurement. Similar predictions and/or measurement will have similarly looking echograms. Such a comparison will reveal information about the sound fields, such as prominent reflections and other finer details about the distribution of energy in time.

The other perceptible attribute of the field is the temporal distribution of energy. Most room acoustical parameters are measures of this distribution (for example, C_{80} and D_{50} are defined by ratios of early and late energy), and have been established as being well correlated with listener perception [61]. For this reason, a comparison of these parameters is a good way to compare sound fields. Nevertheless, much information about the distribution of energy is lost to these parameters, which are not highly sensitive to subtle changes in the distribution.

To enable comparison of such changes, a technique called 'echogram discretization' was developed for use in this thesis. Echogram discretization is a way to compare total energy levels within small time steps. The idea behind echogram discretization is very simple: time is discretized and all energy arriving between points of discretization is summed to give the total energy for the corresponding time step. This is a similar idea to that used in discretizing time in the radiosity algorithm. To gain more information from the discretized echogram than is available from the original echogram, the resolution used in the echogram discretization must be coarser than the time resolution used in the radiosity algorithm (or in the case of measurements, the inverse of the sampling frequency). Note, however, that using a larger time interval in the radiosity algorithm will not give the same results as using a smaller time interval in radiosity and then using the larger interval in the discretization of the echogram.

5.2.2 Auralization

Auralization refers to techniques by which the predicted sound field is realized audibly. This can be done over headphones or by using loudspeakers. Because it is difficult to quantify what we hear, perhaps one of the best ways to compare predictions and measurements is to auralize their sound fields and compare the listener's perception of the different fields. Indeed, it

would be very interesting to listen to a room with perfectly diffusely reflecting boundaries, which does not exist in reality. Unfortunately, time limitations did not allow for the inclusion of auralization into this research.

5.2.3 Ray tracing with *RAYCUB*

It is of interest to compare radiosity to ray tracing, which is one of the most comprehensive and thoroughly investigated room acoustics prediction methods. The ray tracing model used for this comparison is *RAYCUB*, consolidated by Murray Hodgson. *RAYCUB* uses the ray tracing algorithm suggested by Ondet and Barbry [47], with modifications to predict echograms and acoustical parameters, and to account for diffuse reflections, as described by Kuttruff [30]. *RAYCUB* allows the user to input all of the room characteristics (room dimensions, source/receiver positions, absorption coefficients, air absorption exponents), the receiver size (a cube of finite volume), the number of rays to be traced, the number of ray trajectories, and the sampling rate. In addition, a diffuse reflection coefficient, d, is input for each of the surfaces. This coefficient gives the proportion of the incident energy that is diffusely reflected. The remaining proportion, $1-d$, of the energy is specularly reflected, so that $d = 1$ and $d = 0$ correspond to purely diffuse and specular reflection, respectively. To incorporate this, a random number in the interval (0,1) is chosen at each reflection. If the number is less than or equal to d, then the reflection is diffuse, otherwise it is specular. In the case of diffuse reflection, two additional random numbers determine the direction of the reflected ray. The first number is chosen in the interval $(-\pi, \pi)$ to define the azimuthal angle of the reflected ray. The polar angle of the reflected ray is defined by the arccosine of the square root of the second number, chosen in the interval (0,1). Details about this method can be found in the paper by Kuttruff [30].

5.2.4 Predicted impulse response length

It is important to have an understanding of how the length of the predicted impulse response may effect our predictions and, thus, what prediction length is required. In particular, since many of the parameters involve integrals of the impulse response from some time to infinity, we must be careful not to lose too much information and introduce too much inaccuracy by not predicting the impulse response to a sufficiently large time. We turn our attention to reverberation time.

For this discussion, we assume exponential decay of the energy in the room. Let T be the decay time at the receiver position. Then

$$E(t) = \frac{s(t)}{\rho_0 c^2} \tag{5.1}$$

by Eq. (2.14), where $E(t)$ is the energy density at the receiver position at time t and $s(t)$ is the pressure squared signal response. Also, $E(t) = E(0)e^{-t/T}$ by the assumption of exponential decay (see Appendix A). It follows that $s(t) = s(0)e^{-t/T}$, and that the decay curve is given by

$$h(t) = 10\log\left(\frac{s(t)}{s(0)}\right) = 10\log\left(\frac{s(0)e^{-t/T}}{s(0)}\right) = 10\log\left(e^{-t/T}\right). \tag{5.2}$$

Let $g(t)$ be the complete (pressure squared) impulse response extending to infinite time. Then the decay curve, as in Section 4.5, is given by

$$h(t) = 10\log\left(\frac{s(t)}{s(0)}\right) = 10\log\left(\frac{\int_t^\infty g(\tau)d\tau}{\int_0^\infty g(\tau)d\tau}\right).$$

If t_{final} is the maximum time to which the impulse response is predicted, the integral to infinity is approximated by the integral to t_{final}, and we get the approximate decay curve, $h_{approx}(t)$, defined for $0 \le t < t_{final}$

$$\begin{aligned}
h_{approx}(t) &= 10\log\left(\frac{\int_t^{t_{final}} g(\tau)d\tau}{\int_0^{t_{final}} g(\tau)d\tau}\right) \\
&= 10\log\left(\frac{\int_t^\infty g(\tau)d\tau - \int_{t_{final}}^\infty g(\tau)d\tau}{\int_0^\infty g(\tau)d\tau - \int_{t_{final}}^\infty g(\tau)d\tau}\right) \\
&= 10\log\left(\frac{s(t) - s(t_{final})}{s(0) - s(t_{final})}\right) \\
&= 10\log\left(\frac{s(0)e^{-t/T} - s(0)e^{-t_{final}/T}}{s(0) - s(0)e^{-t_{final}/T}}\right) = 10\log\left(\frac{e^{-t/T} - e^{-t_{final}/T}}{1 - e^{-t_{final}/T}}\right).
\end{aligned} \tag{5.3}$$

In our predictions, reverberation time is found from the slope of the line of best fit to the decay curve between -5 and -35 dB (see Section 4.6). The exact decay curve, $h(t)$, is a straight line (passing through the origin) with slope $m = -\frac{10}{T\ln(10)}$ (this can be easily confirmed by taking the derivative of $h(t)$). Differentiating $h_{approx}(t)$ with respect to time to find the slope of the approximate decay curve at time t we get

$$m_{approx}(t) = \frac{dh_{approx}(t)}{dt} = \left(\frac{-10}{\left(e^{-t/T} - e^{-t_{final}/T}\right)\ln(10)}\right)\left(-\frac{e^{-t/T}}{T}\right)$$

$$= \left(-\frac{10}{T\ln(10)}\right)\left(\frac{1}{1-e^{(t-t_{final})/T}}\right)$$

$$= \frac{m}{1-e^{(t-t_{final})/T}}. \tag{5.4}$$

Since $0 < e^{(t-t_{final})/T} < 1$ for $t < t_{final}$ (the domain of definition of $h_{approx}(t)$), $m_{approx}(t) < m < 0$, the approximated slope will always be greater than the actual slope. By Eq. (4.6), the approximated reverberation time is, consequently, less than the actual reverberation time. We have shown that predicting the impulse response to a finite time results in low approximated reverberation times. (Note that $\lim_{t_{final}\to\infty} h_{approx}(t) = h(t)$ and $\lim_{t_{final}\to\infty} m_{approx}(t) = m$ as they should.)

Suppose we want to find the approximate reverberation time within some small value ε of the actual reverberation time (we require $\varepsilon < RT$, otherwise we are allowing the predicted reverberation to be less than zero). Notice in Eq. (5.4) that as t increases to t_{final}, $m_{approx}(t)$ decreases. Thus, the slope of the line of best fit to (a finite sample of points along) $h_{approx}(t)$ between –5 and –35 dB is a better approximation to the actual slope, m, than the line between (t_5, -5) and (t_{35}, -35), where t'_5, and t'_{35} are such that $h_{approx}(t'_5) = -5$, and $h_{approx}(t'_{35}) = -35$ respectively. We approximate the slope as

$$m_{approx} = -\frac{30}{t'_{35} - t'_5} = -\frac{30}{\Delta t'} \tag{5.5}$$

where $\Delta t' = t'_{35} - t'_5$. From this we find the approximate reverberation time as

$$RT_{approx} = -60 m_{approx}^{-1} = 2\Delta t'. \tag{5.6}$$

Note that $RT_{approx} < RT$ (from the discussion after Eq. (5.4)). If we can ensure that

$$RT - RT_{approx} \leq \varepsilon, \tag{5.7}$$

then the reverberation time predicted from the line of best fit will also be within ε of the actual reverberation time (by the 'better approximation' argument above). We know

$$RT = -60m^{-1} = 6T\ln(10). \tag{5.8}$$

To find RT_{approx} we must find $\Delta t'$. By Eq. (5.3) and by definition of t_i' for $i = 5,35$,

$$-i = h_{approx}(t_i') = 10\log\left(\frac{e^{-t_i'/T} - e^{-t_{final}/T}}{1 - e^{-t_{final}/T}}\right)$$

$$\Rightarrow\ 10^{-i/10}\left(1 - e^{-t_{final}/T}\right) = e^{-t_5'/T} - e^{-t_{final}/T}$$

$$\Rightarrow\ t_i' = -T\ln\left[10^{-i/10}\left(1 - e^{-t_{final}/T}\right) + e^{-t_{final}/T}\right].$$

It follows that

$$\begin{aligned}\Delta t' &= t_{35}' - t_5' \\ &= T\ln\left[\frac{10^{-5/10}\left(1 - e^{-t_{final}/T}\right) + e^{-t_{final}/T}}{10^{-35/10}\left(1 - e^{-t_{final}/T}\right) + e^{-t_{final}/T}}\right] \\ &= T\ln\left[\frac{10^{-5/10}\left(e^{t_{final}/T} - 1\right) + 1}{10^{-35/10}\left(e^{t_{final}/T} - 1\right) + 1}\right].\end{aligned} \tag{5.9}$$

To find the minimum required value of t_{final} to satisfy Eq. (5.7), we combine Eq. (5.6) - (5.9), to get

$$6T\ln(10) - 2T\ln\left[\frac{10^{-5/10}\left(e^{t_{final}/T} - 1\right) + 1}{10^{-35/10}\left(e^{t_{final}/T} - 1\right) + 1}\right] \leq \varepsilon$$

$$\Rightarrow \qquad \frac{10^{-5/10}\left(e^{t_{final}/T} - 1\right) + 1}{10^{-35/10}\left(e^{t_{final}/T} - 1\right) + 1} \leq 10^{-3}e^{\frac{\varepsilon}{2T}}$$

$$\Rightarrow \qquad e^{t_{final}/T} \geq 1 + \frac{\left(10^{-3}e^{\frac{\varepsilon}{2T}}\right) - 1}{10^{-35/10} - 10^{-5/10}\left(10^{-3}e^{\frac{\varepsilon}{2T}}\right)}$$

$$\Rightarrow \qquad t_{final} \geq T \ln\left[1 + \frac{\left(10^{-3} e^{\frac{\varepsilon}{2T}}\right) - 1}{10^{-35/10} - 10^{-5/10}\left(10^{-3} e^{\frac{\varepsilon}{2T}}\right)}\right] = t_{final_{\min}}(\varepsilon, T) \tag{5.10}$$

Note that all times (including $t_{final_{\min}}(\varepsilon,T)$) are in seconds and that Eq. (5.10) applies only for $\varepsilon < RT = 6T\ln(10)$. For values of epsilon equal to the reverberation time, the second term in the brackets for natural log is zero, giving $t_{final} = 0$. Indeed for $\varepsilon \geq RT$, $RT_{approx} = 0$ satisfies Eq. (5.7) so that no prediction is needed. Figure 5.1 shows $t_{final_{\min}}$ versus reverberation time for various ε.

If the reverberation time is to be predicted from the decay curve between -5 and -25 dB, -35 in the denominator of Eq. (5.10) must be replace by -25. This will result in a smaller value of $t_{final_{\min}}(\varepsilon,T)$, so that the impulse response does not need to be predicted as far.

Figure 5.1. $t_{final_{\min}}$ versus reverberation time for various ε.

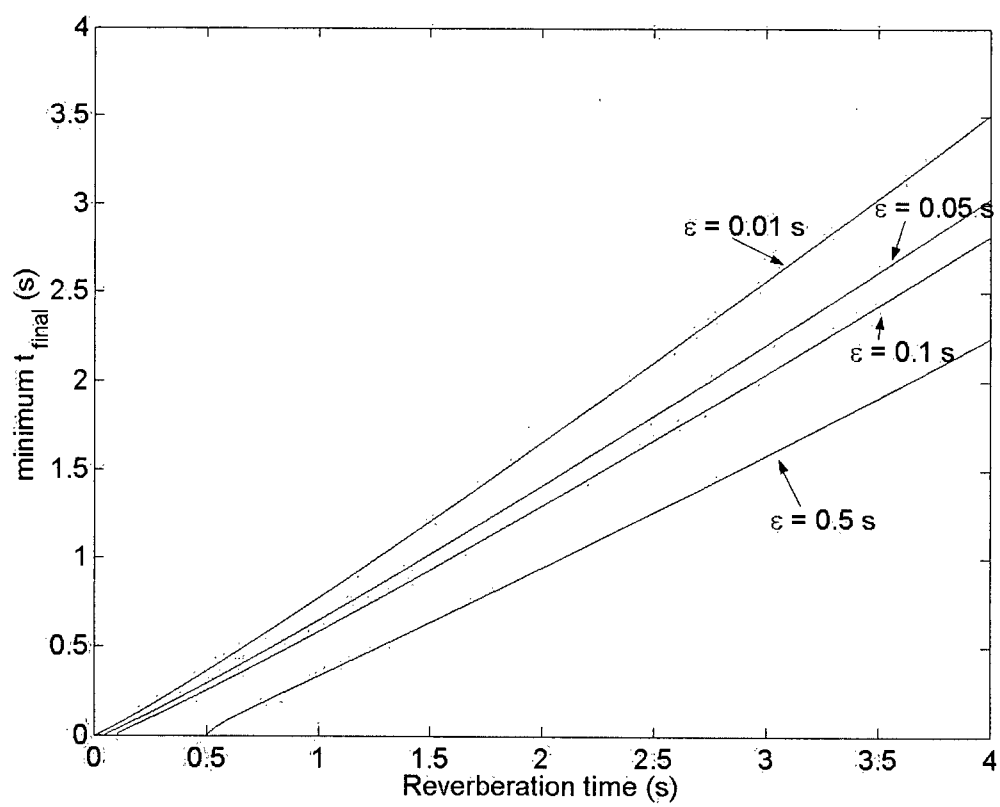

In summary, to guarantee that the reverberation time predicted from a truncated impulse response is within ε of the reverberation time obtained from the full impulse response, the truncation must occur at a time greater than $t_{final_{\min}}(\varepsilon, T)$, given in Eq. (5.10), where T is the actual decay time. The reverberation time obtained from a truncated impulse response will always be less than the reverberation time obtained from the full impulse response. This is based on an assumption of exponential decay, and may not be applicable to responses with non-exponential decay.

5.3 Predictions for a cubic room

To investigate several issues surrounding the convergence and computational efficiency of the numerical solution developed in the previous section, the radiosity algorithm was run numerous times for four cubic rooms. Each cube had walls 8 m long, and an average absorption coefficient of 1/6 (average absorption coefficients were chosen to be equal to allow for observations about the effect of absorption distribution). The absorption was distributed as indicated in Table 5.3.

Predictions were made varying: (1) the number of patches (only a singe-level hierarchy was applied); (2) the resolution of the time discretization; (3) the length of time for which exact and approximate predictions made are made; and (4) the form factor prediction method. The effect of the varying distribution of absorption (among the four cubes) was investigated using the results, and comparisons were made with predictions by ray tracing. For each prediction, the source was in the center of the cube and had power 0.005 W. The receiver was located two meters above the floor, two meters from the front wall, and two meters from a side wall (by symmetry of the configurations, it doesn't matter which). Air absorption was neglected throughout because it has no effect on convergence (from the way it is incorporated).

Table 5.3. Distribution of absorption in the cubical rooms. In all cases, $\bar{\alpha} = 1/6$.

Cube	Distribution of absorption
1	$\alpha = {}^1/_6$ over all walls
2	$\alpha = 1$ on the floor, 0 on the other walls
3	$\alpha = {}^1/_2$ on the floor and the ceiling, 0 on the other walls
4	$\alpha = {}^1/_2$ on the floor and the front wall, 0 on the other walls

Figure 5.2. Discretization of the cubical rooms.

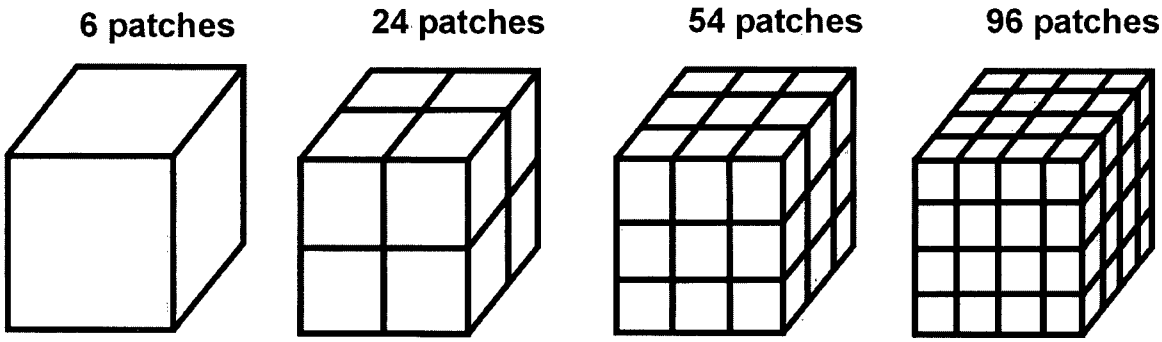

5.3.1 Initial predictions with varying patch sizes

The fundamental basis of the numerical solution of the integral equation was the discretization of the boundary. This results in discretization error, which we expect becomes smaller as the resolution of the meshing is increased. In particular, we expect that, as the resolution is increased, the numerical solution approaches the analytical solution. Because CPU requirements increase with the square of the number of patches (as we shall see later in this section), we wish to minimize the number of patches used in the discretization. The following investigation was conducted to gain better understanding about requirements for the resolution of the mesh used.

For each cube, the radiosity algorithm was run ten times for each cube with an increasing number of patches. The first prediction for each cube had each wall as a single patch, giving a total of six patches. For the second prediction, each wall was divided into four equally sized, rectangular patches, giving 24 patches in total. The third prediction had nine patches on each wall for a total of 54 patches, the fourth had 16 for 96 total, and so on (in general, the nth prediction had n^2 patches on each wall and $6n^2$ patches in total - see Figure 5.2).

The predictions were made with discretization period $\Delta t = 1/24000$ s. This was chosen based on initial, rough predictions that indicated that there is almost no variation in the parameters if the time is discretized more finely than $\Delta t = 1/18000$ s. Time discretization is discussed further in Section 5.3.2. Form factors were found using the analytical formulas given by Hahne et al. [19].

t_{exact} and t_{final} were set to 0.8 s and 1.0 s, respectively, where t_{exact} is the time step to which the exact radiosity prediction is made (corresponding to t_n of Section 3.1.4) and t_{final} is the last time step to which the prediction is made (corresponding to $t_{n_{\max}}$ of Section 3.4.2). They

were chosen according to Eq. (5.10) as follows. According to Eying, *RT* in the cubical rooms should be 1.1782 s, which corresponds to a decay time of 0.0853 s by Eq. (B.1). Although this decay time may not be perfectly accurate (due to the limitations of diffuse field theory [23] we can take it as an initial estimate for use in Eq. (5.10). To apply Eq. (5.10), we also must assume exponential decay. Miles [45] has shown that in general, after some time, the decay curves predicted using the integral equation, Eq. (2.7), are strictly exponential. Consequently, even though the first part of the sound decay may not be exponential, the assumption of exponential decay along the entire curve may not be unreasonable in this application. If we wish to predict reverberation time within 0.01 s of the full impulse response *RT* (which represents very high accuracy), then according to Eq. (5.9), we need

$$t_{final} \geq t_{final_{\min}}(0.001, 0.0853) = 0.9264 \text{ s}.$$

$t_{final} = 1.0$ was chose accordingly, and t_{exact} was chosen quite close to t_{final} because the effects of varying t_{exact} remained to be explored. t_{final} and t_{exact} are discussed further in Section 5.3.3.

5.3.1.1 Patch Size

Figure 5.3 shows the echograms for Cube 1 obtained from the 2nd, 3rd, 5th, and 10th predictions (with 24, 54, 150, and 600 patches, respectively). As the meshing is refined, it appears that the energy arriving at the receiver is spread out in time, with fewer distinct reflections. Indeed, the echogram for 600 patches has none of the outstanding, large peaks that the echogram for 24 patches has (apart from the direct signal). An explanation for this observation is that, with a finer meshing, the energy leaving a patch is divided into more parts to propagate to the other patches, so that large units of energy are quickly dissipated. This is what we would expect in a room with diffusely reflecting boundaries. The echograms have been plotted in Figures 5.4 and 5.5 with different domains and ranges than Figure 5.3 to show different details.

In a real room, with partially specularly reflecting boundaries, some distinct reflections would be expected, suggesting that fewer patches may give echograms looking more similar to measured echograms. However, this should not be interpreted as meaning that predictions with fewer patches give more realistic predictions. The arrival times and amplitudes of the distinct reflections in such predictions are unrealistic and do not correspond to times and amplitudes that would result from specular reflection.

Figure 5.3. Echograms for Cube 1 from predictions with 24, 96, 294, and 600 patches.

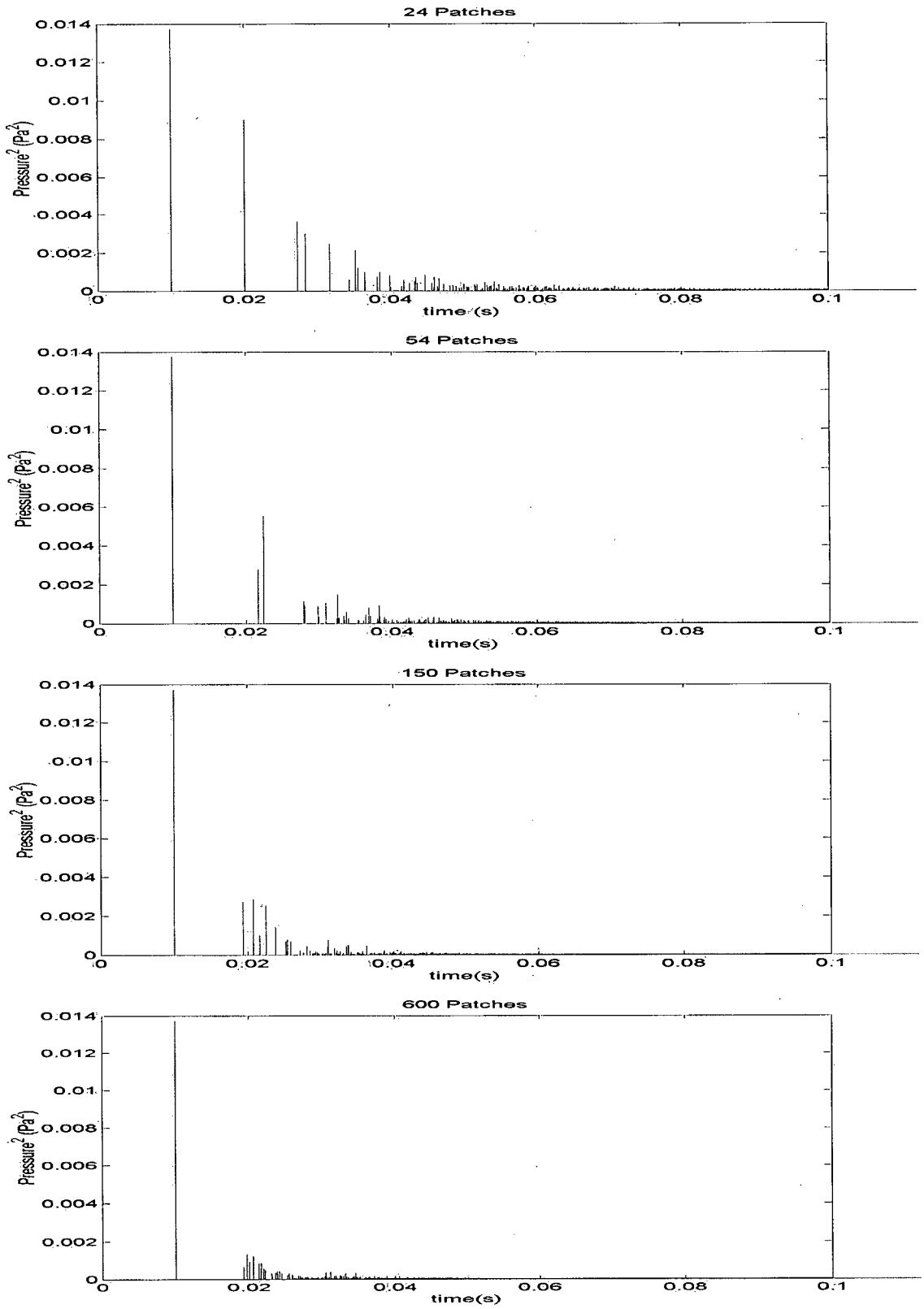

Figure 5.4. Range reduced from Figure 5.4 for more detail

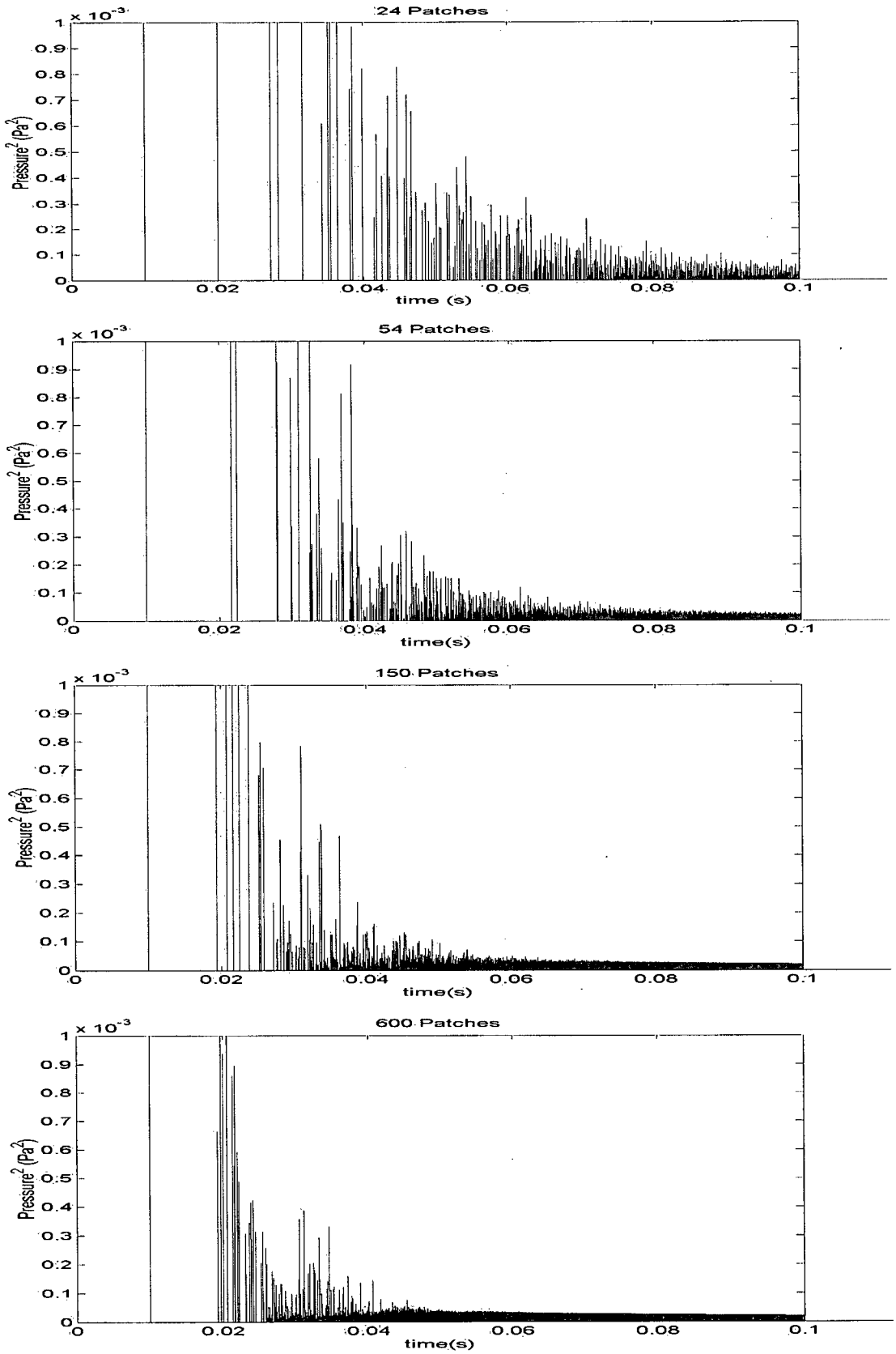

Figure 5.5. Range reduced and domain increased from Figure 5.5 for more detail.

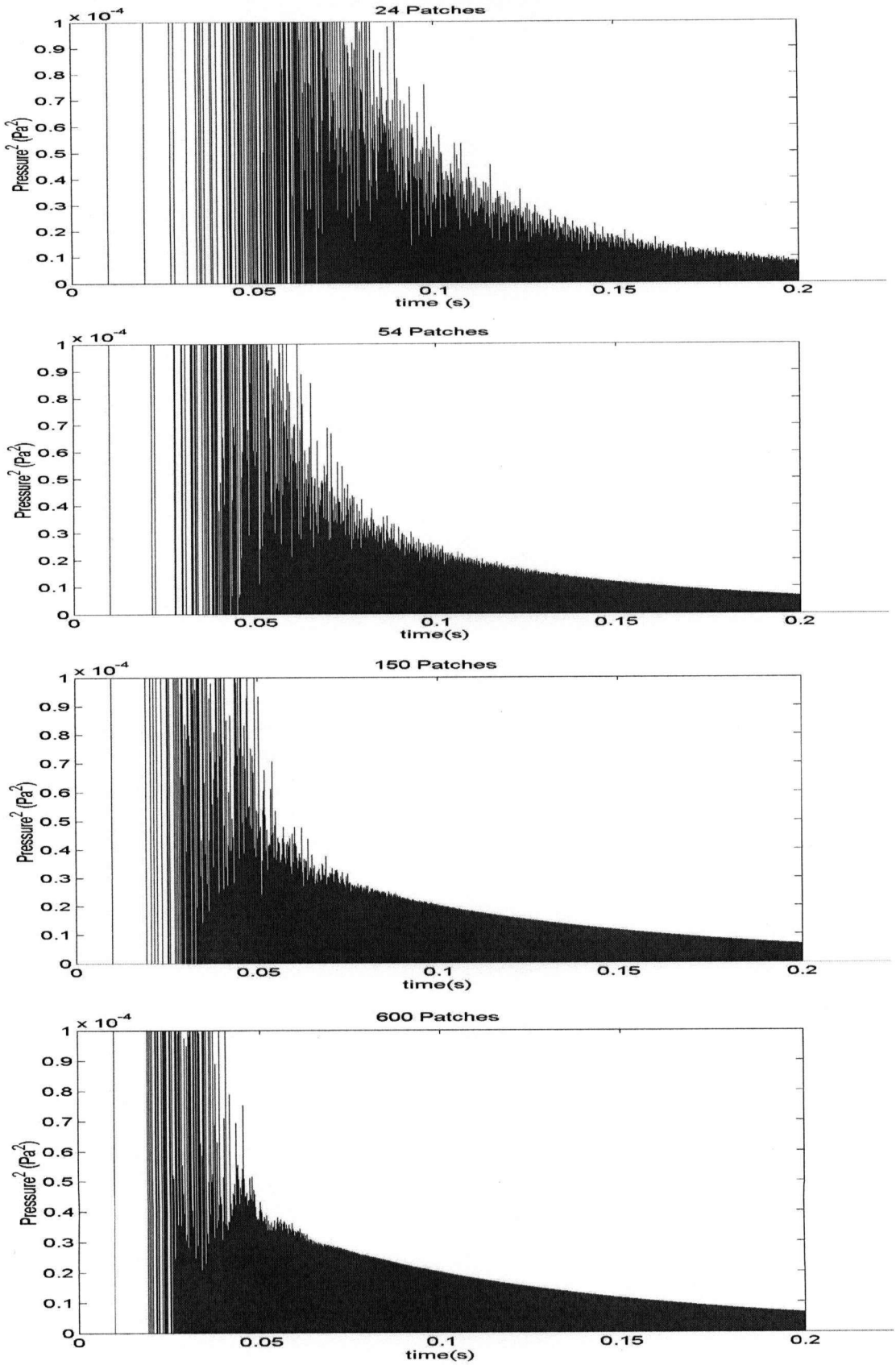

Figure 5.6 shows discretized echograms for Cube 1, with time intervals of 0.01 s and 0.05 s. For each time interval, the pressure-squared sums found for the 1st, 3rd, 5th, and 10th predictions (with 6, 54, 150, and 600 patches, respectively) are plotted next to one another. From the graphs, we see that more patches tend to result in more energy in the very early time steps, with levels becoming more uniform at about 0.15 s. The very early trend seems to reverse itself from about 0.2 s to 0.35 s, after which energy levels are once again very similar.

The most noticeable changes in the echograms and discretized echograms occur for predictions with less than 150 patches. For more than 150 patches, there is much less change, with predictions for 150 patches already very similar to predictions with 600 patches. This indicates that 150 patches are sufficient for accurate predictions in this case.

In Figure 5.7, the predicted values for the various parameters are plotted as a function of the number of patches. These plots are for Cube 1, and were very similar for all four cubes. Each of the parameters considered (*SPL*, *TS*, *EDT*, *RT*, C_{80}, and D_{50}) converged to a finite value as the number of patches was increased. The difference (in percent) between consecutive predictions decreased with increasing number of patches (here consecutive means between the nth and the $(n+1)^{st}$ prediction, with $6n^2$ and $6(n+1)^2$ patches, respectively). This suggests convergence by the ratio test [14]. Because the algorithm gave predictions very close to analytical solutions for the sphere, we can be quite confident that the numerical solution does indeed converge (with increasing number of patches) to the analytical solution to the integral equation.

C_{80} was quite clearly the slowest to converge of all the parameters. Even in the case where it was slowest to converge (Cube 1), however, the differences between fifth and sixth predictions of C_{80} were less than 1%. In fact, all of the other parameters (in all cubes) had differences less than 1% already between the third and fourth predictions. Indeed, a fine subdivision of the enclosure was not at all necessary in these trials, and 150 patches were sufficient for good predictions, as in the echograms.

Worth noting is that the difference between *SPL*s for the first and second prediction was already less than 1% (in all cubes). This suggests that radiosity can be used with a very coarse subdivision (one patch per wall in this case) to predict steady state sound pressure levels in rooms with diffusely reflecting boundaries, even with non-uniformly distributed absorption (at least for a cubical room).

Figure 5.6. Discretized echograms for Cube 1.

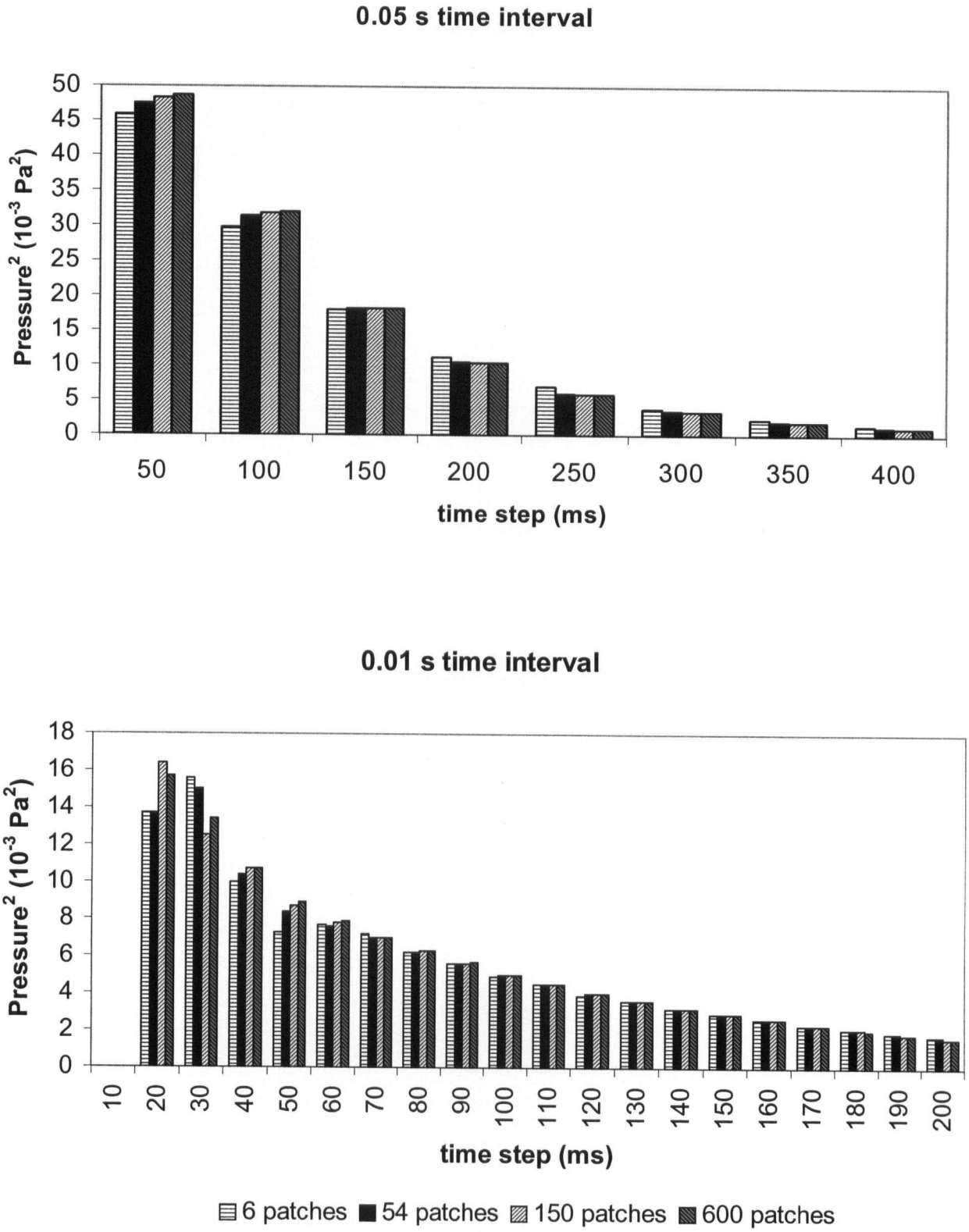

Figure 5.7. Parameter predictions versus number of patches for Cube 1.

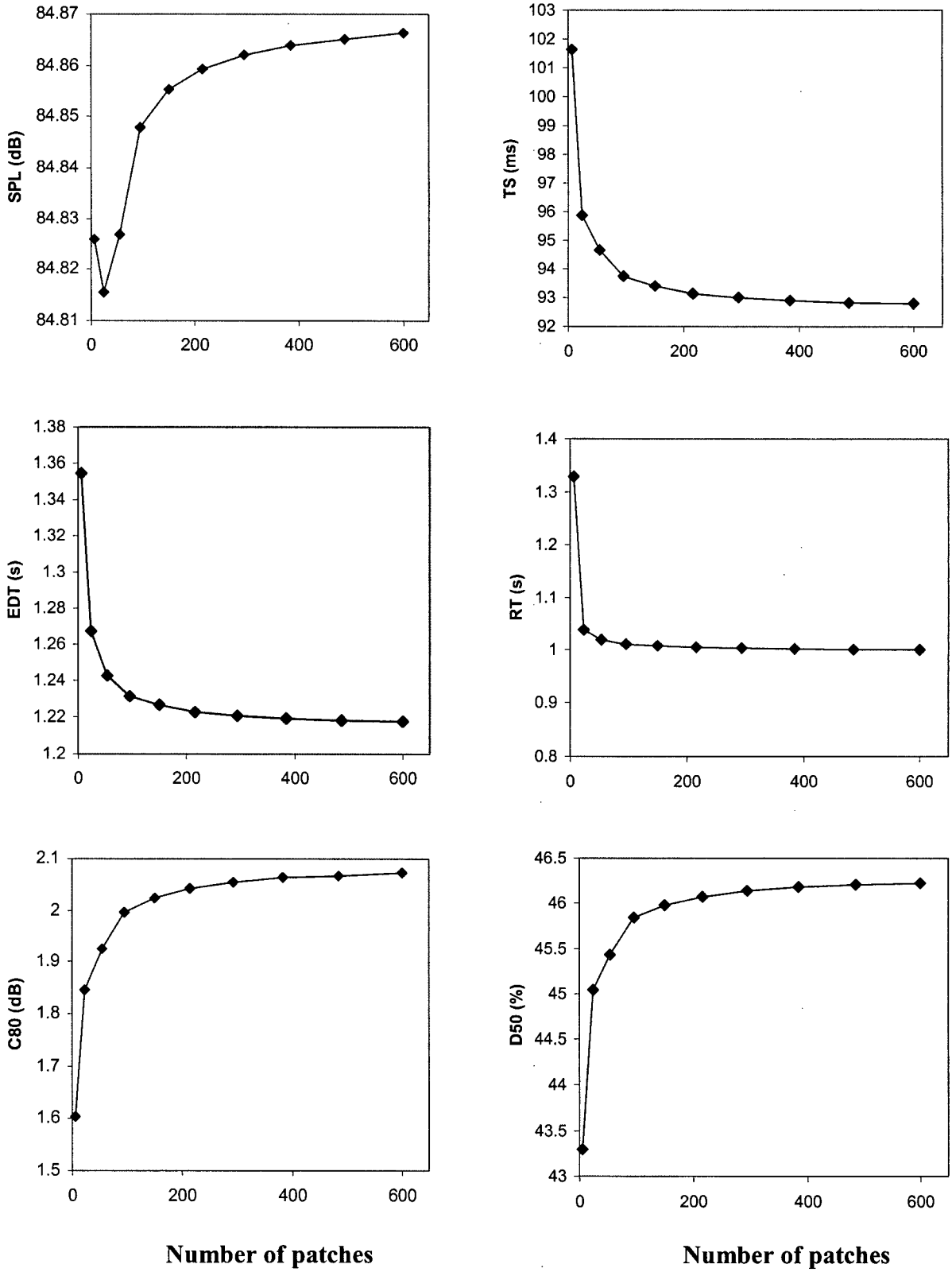

At this point, it is worth pointing out that the required patch size does not depend on the frequency of the sound that is being considered. This is due to the fact that phase is not accounted for in radiosity. Indeed, the integral equation is the same for any frequency (except for the values of absorption coefficients and air absorption constants), and consequently convergence of the numerical solution to the analytical solution is not frequency dependent (apart from changes in convergence with varying absorption). Convergence of the numerical solution to the analytical solution is not to be confused with convergence to the true solution (the solution that would be obtained in a real room). We certainly expect that the analytical solution to the integral equation (which is the converged numerical solution) will be closer to the true solution at higher frequencies, because phase effects are less significant at these frequencies. The phase independence of radiosity might also help to explain the adequacy of a coarse subdivision of the enclosure. Still, it is important to keep the relationship between the patch sizes and the wavelength of sound being considered in mind when working with acoustical radiosity. Particular attention must be paid in the case of high frequencies, where shorter wavelengths might require smaller patches. Refer to Section 3.2.4.2 for further discussion on patch sizes.

5.3.1.2 Absorption distribution

From the predictions made for the four different cubes, we can learn something about the effect of different distributions of absorption. As mentioned above, the average absorption coefficient in each cube was 1/6. Refer to Table 5.4 for the predicted parameters (from the run with 150 patches).

Reverberation time was longest in Cube 1, with uniform absorption, while the shortest reverberation time was in Cube 2, which had absorption on the floor. The 12% difference in *RT*

Table 5.4. Parameter predictions for the four cubical rooms.

Cube	**1**	**2**	**3**	**4**
***SPL* (dB)**	84.87	84.99	84.63	84.67
C_{80} (dB)	2.00	2.85	2.39	2.35
D_{50} (%)	45.87	49.88	47.83	47.58
***TS* (ms)**	94.67	84.50	89.70	90.20
***EDT* (s)**	1.24	1.08	1.17	1.17
***RT* (s)**	1.23	1.08	1.17	1.17

in these cubes indicates that absorption distribution has significant effect on *RT*. Following a line of reasoning set forward by Schroeder and Hackman [54], the reason Cube 2 had the lowest *RT* is that the absorbent surface 'sees' only reflective surfaces. In the other cubes, the absorbing surfaces 'see' surfaces that absorb some of the sound, so they receive lower sound energy than they would from reflecting surfaces. In Cube 1, no surfaces are fully reflecting, so that absorbing surfaces 'see' only other absorbing surfaces, resulting in a lower decay rate and higher *RT*. Since the absorbing surfaces in Cubes 3 and 4 'see' both reflecting and absorbing surfaces, the reverberation times are between those in Cube 1 and Cube 4.

Steady state sound pressure levels were very similar (within 0.4 dB) for all four patches. Predicted values of C_{80} are D_{50}, which are lower for Cube 1 and higher for Cube 4, are consistent with the predictions for *RT*. For higher *RT*s, we might expect lower C_{80} and D_{50} values because a slower decay rate means more late energy, giving lower early-to-late energy ratios (which are the basis of the definitions of clarity and definition). Similarly, higher and lower center times for Cubes 1 and 4, respectively, are consistent with the reverberation time results.

5.3.1.3 Computational efficiency

Experimental data suggests a computational time complexity of order n^2, where n is the number of patches and we are working in single level hierarchy (see Appendix A for the definition of order). This can be explained theoretically as follows. At each time step and for each element, $(n-1)$ elements must be considered in the calculations. Since there are n elements in total, this gives $n*(n-1)$ calculations for each time step, giving a time complexity of order n^2. For a two-level hierarchy with n elements and m patches, we expect a complexity of order $m*n$.

Also suggested by experimental data is a memory complexity of order n; memory requirement increases linearly with the number of patches. Once again, this makes sense theoretically because for each element, we need to compute radiation densities for all time steps, so that there are always $n*$(number of time steps) values to be stored.

Refer to Figure 5.8 for plots of elapsed time versus number of patches and for memory requirement versus number of patches. The run times and memory requirements are for predictions for Cube 2 (and are very similar to times and requirements for the other cubes). A 2193 MHz Pentium III desktop computer was used for these predictions.

Figure 5.8. CPU time and memory requirements versus number of patches for Cube 2.

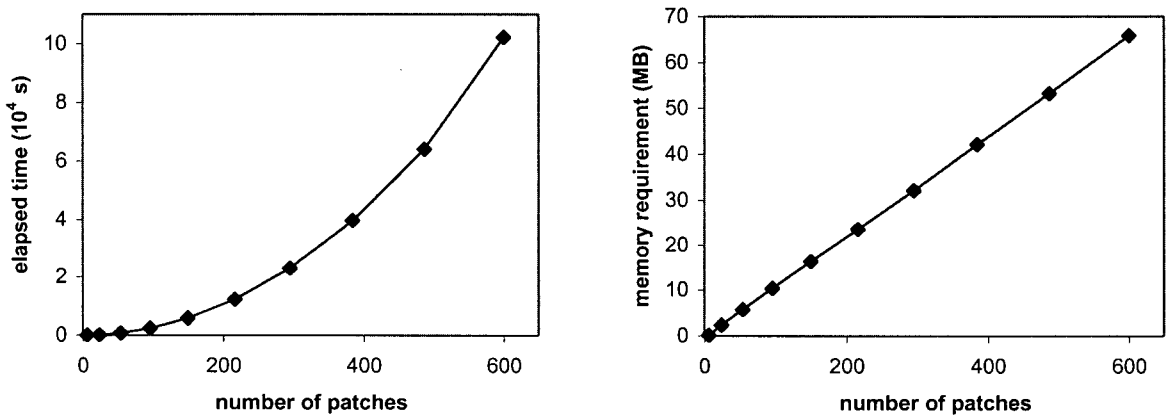

5.3.2 Predictions with varying time resolution

First, it should be recognized that the nature of time resolution in the radiosity algorithm is quite different from sampling periods used in digital systems and in measurements. In the radiosity algorithm, we are not really sampling the response every Δt seconds. Rather, energy within a time interval is summed to give the energy level for the corresponding time step. Also, phase is neglected in radiosity all together, so that signal frequency does not affect the algorithm (apart from requiring different absorption coefficients and air absorption exponents). Previous authors have referred to Nyquist's and Shannon's theorem, claiming that by these theorems, a discretization frequency ($1/\Delta t$) of at least twice the maximum signal frequency is sufficient. Because it is not clear that the application of these theorems is appropriate, they are not used here.

On the other hand, the Courant Number criterion is applicable here. The Courant Number can be expressed as $c\Delta t / \Delta x_{\min}$ where $\Delta x_{\min}$ is the minimum distance between patches. To satisfy the Courant Number criterion, we require this number to be less than one; if the Courant Number is too big, then the time resolution must be refined to satisfy the criterion. This ensures that the distance traveled in one time step is not more than the distance between patches. In all investigations performed in this research, the Courant Number criterion was satisfied by default.

To investigate the effect of resolution, further predictions were made for all cubes, with discretization periods of $\Delta t = 1/16000$, 1/12000, 1/8000/, 1/4000, 1/2000, and 1/1000 s (recall that the initial predictions had $\Delta t = 1/24000$). For these predictions, 150 patches were used to mesh the cubes (in the same way as before for 150 patches) because this number of patches was

found to be sufficient in the previous section. Once again, t_{exact} and t_{final} were set to 0.8 s and 1.0 s, respectively.

Several echograms for Cube 1 are given in Figure 5.9. Echograms for the different resolutions look quite similar. Already for $\Delta t = 1/2000$, the distinct early signals are in the same place and of the same amplitude as the ones for $\Delta t = 1/24000$. The overall amplitudes of the signals in the later parts of the echogram are smaller for finer time resolution, as expected; smaller time steps result in more time steps, each with less energy. From this we conclude that discretization periods of $\Delta t = 1/4000$ are sufficient, and that already at $\Delta t = 1/2000$ we get reasonable results.

Discretized echograms for the different time resolutions were almost identical. There tended to be slightly more energy in the early time steps for finer resolutions. This tendency reversed for later time steps (after about 0.2 s). Interestingly, this is a similar trend to that for varying patch discretization. Nevertheless, the differences for the varying time resolutions are, for all practical purposes, negligible.

Plots of the various parameters versus $1/\Delta t$ are shown in Figure 5.10. The figures are for Cube 4, which had the most significant differences in parameters for different resolutions. Figures for the other cubes were very similar.

As was the case for varying patch sizes in Section 5.3.1, the parameter predictions converged with finer resolution. *SPL* was unaffected by discretization period. This is expected because different time resolutions do not alter the total energy in the system, they only distribute it differently. Values of C_{80}, D_{50}, and *TS* changed very minimally for the different discretization (differences between predictions with $\Delta t = 1/1000$ and $\Delta t = 1/24000$ were less than 1%). The most significant changes were for *EDT* and *RT*. Even for these parameters, however, predictions for $\Delta t = 1/2000$ were within 1% of predictions for $\Delta t = 1/4000$, and the differences for predictions for $\Delta t = 1/4000$ and $\Delta t = 1/24000$ were less than 1%. As with the echograms, this suggests that discretization periods of $\Delta t = 1/4000$ are sufficient for accurate predictions.

Both time complexity and memory requirements were of order $1/\Delta t$, as would be expected. Figure 5.11 shows elapsed time versus $1/\Delta t$ and memory requirement versus $1/\Delta t$ for the predictions on Cube 1. Once again, the computer was a 2193 MHz Pentium III.

Figure 5.9. Echograms for Cube 1 with varying time resolution (range reduced to cut off direct signal, which is the same for all predictions).

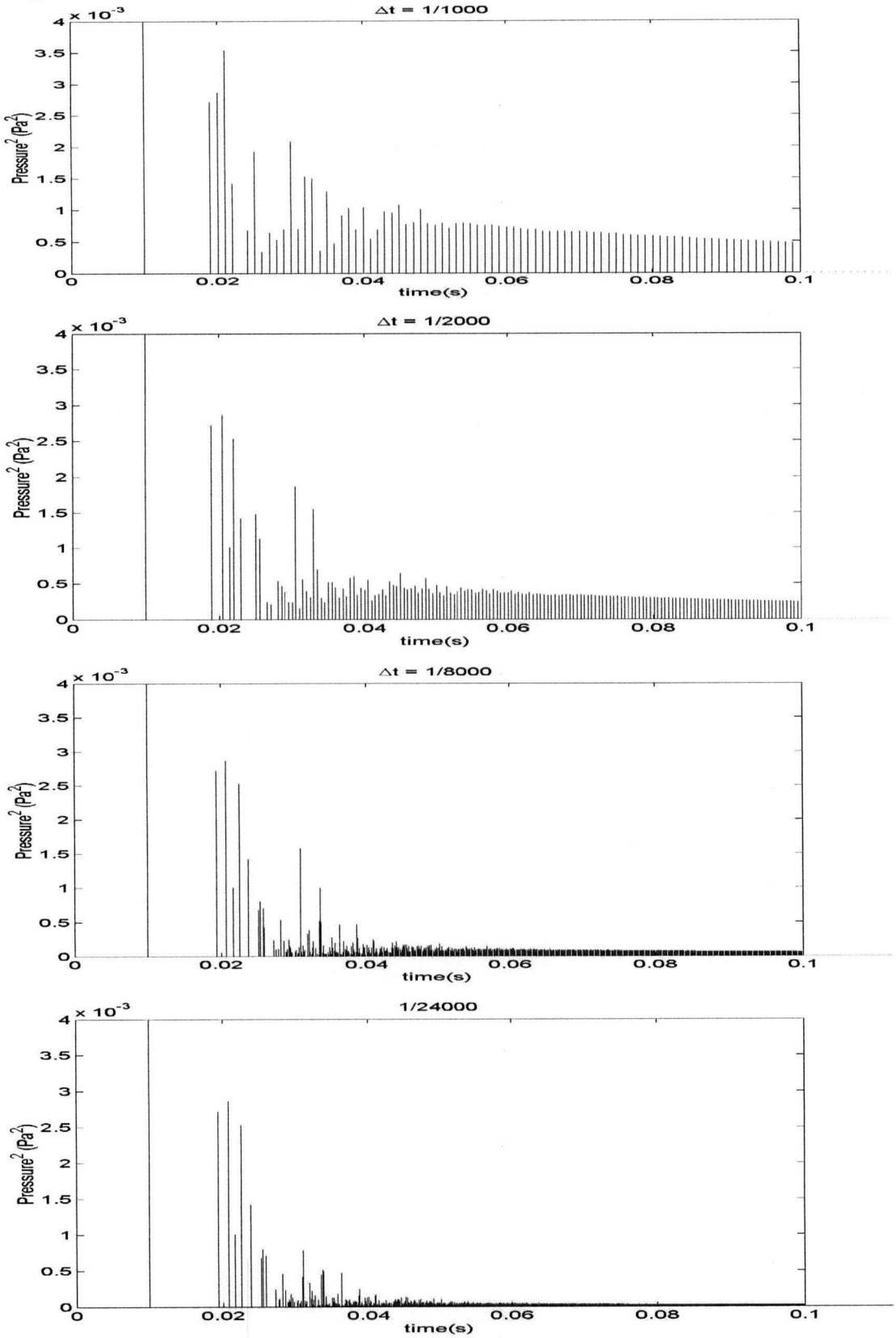

Figure 5.10. Parameter predictions versus $1/\Delta t$ for Cube 4.

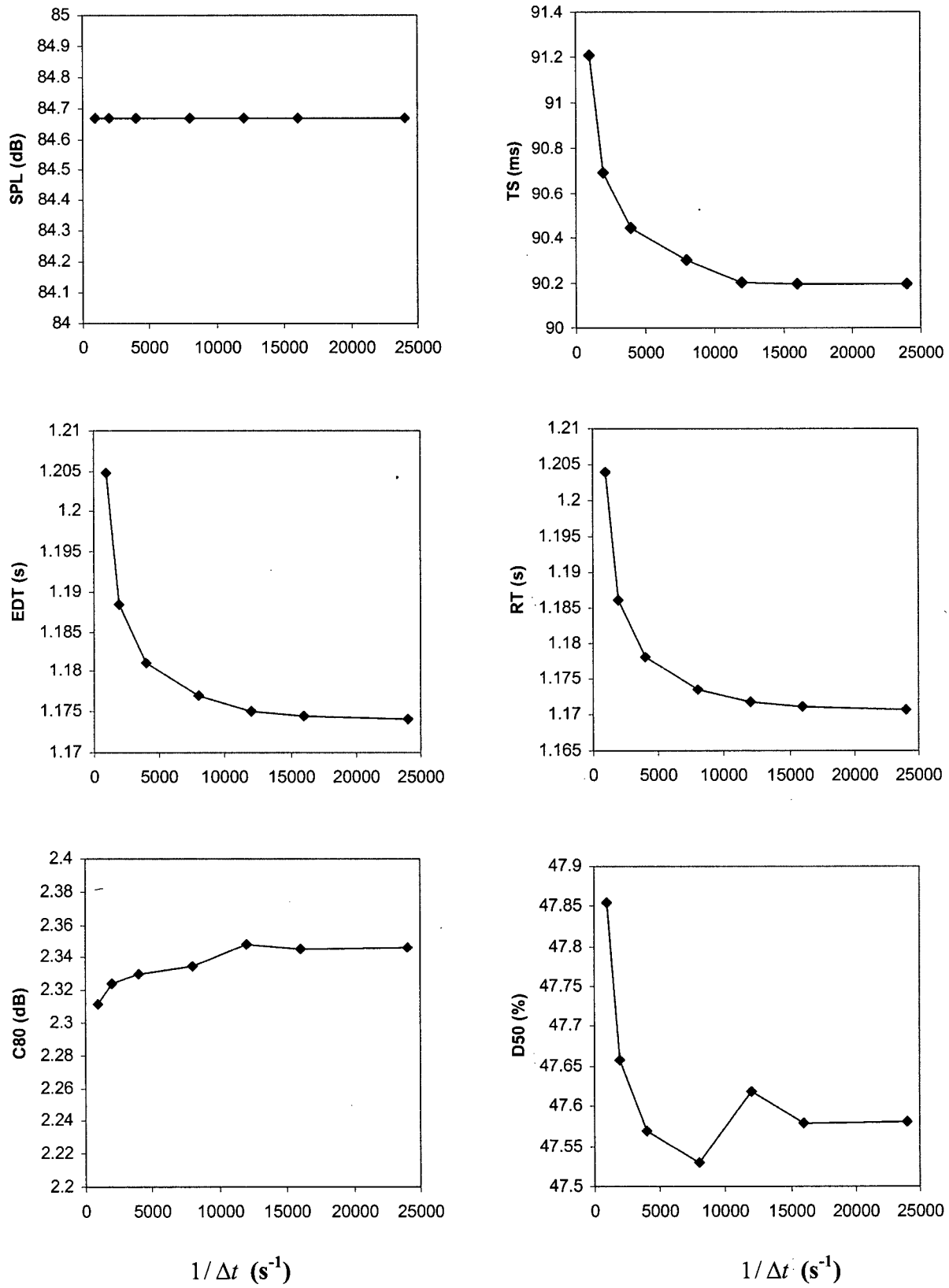

Figure 5.11. CPU time and memory requirement vs. discretization frequency for Cube 1.

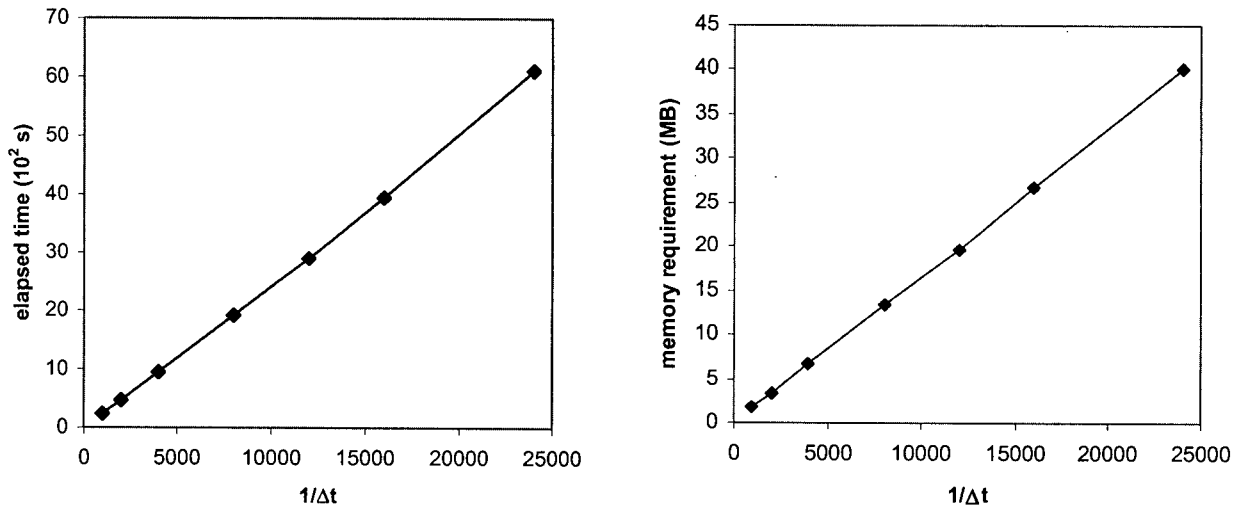

5.3.3 Predictions with varying time limits

We have shown that to get accurate predictions of reverberation time, we need to predict the impulse response to at least $t_{final_{\min}}$, as given by Eq. (5.10) (we require $t_{final} \geq t_{final_{\min}}$). Although this gives us an idea of what value of t_{final} to use in our predictions, it is still not known what time t_{exact} (to which the exact radiosity prediction is made) is necessary. It was also desirable to investigate the effect of changing t_{final} in the predictions to see if Eq. (5.10) does give the necessary minimum final time. To do so, predictions were made for the cubes with varying t_{final} and t_{exact}. In this investigation, 150 patches were used with $1/\Delta t = 12000$.

First, as an 'exact' case, a prediction was made using $t_{final} = 2$ s and $t_{exact} = 1.4$ s. This was confirmed as the limit to which predictions with increasing time converge; there was no change (up to four decimal places) in parameter predictions between this case and predictions with $t_{final} > 2$ s and/or $t_{exact} > 1.4$ s.

For the first set of predictions, t_{final} was held constant at 2 s while t_{exact} was varied (between 0.05 s and 1.4 s). In Figure 5.12, the parameter predictions for Cube 2 are plotted as a function of increasing t_{exact}. From these predictions, it became clear that reverberation time is the parameters most sensitive to changes in t_{exact}. Still, in all cubes, the *RT* prediction with $t_{exact} = 0.6$ gave less than 1% difference from the exact answer. For all the other parameters,

$t_{exact} = 0.1$ was sufficient for the same accuracy (at this exact time limit, *RT* predictions were up to 5% off).

To investigate the effect of t_{final}, another set of predictions held t_{final} constant and varied t_{exact}. Figure 5.13 shows plots of the parameters predicted with $t_{exact} = 0.6$ s and varying t_{final}. Predictions did not change significantly as t_{final} was increased beyond 1 s. This is consistent with Eq. (5.10). Indeed, the prediction with $t_{exact} = 0.6$ s and $t_{final} = 1.0$ s gave all parameter predictions within 1% of the predictions in the 'exact' case for all cubes.

5.3.4 Predictions using form factors by *HeliosFF*

Because the form factors found by *HeliosFF* are approximations (see Section 3.2.4 for details), it was necessary to check that the use of these form factors does not significantly affect predictions. For this reason, predictions were made for all four cubes under the same conditions as those outlined in Section 5.3.1. In all cases, the parameters other than C_{80} were within 1% of those found using analytical form factors (in Section 5.3.1) for the meshing with 96 patches. C_{80} came to within 1% of the analytical form factor predictions for 150 patches. Echograms and discretized echograms were also very similar to those predicted in Section 4.3.1. From this, we conclude that the approximations made in the determination of form factors by *HeliosFF* do not significantly affect predictions, particularly when a reasonably fine meshing of the enclosure is used.

5.3.5 Comparisons to ray tracing

Finally, to compare radiosity to ray tracing, predictions were made for the four cubes using *RAYCUB* (see Section 5.2.3 for details). The ray tracer was run on all four cubes for perfectly diffuse reflection, perfectly specular reflection, and 50% diffuse / 50% specular reflection from all walls. To ensure high precision, a million rays were traced for 500 reflections at a sampling frequency of 24 kHz. The receiver was a cubic cell with side-lengths of 0.1 m.

Figure 5.12. Parameter predictions versus t_{exact} (s) for Cube 2 (with $t_{final} = 2$ s).

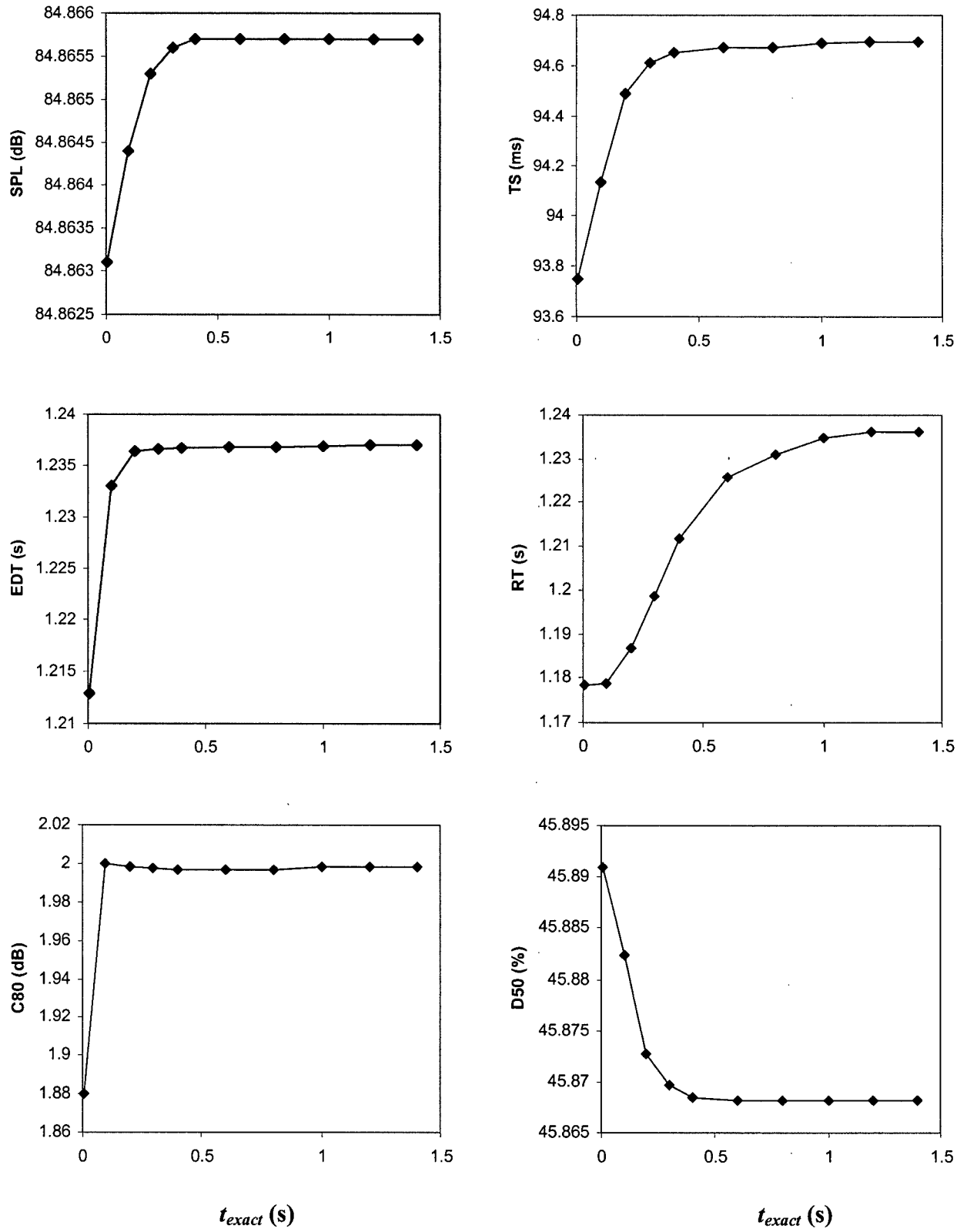

Figure 5.13. Parameters predictions versus t_{final} (s) for Cube 1 (with t_{exact} = 0.6 s).

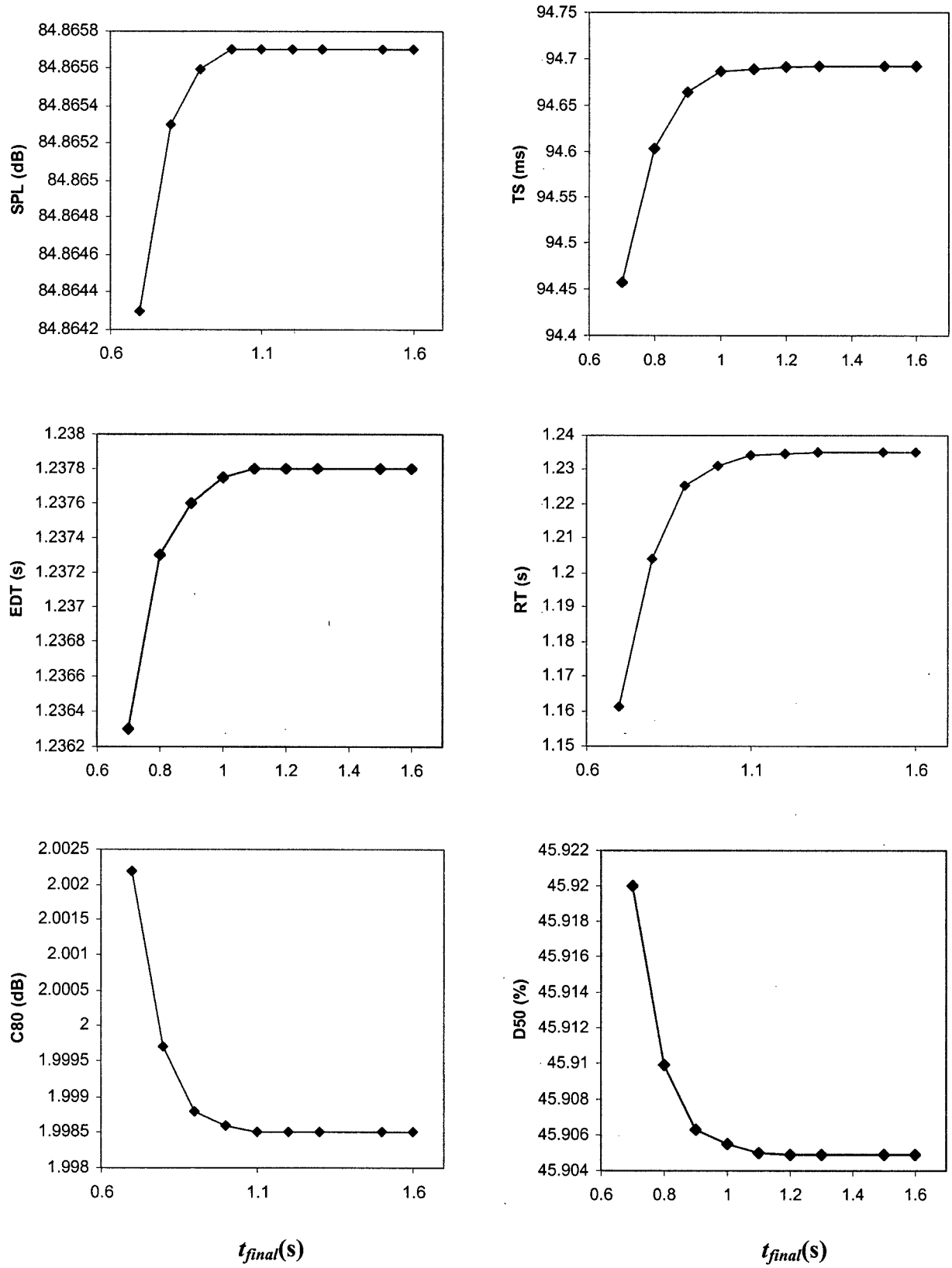

Echograms obtained by radiosity (with 600 patches and $\Delta t = 1/24000$), ray tracing with diffuse reflection, and ray tracing with specular reflection for Cube 2 are shown in Figures 5.14 and 5.15 (echograms for the other cubes were similar). The echograms are clearly quite different. The echogram for ray tracing with specular reflection has much more prominent reflections than the echogram for radiosity. This is obviously due to the specular reflections, which keep energy moving in a single direction rather than scattering it in many directions, as is the case in diffuse reflection. The echogram for ray tracing with diffuse reflection seems to lie somewhere in between the other two echograms; it has more peaks than the radiosity echogram, and less pronounced peaks and more uniformly distributed energy than the specular echogram. It seems that radiosity tends to smear the energy in time even more than ray tracing with diffuse reflection.

When the discretized echograms were compared, differences were apparent in the distribution of the energy for all cubes (see Figures 5.16 and 5.17). The larger amounts of energy in the later time steps for ray tracing with specular reflection in Cubes 2 and 3 explains the longer reverberation and early decay times and lower clarity and definition values predicted by specular ray tracing for these cubes. In general, it can be observed that total energy levels in very early time steps (before 200 ms) were quite similar between the two ray tracing predictions, whereas in later time steps, levels were more similar between radiosity and diffuse ray tracing predictions. This seems to suggest, as did observation of the echograms, that radiosity tends to smear (or diffuse) energy faster than ray tracing with diffuse reflection.

Plots of the parameters predictions for the cubes are shown in Figure 5.18 (parameters for radiosity were taken from the predictions for 150 patches in Section 4.3.1). In general, ray tracing with diffuse reflection gave predictions closer to predictions by radiosity than ray tracing with any other type of reflection. The parameter that exhibited the greatest discrepancy between predictions was *TS*, with a maximum difference of 20% for Cube 2. It should be noted that radiosity predictions for *SPL* were consistently lower than predictions by ray tracing with diffuse reflection. Similarly, radiosity predictions for *TS* were consistently lower than diffuse ray tracing, while radiosity predictions of C_{80} and D_{50} were higher. *EDT* and *RT* were both higher and lower, but radiosity and diffuse ray tracing predictions differed by less than 0.1 s (or 5%) in all cases except *RT* in Cube 2 (where radiosity predicted 1.08 s and ray tracing predicted 0.86 s reverberation time).

Figure 5.14. Echograms for Cube 2 from radiosity (600 patches), ray tracing with diffuse reflection, and ray tracing with specular reflection predictions. (Range reduced to cut off direct signal to show detail).

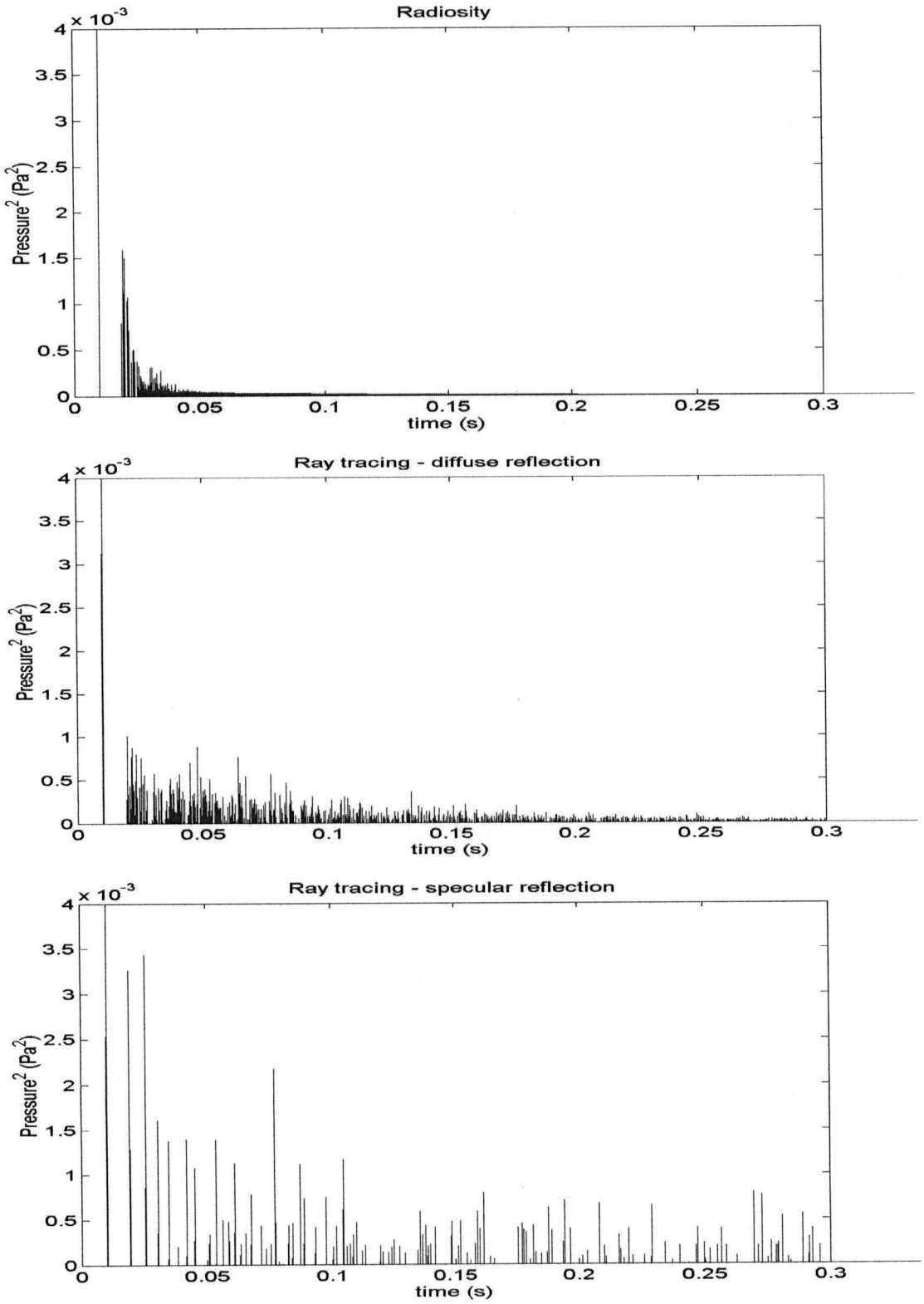

Figure 5.15. Range reduced from Figure 5.14 for more detail.

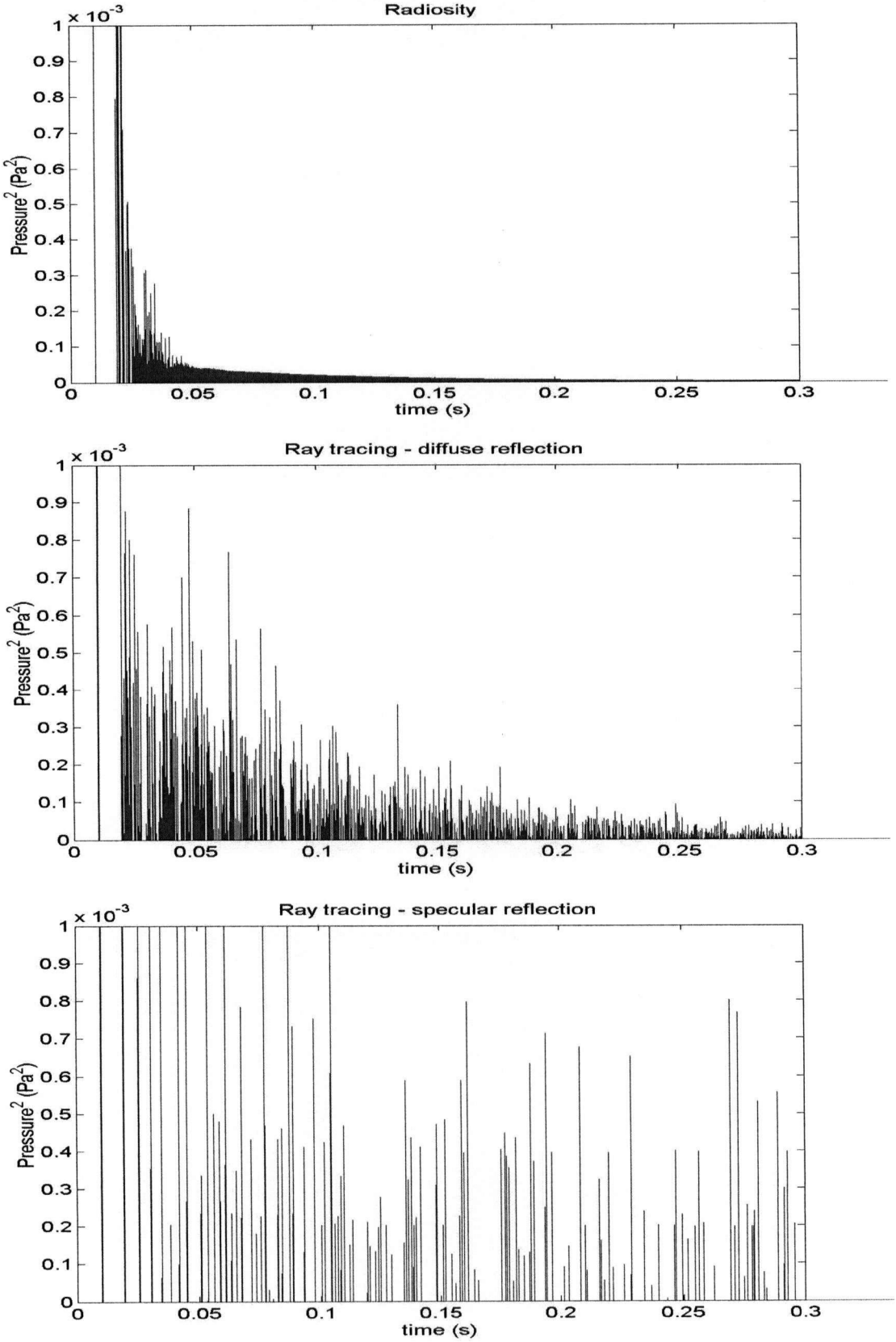

Figure 5.16. Discretized echograms for Cubes 1 and 2 by radiosity and ray tracing (diffuse and specular) with time resolution of 0.05 s.

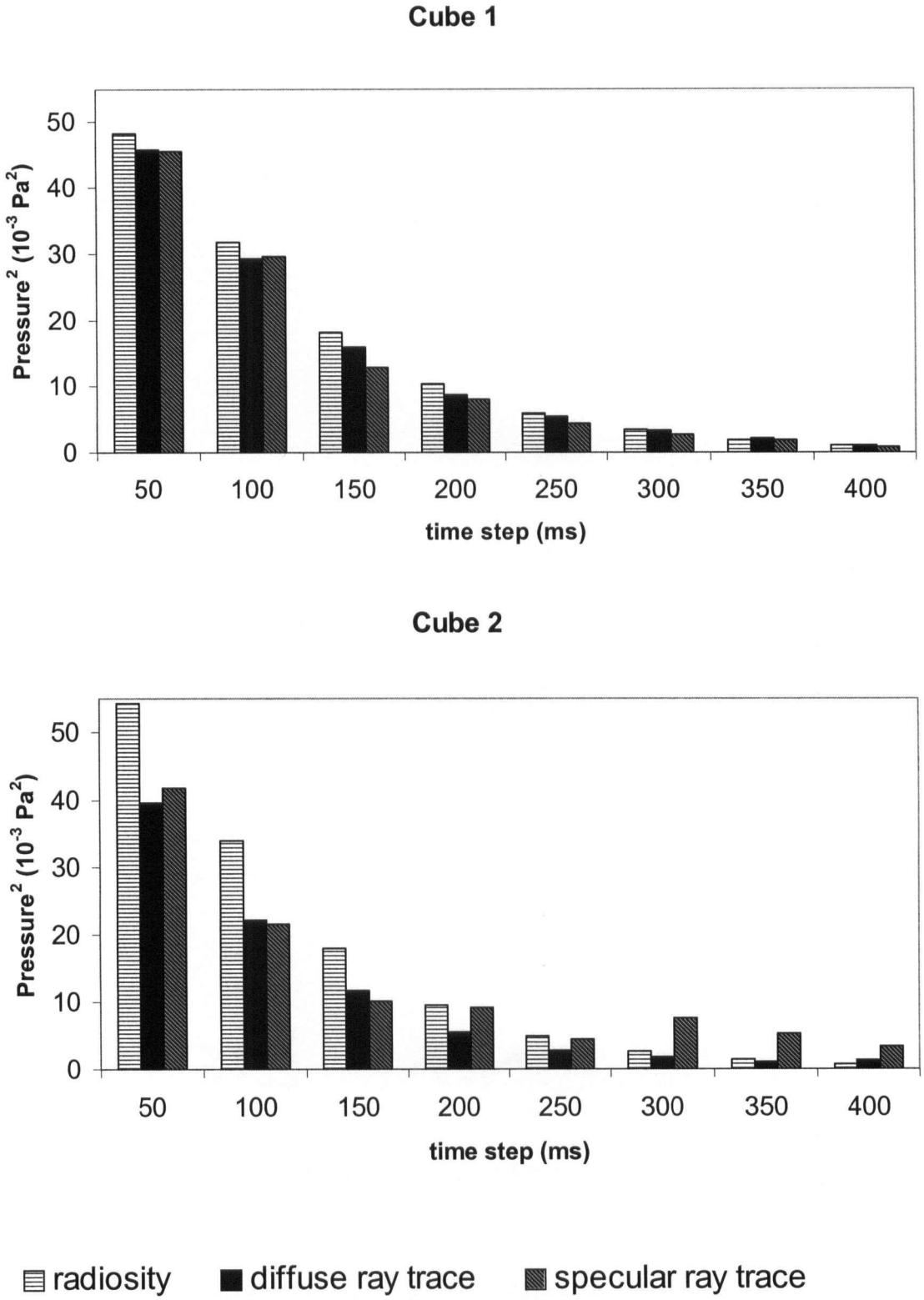

Figure 5.17. Discretized echograms for Cubes 3 and 4 by radiosity and ray tracing (diffuse and specular) with time resolution of 0.05 s.

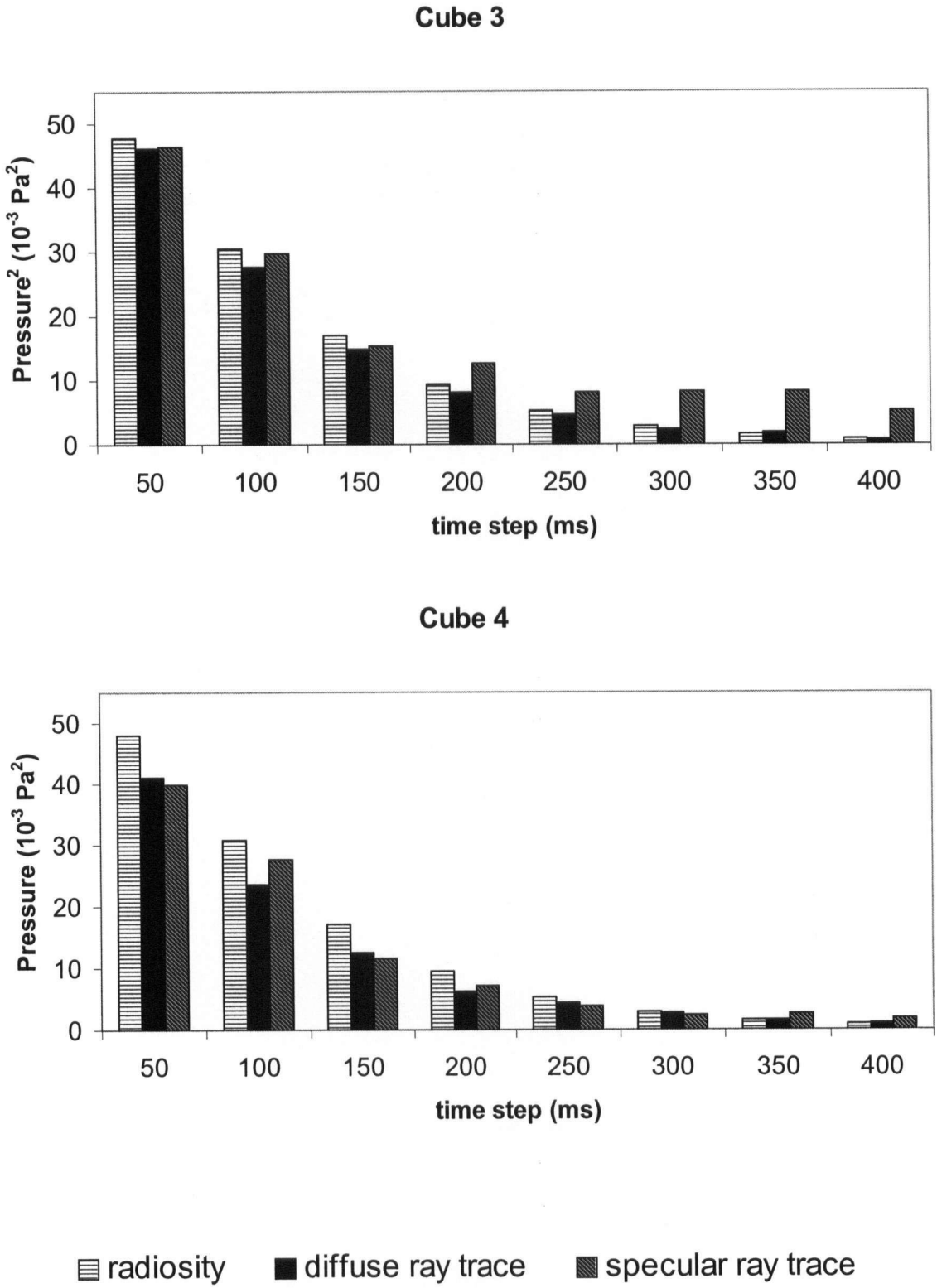

Figure 5.18. Parameter predictions by radiosity and ray tracing with diffuse, 50% diffuse/50% specular, and specular reflection for all four cubes.

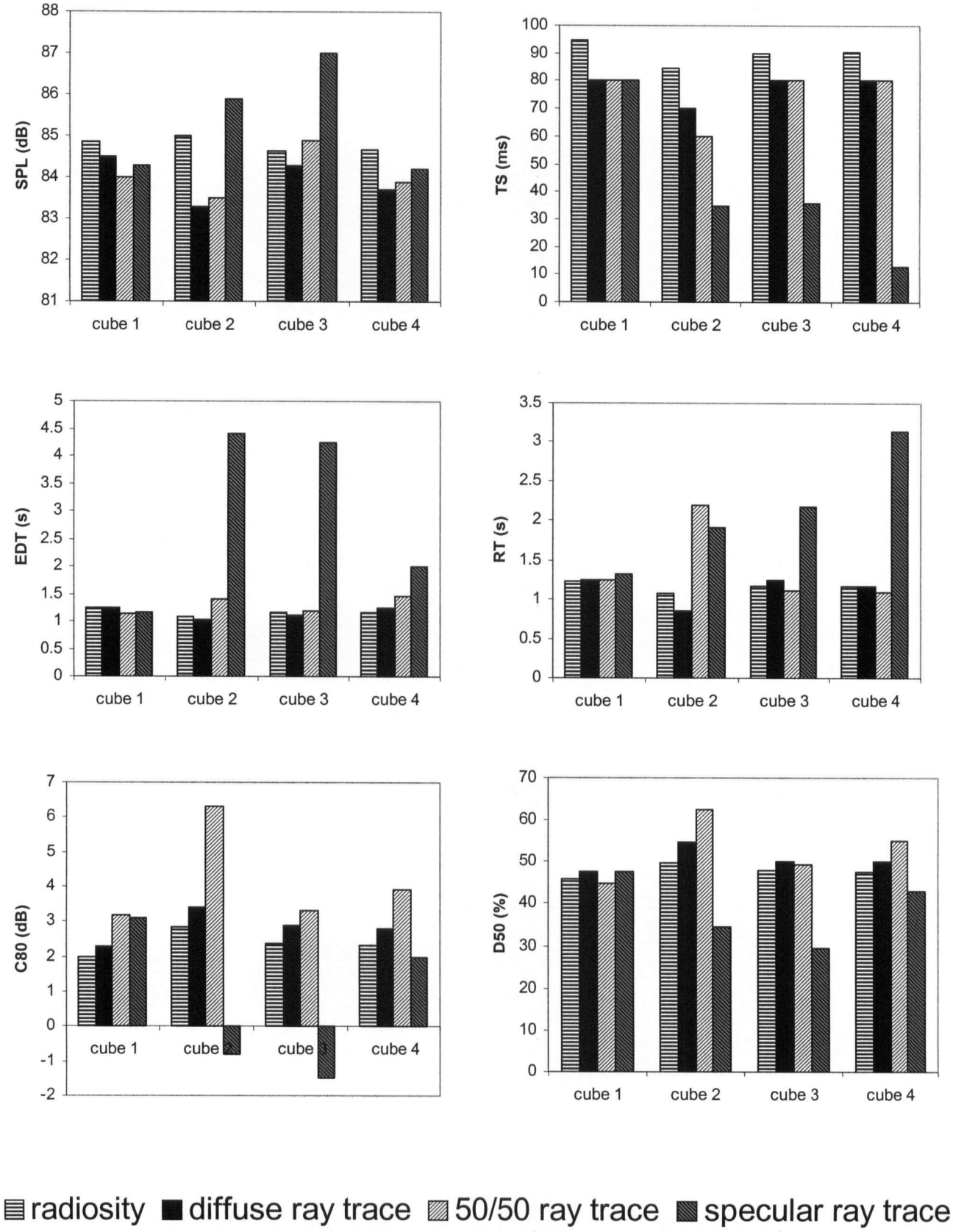

In Cubes 2, 3, and 4, specular and 50% specular / 50% diffuse reflection predictions were often quite different from predictions by radiosity and ray tracing with diffuse reflection. However, all parameters were predicted quite similarly by all methods in Cube 1. This is evidence (although far from conclusive) that, for regular enclosures (all dimensions of similar magnitude) with uniform absorption, the resulting sound field is similar, regardless of how the surfaces reflection (with respect to diffuse/specular components).

Because real room surfaces always have some specular component, it is of practical interest to compare diffuse reflection predictions with specular or partially specular predictions. It seems that the assumption of diffuse reflection results in over-estimated center times and under-estimated reverberation and early decay times. These trends were evident in all four cubes. Predictions for SPL, C_{80}, and D_{50} were variable.

5.3.6 More on ray tracing with diffuse reflection

The difference in parameter predictions, echograms, and discretized echograms for radiosity and ray tracing with diffuse reflection might be a consequence of the different manner in which diffuse reflection is incorporated in radiosity and ray tracing. Indeed, a ray in diffuse ray tracing is not scattered in all directions, as it is in radiosity, but only in one, random direction (see the description of *RAYCUB* in Section 5.2.3). Consequently, the energy of the ray is not broken into many parts, as it is in radiosity; rays with high amounts of energy retain this energy, resulting in peaks in the echogram and less smearing of energy. In radiosity, all energy is immediately scattered, so that no larger 'bundles' of energy remain intact to propagate through the system to cause peaks in the echogram. Also, because of this scattering in radiosity, energy is quickly smeared in time, giving different discretized echograms and parameter predictions.

Still, in the limiting cases (with infinitely many rays traced indefinitely with a point receiver in ray tracing, and with infinitely many patches and continuous time in radiosity) we would expect the two methods to be equivalent. It is somewhat surprising to see such obvious differences, particularly in the echograms (where the difference is most pronounced). Several attempts were made to understand this, including finer meshing of the wall in radiosity and further predictions with ray tracing. It is possible that the solutions obtained by the two methods had not converged; likely that the least converged solution was the one found by ray tracing.

Ray tracing predictions were made for a squash court (discussed in the next section) at the 1 kHz octave band with a sampling frequency of 24 kHz, a cubical receiver with 0.1 m side-lengths, and rays traced for 500 trajectories. For the same room, radiosity was run with the specifications outlined in Section 5.5 (300 patches), and with a discretization frequency of 24 kHz. Plots of the resulting echograms and discretized echograms are shown in Figures 5.19 and 5.20. The number of rays hitting the receiver for the ray tracing runs (with 1 million rays) was consistently around 18000. When the number of rays was increased to 10 million, the number of hits increased by a factor of 10 (to 178860), indicating that the solution had not yet converged for the case with 1 million rays, and that noise artifacts may be the source of the problem. In addition, even with 10 million rays, when the ray tracer was run a second time with a different initialization number, the echogram was different than it was the first time. This indicates that the solution had not yet converged, even with 10 million rays. The echogram in the case of 10 million rays looked more similar to the radiosity echogram than in the case of 1 million rays; some of the most predominant peaks were slightly reduced in amplitude. Still one certainly could not conclude that the two methods give similar echograms. When 50 million rays were used, 902014 rays hit the receiver (about 5 times the number that hit for 10 million rays). The echogram for 50 million rays looked quite similar to the one for 10 million rays; even with 50 million rays, ray tracing was not similar to radiosity. Predicted discretized echograms also changed with increasing numbers of rays, and those for ray tracing with 50 million rays were not necessarily closer to radiosity than those with fewer rays. Parameter values, on the other hand, did not change with the number of rays. It would be of interest to run the ray tracer with a much larger number of rays. This could not be done because of time restrictions (the run with 10 million rays took 15 hours on a 500 MHz Pentium III PC; the one with 50 million rays took 80 hours on a 2193 MHz Pentium III PC). There is a possibility that, with many more rays, ray tracing would converge to the radiosity solution. If this is the case, then clearly radiosity presents a more efficient way to predict the details of the echograms for rooms with diffuse reflection (the run for radiosity took about 5 hours). It may also be the case, however, that with a much finer meshing, the echogram predictions made by radiosity would be more like those by ray tracing. Very long run times prohibit an exhaustive investigation of the issue at this time. We conclude that the presented results may not represent converged solutions, but that they represent limits in the algorithms used and in current computing capabilities.

Figure 5.19. Echograms from radiosity and ray tracing with diffuse reflection in the squash court.

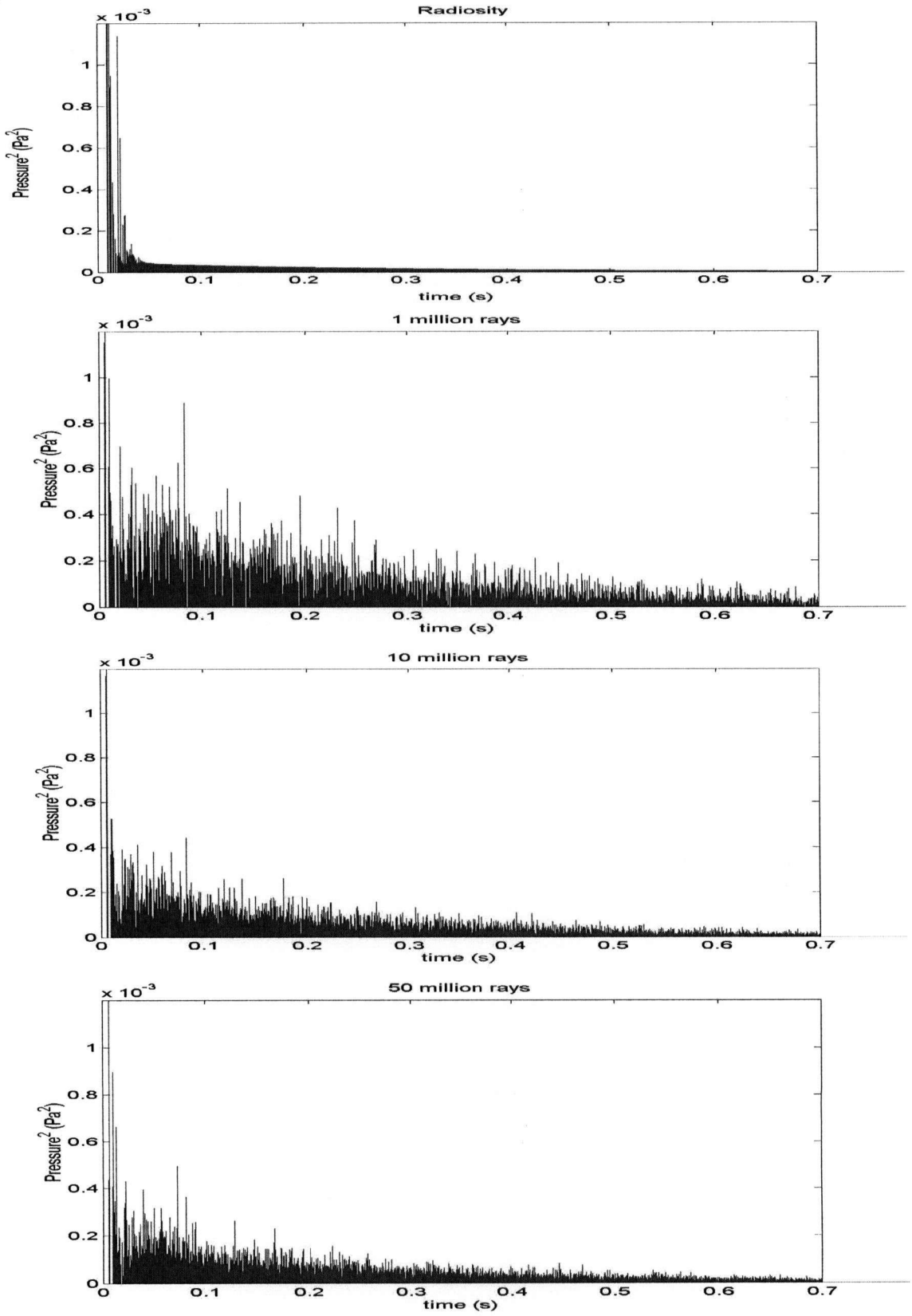

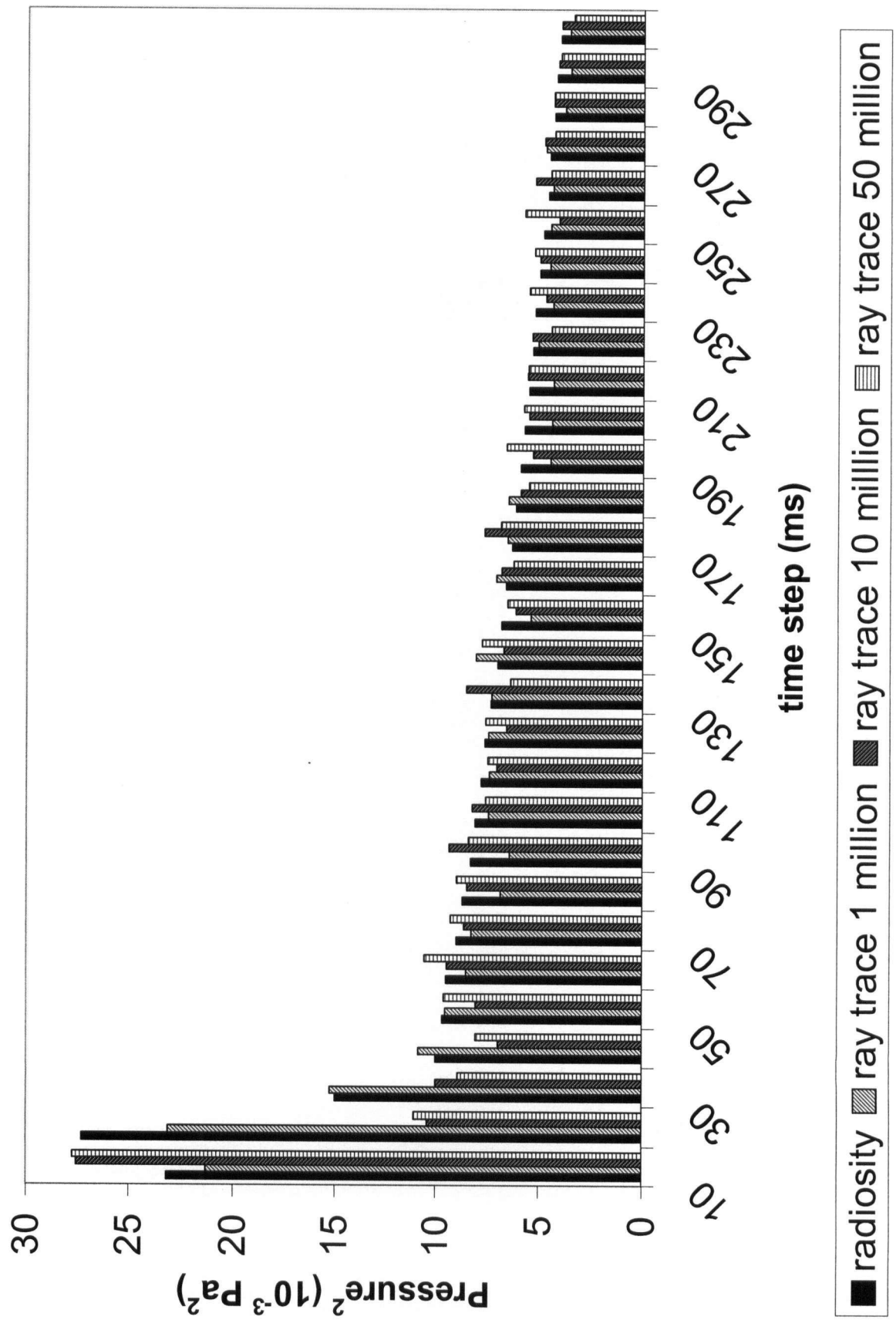

Figure 5.20. Discretized echogram from radiosity and ray tracing with diffuse reflection in the squash court.

5.4 Experiment

Through the experiments in the cubical rooms, we have explored some of the aspects of acoustical radiosity. Since we wish to investigate how acoustical radiosity performs in predicting real sound fields, we now turn our attention to experimental results and predictions in real rooms. Three rectangular rooms were used to validate the radiosity technique experimentally. The rooms were chosen with increasing non-uniformity in geometry and absorption distribution, associated with increasingly non-diffuse sound fields. This section discusses the rooms and the experimental set-up and procedure for the measurements.

5.4.1 Test Environments

5.4.1.1 Squash court

The first room was a squash court. The particular squash court used was court number one in the Dunbar Community Center in Vancouver. It is a regulation squash court with dimensions 6.40 m (width), 9.75 m (length), and 6.65 m (height). The walls and ceiling are painted concrete and the floor is varnished hardwood. Allowing access into the court, a small door is located in a corner of the front wall. Also, this particular court has a glass window along the top 2 m of the front wall for observers. The squash court was chosen for its relatively uniform geometry (width, length, and height are similar) and because all walls have similar properties. That is, the contained sound fields should be highly diffuse.

5.4.1.2 Environmental Room

The second room measured is room 369C of the Library Processing Center at the University of British Columbia. We will call it the Environmental Room. It is a small room, 3.94 m wide, 5.36 m long, and 2.71 m high. The Environmental Room has a floor of vinyl tile on concrete, four walls of drywall on 100 mm studs, and a suspended acoustical-tile ceiling. The Environmental Room was chosen for use in the validation because it is small with relatively uniform geometry but non-uniform absorption distribution (the acoustical-tile ceiling is much more absorbent than the other surfaces). It is the same room used by Ressl in her 1997 thesis [49].

Figure 5.21. Dimensions of Hebb 12.

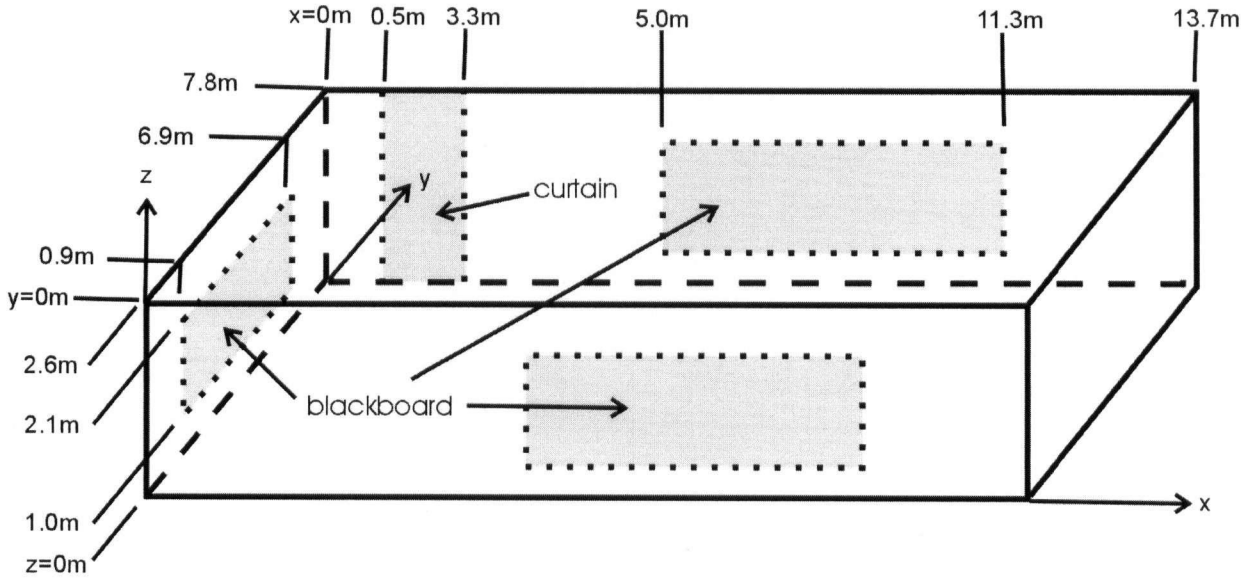

5.4.1.3 Hebb 12

The third room was a medium-sized classroom (room 12 of the Hebb building) at the University of British Columbia. The classroom, called Hebb 12, has width = 7.80 m, length = 13.70 m, and height = 2.60 m. Hebb 12 has walls of painted concrete, blackboards on the front and side walls, a short length of curtain on one side wall, a floor of linoleum tiles on concrete, and ceiling of acoustical tiles on concrete. The blackboard on the front wall has area = 7.20 m^2, while those on the side walls have area = 7.40 m^2. The curtain is 2.80 m wide and runs from the ceiling to the floor on one of the walls. Two doors are located on one side wall, one near the front and the other near the back (see Figure 5.21 for a diagram of Hebb 12). Hebb 12 was chosen because it has one dimension (the length) much longer than the other dimensions, because it has non-uniform distribution, and because its furnishings (desks and chairs) could be easily removed. Once again, Ressl previously used this room in her thesis [49].

5.4.2 Measurements

In each room, measurements were made of room impulse responses between a source and a receiver using the Maximum Length Sequence System Analyzer (*MLSSA*) [46]. The equipment used was as follows:

Figure 5.22. Experimental setup.

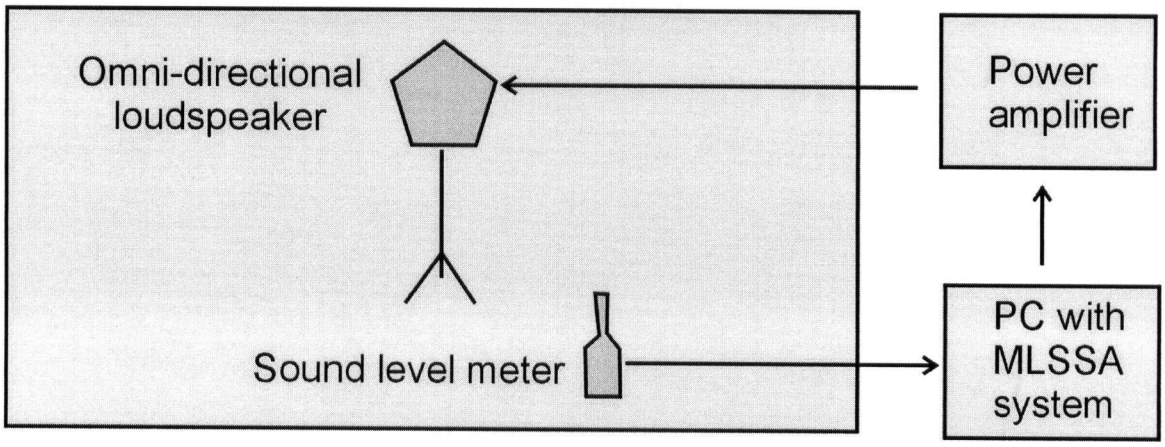

- Portable personal computer with the *MLSSA* board and software installed;
- Power amplifier: QSC Audio USA 370;
- Omni-directional loudspeaker array: Realistic model 40-1284E, dodecahedral array, frequency range 700 Hz – 20 kHz, on an adjustable stand;
- Microphone and amplifier: Rion model NA-29 (sound level meter with internal amplifier) with ½ " microphone.

The PC was located outside of the room, as was the power amplifier. The maximum length sequence signal from *MLSSA* passed through the amplifier (to be amplified) to the speaker in the room. From the signal, the speaker radiated sound energy into the room. The microphone converted the pressure at the receiver position into an electrical signal. This signal, amplified by the sound level meter, was transmitted back to *MLSSA* for analysis. The set-up is illustrated in Figure 5.22. Before measurements were made, the system was calibrated using a calibrator (pure tone at a known steady state sound pressure level) placed over the microphone, and using the *Calibrate* command.

Measurements were made for several source and receiver positions. These positions were measured and recorded. Room dimensions and the locations of the different surfaces (in Hebb 12) were also noted.

For each measurement, the response was averaged over 12 samples in the Environmental Room and 5 samples in the other two rooms (using the *Go Average* command) to increase the signal-to-noise ratio. All measurements had *MLSSA* operational parameters as follows: Acquisition length = 65536 samples (the maximum possible in *MLSSA*); Stimulus amplitude =

± 0.5332 volts. For the Environmental Room and Hebb 12 the following additional settings were used: Anti-aliasing filter bandwidth = 12 kHz; Acquisition sample rate = 36 kHz, giving a sample length of 1.819 seconds. Because of longer reverberation times in the squash court, longer samples were needed to get accurate predictions. Thus, the sample rate was decreased and, consequently, the filter bandwidth also was decreased (this insured sufficient alias suppression – see the *MLSSA* manual [46]). Settings for the squash court were: Anti-aliasing filter bandwidth = 10 kHz; Acquisition sample rate = 30.1 kHz, giving a sample length of 2.179 seconds.

MLSSA analyzes the received signal from the microphone, calculating the cross-correlation between the received response and the original signal, to find the impulse response. From this, steady state sound pressure levels, and all of the room parameters in which we are interested (*RT*, *EDT*, C_{80}, D_{50}, *TS*, and *G*) are calculated. The (unfiltered) impulse responses output to data files were then input into *MATLAB* - *MLSSA* does not output the filtered impulse responses. In *MATLAB*, the impulse responses were filtered into octave bands using a *MATLAB* function written by Ann Nakashima. The filtered impulse responses can subsequently be used for comparison with predicted impulse responses, echograms, and decay curves. Octave band filtered steady state sound pressure levels and room parameters were read directly from the *MLSSA* output display (using the *Calculate Acoustics* command).

5.4.3 Air-absorption exponents

Environmental conditions in all rooms were typically 23° C and 50% relative humidity under normal atmospheric pressure (1 atmosphere). Corresponding air absorption exponents were found using the formulas in Bass et al. [5] and are listed in Table 5.5.

The formulas of reference [5] give the air absorption coefficient, α_m and not the required air absorption exponent (see Appendix A). Also, α_m in reference [5] is in nepers/m. To convert to dB/m, recall that there are $20/\ln(10)$ decibels in a neper, so

Table 5.5. Air absorption exponents at 23° C, 50% relative humidity, and normal atmospheric pressure in 10^{-3} m^{-1}.

Frequency (Hz)	**125**	**250**	**500**	**1000**	**2000**	**4000**	**8000**
m	0.095	0.305	0.699	1.202	2.290	6.240	21.520

$$\overline{\alpha_m} = \alpha_m * 20 / \ln(10)$$

where α_m is the air absorption coefficient in nepers/m and $\overline{\alpha_m}$ is the air absorption coefficient in dB/m (this notation was chosen for consistency with reference [5]). Finally, to find the air absorption exponent, *m*, refer to Appendix B for the relationship between air absorption coefficients and exponents.

5.4.4 Source power

Before measurements were made in the rooms, the omni-directional loudspeaker was tested for omni-directionality and power output for the given setup. The same setup was used as in the actual tests, with the room being an anechoic chamber (to create a free-field environment). The anechoic chamber used is located in the Rusty Hut on the UBC campus and has dimensions of 4.7 m × 4.0 m × 2.5 m. Because the *MLSSA* operational parameters were set in two different ways for the validation experiments, two tests were done in the anechoic chamber, one with the parameters as in the squash court (bandwidth = 10 kHz), the other with the parameters as in the Environmental Room and Hebb12 (bandwidth = 12 kHz). For each test, measurements of sound power were made at three microphone positions: 'low' (below and to the side of the loudspeaker), 'medium' (on the same horizontal plane as the loudspeaker), and 'high' (above and to the side of the loudspeaker). In each position the microphone was 1 m away from the center of the loudspeaker array. For each of the three receiver positions, sound pressure level was measured 7 times, each time with the speaker rotated by about 25° from the previous measurement (until the speaker was returned to the original position). Each measurement was the average of 5 samples (using the *Go Average* command). Sound pressure levels were recorded for the seven octave bands between 125 Hz and 8 kHz. Sound pressure levels over all the positions were decibel averaged (see Appendix A) to obtain the average sound pressure level at one meter.

For omni-directional point sources in a free-field, there exists a simple formula relating sound pressure and power levels. We consider an imaginary sphere of radius *R* with the source at the center. All of the sound radiated from the source (that has not been attenuated by the air) passes through the surface of the sphere. Since the source is omni-directional, the intensity must be the same at all points on the sphere. Now,

$$I = \frac{p^2}{\rho_0 c} \quad \text{by Eq. (2.14), and} \quad W = IA$$

where I is intensity (W/m^2), p is pressure (Pa), W is power (W), and A is area (m^2) (note that this first formula applies for point sources in the far field only - i.e. for r >> $\lambda / 2\pi = 0.44$ m for 125 Hz). Combining these, and recalling that the surface area of a sphere with radius R is $4\pi R^2$, we get:

$$p^2(r) = \frac{W \rho_0 c e^{-mR}}{4\pi R^2}$$

$$\Rightarrow \frac{p^2(R)}{p_0^{\,2}} = \left(\frac{W}{W_0}\right)\left(\frac{W_0 \rho_0 c e^{-mR}}{p_0^{\,2} 4\pi R^2}\right)$$

$$\Rightarrow SPL(R) = PL + 10\log\left(\frac{W_0 \rho_0 c e^{-mR}}{p_0^{\,2} 4\pi R^2}\right)$$

where PL is the sound power level (see definitions) and SPL is the sound pressure level at distance R from the source. It follows that

$$PL = \overline{SPL} - 10\log\left(\frac{W_0 \rho_0 c e^{-m}}{p_0^{\,2} 4\pi}\right) \approx \overline{SPL} - 10.84$$

where $\overline{SPL}$ is the average sound pressure level at one meter from the omni-directional source found above. The (octave band) average sound power levels found for the two *MLSSA* operational parameter settings found by this method are given in Table 5.6. Also given in the table are the differences (arithmetic, not decibel) between the maximum and minimum measured sound power levels measured over all 21 positions for the squash court setting. For a perfectly omni-directional source, these differences are zero. From these values, we see that the source is indeed quite omni-directional at low frequencies, but that it has directional characteristics at higher frequencies, particularly above 2 kHz. This is not surprising; as such arrays are typically omni-directional only at low frequencies [36].

Table 5.6. Sound Power Levels (dB) of the source with settings for (1) the Environmental Room and Hebb 12 and (2) the squash court.

Octave Band (Hz)	**125**	**250**	**500**	**1000**	**2000**	**4000**	**8000**
setting 1: bandwidth = 12 kHz	81.18	93.81	95.01	93.77	95.90	92.27	90.50
setting 2: bandwidth = 10 kHz	81.80	94.35	95.92	95.22	96.88	95.10	92.26
maximum difference	0.70	0.70	0.50	1.20	3.30	5.90	6.70

5.4.5 Room surface absorption coefficients

Perhaps the most difficult variables to estimate for use in the radiosity algorithm are the room surface absorption coefficients. Reliable methods for measuring sound absorption - such as impedance tube methods or reverberation chamber methods [36] - could not be applied because we did not have removable samples of the surfaces. In-situ methods, such as those suggested by Li and Hodgson [42], among others, were beyond the scope of this thesis. Extensive tables of absorption coefficients of various materials and surface finishes, found by test in reverberation rooms, exist [50]. However, since it is often not possible to know the exact materials that a wall is constructed from - particularly what lies behind the surface – these tables can only act as a guideline. Even if the construction of a wall were known accurately, the actual absorption coefficient would vary somewhat from case to case. The empirical method used here, which incorporates values obtained from the tables, is outlined below.

First, the average room absorption coefficients were found from the measured reverberation times by assuming a diffuse field, based on the assumption that room sound fields are often highly diffuse with respect to reverberation time [23]. To do this, reverberation times at all the measured source/receiver positions were averaged to find the average reverberation time, RT (note that, in a diffuse field, reverberation time does not vary with position in a room). Then, by Eyring's formula (see Appendix A),

$$\bar{\alpha} = 1 - \exp\left(\frac{V}{S}\left(4m - \frac{24\ln 10}{cRT}\right)\right)$$

where $\bar{\alpha}$ is the average room absorption coefficient, V is the room volume in m^3, S is the surface area of the room in m^2, and m is the air-absorption exponent in m^{-1}.

Second, absorption was distributed among the room surfaces based on physical considerations and in such a way that the assigned absorption coefficients combined to give the average absorption coefficient found in the first step. This involved looking up the surface materials in tables of absorption coefficients (see above). Surfaces were initially assigned the coefficients found in the tables. These were then manually adjusted until the average coefficient in each band corresponded to that found from measurements. The absorption coefficients for the rooms found by this method are given in Table 5.7.

Table 5.7. Surface absorption coefficients.

Room	Surface	Area	Frequency (Hz)						
			125	250	500	1000	2000	4000	8000
Squash Court	**all**	414.96	0.103	0.065	0.048	0.044	0.043	0.030	0.024
Environmental Room	**walls**	50.41	0.060	0.050	0.030	0.020	0.030	0.040	0.030
	ceiling	21.12	0.200	0.140	0.160	0.170	0.270	0.300	0.300
	floor	21.12	0.010	0.010	0.010	0.010	0.010	0.020	0.010
	average		0.081	0.061	0.055	0.052	0.080	0.095	0.087
Hebb 12	**curtain**	7.28	0.010	0.010	0.010	0.010	0.020	0.030	0.020
	blackboard	22.00	0.010	0.010	0.010	0.010	0.030	0.040	0.020
	walls	82.16	0.020	0.010	0.030	0.030	0.030	0.040	0.020
	ceiling	106.20	0.270	0.280	0.290	0.300	0.350	0.340	0.230
	floor	106.20	0.020	0.020	0.020	0.020	0.020	0.010	0.010
	average		0.101	0.102	0.110	0.113	0.131	0.128	0.086

This method is not perfect, in that it assumes a diffuse field and estimations about absorption distribution. There is a definite possibility that error is introduced into predictions through the inaccurate estimation of absorption coefficients. These errors, and the uncertainty they introduce, are discussed further in the next section.

5.5 Comparisons between measurement and prediction

In this section, results from the measurements outlined the previous section are compared to predictions by acoustical radiosity and by ray tracing for the squash court, the Environmental Room, and Hebb 12. In all predictions discussed in this section, ray tracing was run with a million rays traced for 500 reflections, and the receiver was a cubic cell with side-lengths of 0.1 m. In the radiosity predictions, the Environmental Room was divided into 200 patches while the squash court and Hebb 12 each had 300 patches. These divisions were deemed sufficient for accurate prediction based on the discretization investigations of Section 5.3 and on several exploratory predictions that showed insignificant variation from predictions with finer meshing. Different time discretization periods and time limits were used for different sets of predictions, as are indicated in each case below.

Results were obtained for numerous source and receiver position in each room. For practical reasons, they are discussed for one source position and several receiver positions in the squash court, and one source and one receiver position for the other two rooms. The echograms, discretized echograms, and parameters in the positions chosen for discussion were characteristic

of most of the other positions measured. In all rooms, the 'front' refers to one of the walls with the shortest dimension, and all sources and receivers were centered side-to-side. For the squash court, the source was located 1.00 m from the front of the court and 1.9 m above the floor. Eight measurement positions are discussed, each 1.05 m from the ground. The first position was 2.00 m from the front wall, the second was 3.00 m from the front, and so on, with the eighth position 9.00 m from the front. Corresponding source to receiver distances were 1.31 m, 2.17 m, 3.12 m, 4.09 m, 5.07 m, 6.06 m, 7.05 m, and 8.05 m. The source in the Environmental Room was 1.10 m from the front wall and 1.72 m high, while the receiver was 3.25 m from the front and 0.90 m high, giving a source to receiver distance of 2.30 m. The measurements discussed in Hebb 12 are for a source 6.00 m from the front and 1.60 m above the ground, and for a receiver 7.60 m from the front and 1.40 m high, giving a source to receiver distance of 1.61 m. See Figure 5.23 for section sketches of the three rooms showing source and receiver positions.

5.5.1 Echograms

Figure 5.24 shows echograms for the 1 kHz octave band obtained from measurements and predictions with radiosity and ray tracing (with diffuse and specular reflection) in the squash court; Figures 5.25 and 5.26 show echograms at 1 kHz for the Environmental Room and Hebb 12, respectively. For meaningful comparison, predicted echograms for the squash court (with both radiosity and ray tracing) were made using time discretization frequencies of 30.1 kHz, which was the sampling frequency used in the measurements of the squash court. Similarly, predicted echograms for the other two rooms used discretization frequencies of 36 kHz. Echograms were predicted up to 1 s by ray tracing, and to $t_{exact} = t_{final} = 2$ s by radiosity, but are shown for shorter durations in the figures. The echograms for the squash court are for the second receiver position in that room.

Figure 5.23. Source and receiver positions in the three measured rooms. All distances in meters. Source ⬠; Receiver ○.

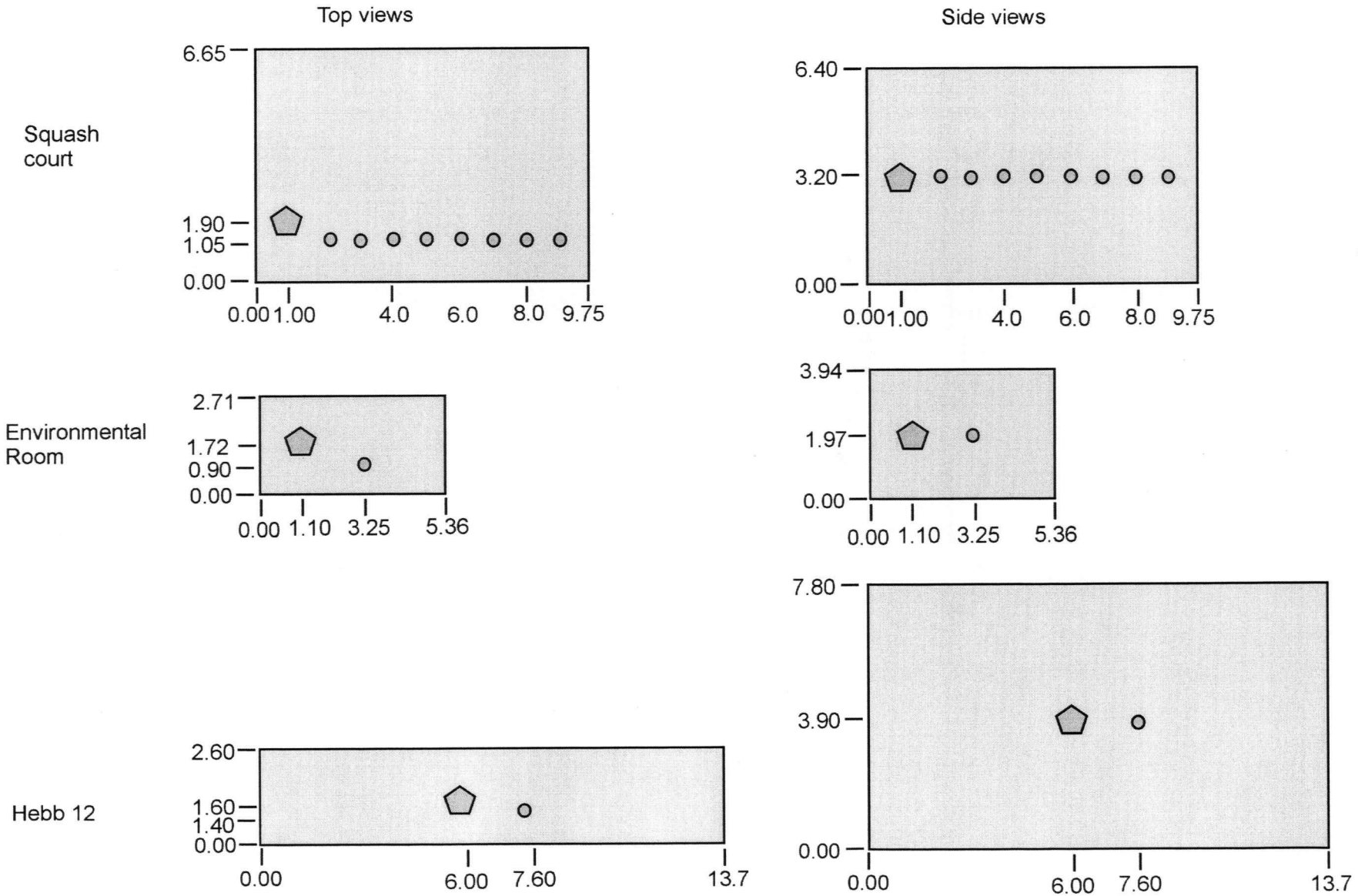

Figure 5.24. Measured and predicted echograms in the squash court at 1kHz.

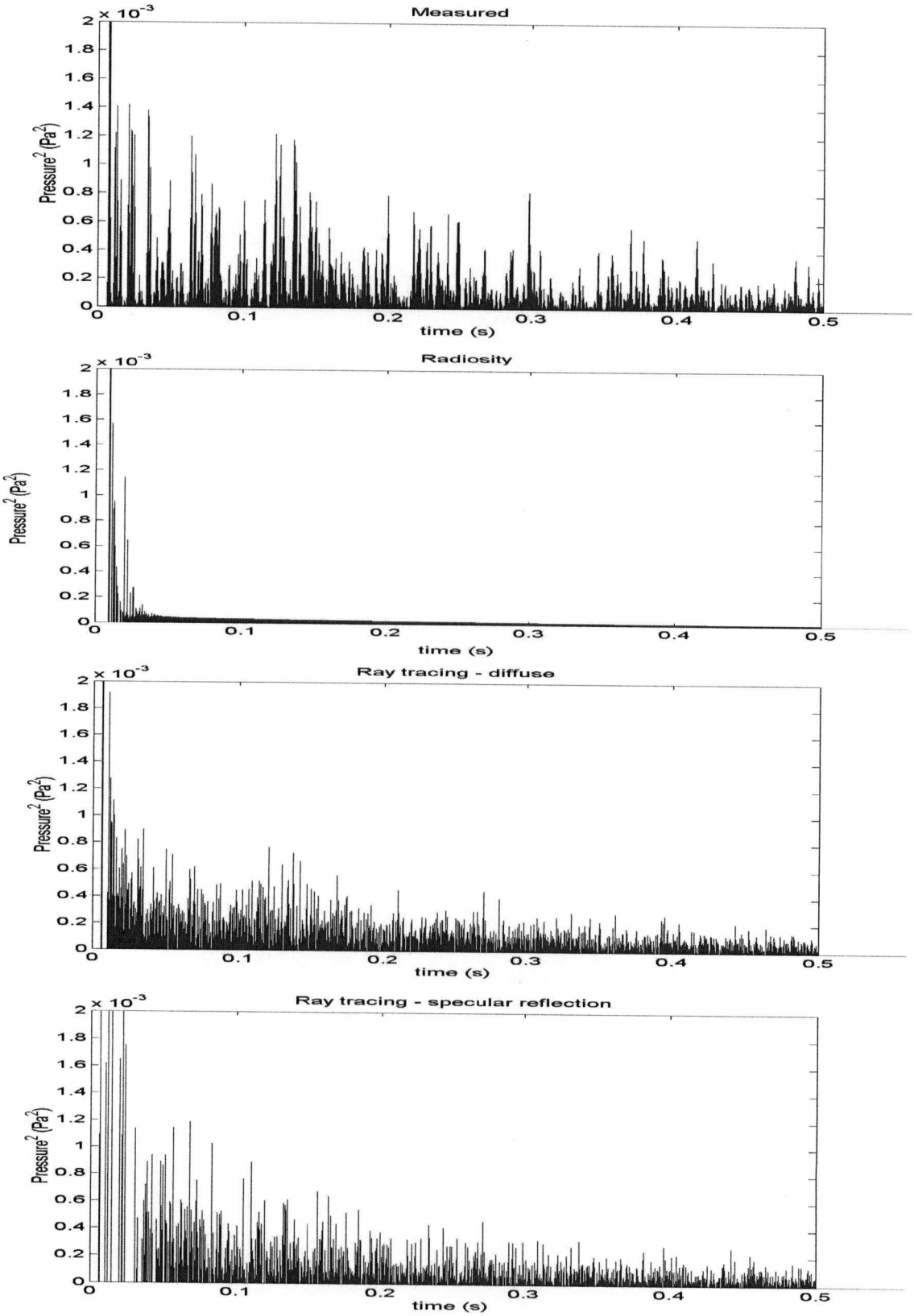

Figure 5.25. Measured and predicted echograms in the Environmental Room at 1kHz.

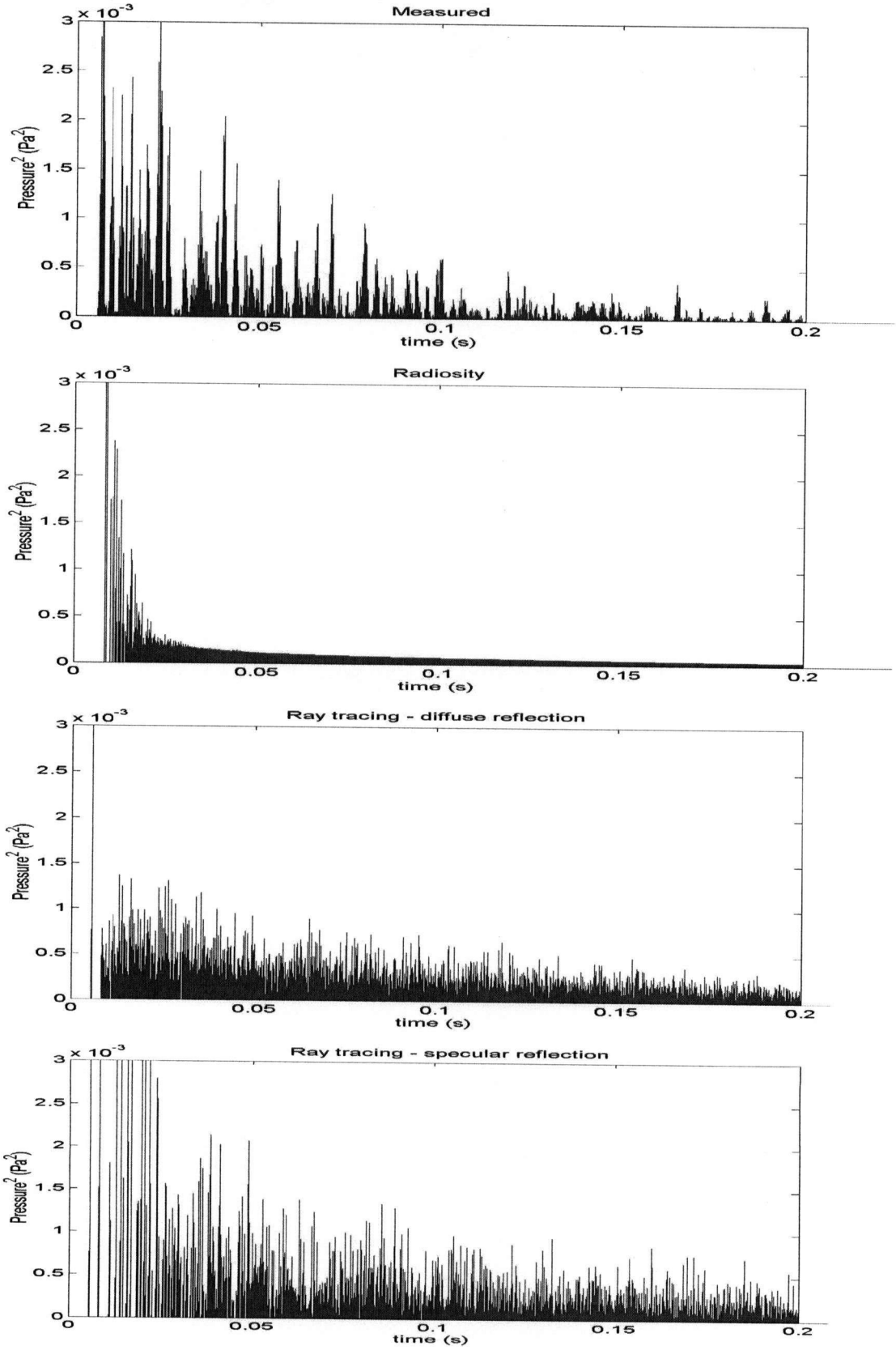

Figure 5.26. Measured and predicted echograms in Hebb 12 at 1kHz.

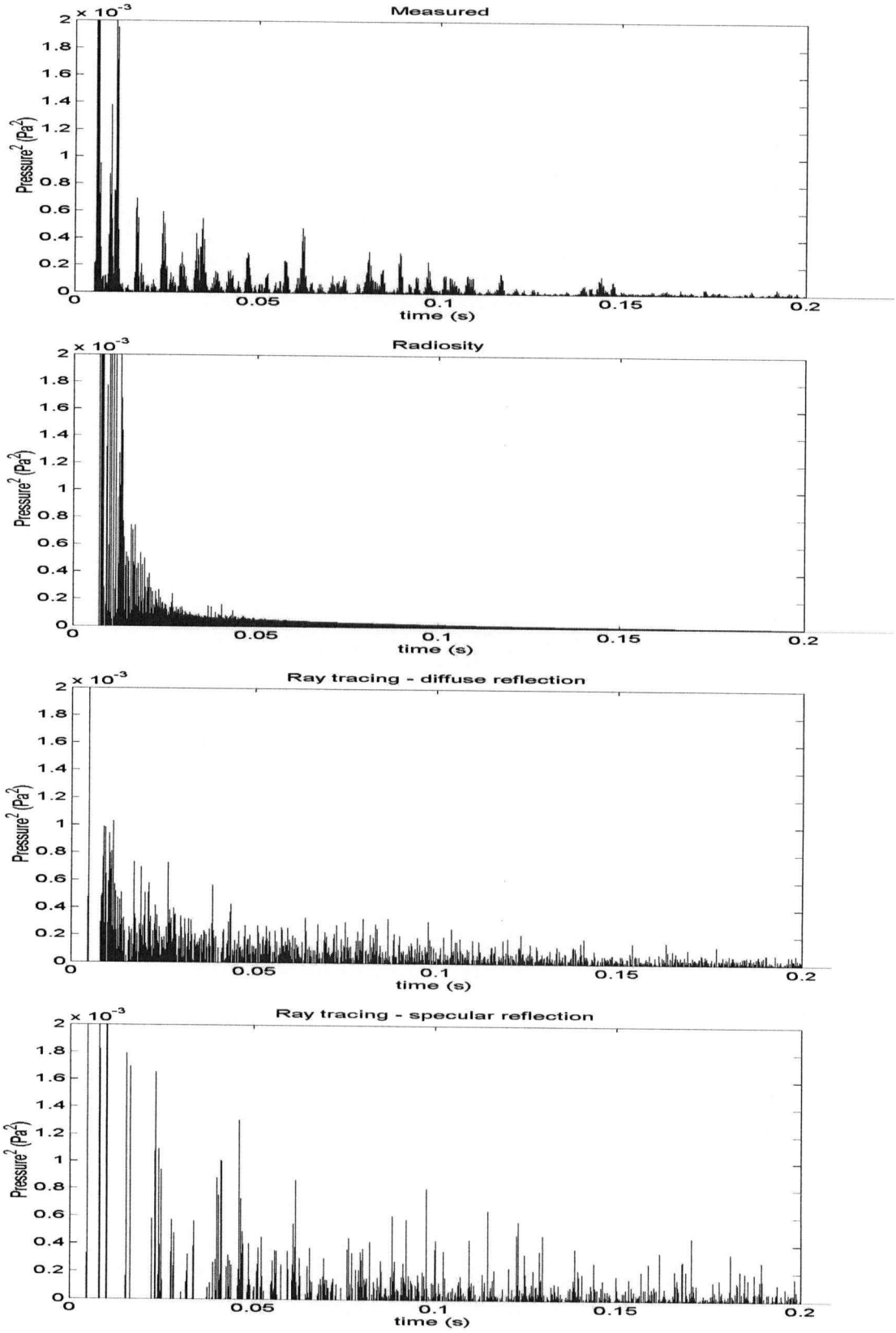

In all cases, the echograms looked quite different. The differences between echograms predicted by radiosity and by ray tracing were similar to those seen and discussed in Section 5.3. In all of the rooms, the echograms predicted by radiosity were least similar to the measured echograms. Strong and distinct peaks in the measured echograms in all three rooms are completely lost in radiosity predictions. Having said this, a comparison of the later part of the echograms shows less extreme differences between measured and radiosity-predicted echograms, particularly in echograms for Hebb 12 and the Environmental Room past 0.15 s. The energy in radiosity is still more smeared than as measured, but the strong reflections that characterize the early part of the measured echograms are no longer present. On the other hand, there still are some distinct reflections present in the later part of the echogram predicted by specular ray tracing. This can be explained by recalling the discussion of the transformation of specular to diffuse energy in a room from Section 1.3. In particular, in the later part of the decay, we might expect more diffuse reflection than specular, so that a predictions method that assumes diffuse reflection, such as radiosity, should give better predictions. For this reason, measured echograms might be most closely predicted by incorporating both specular and diffuse reflection (possibly by using ray tracing with a mix of specular and diffuse reflection, or possibly by a hybrid method that uses a model with specular reflection for the early predictions and radiosity for the late part).

To better understand the distribution of the energy in the measurement and predictions, we turn once again to discretized echograms.

5.5.2 Discretized echograms

The same data that was used to plot the echograms in the previous section was used to find the discretized echograms for the three rooms, as shown in Figures 5.27-5.29. The time resolution used to obtain these figures was 0.01 s. Interestingly, the three prediction methods give similar discretized echograms. Nevertheless, it is evident from these discretized echograms that none of the prediction methods accurately predicts the distribution of energy with time.

Figure 5.27. Discretized echograms for the squash court at 1 kHz.

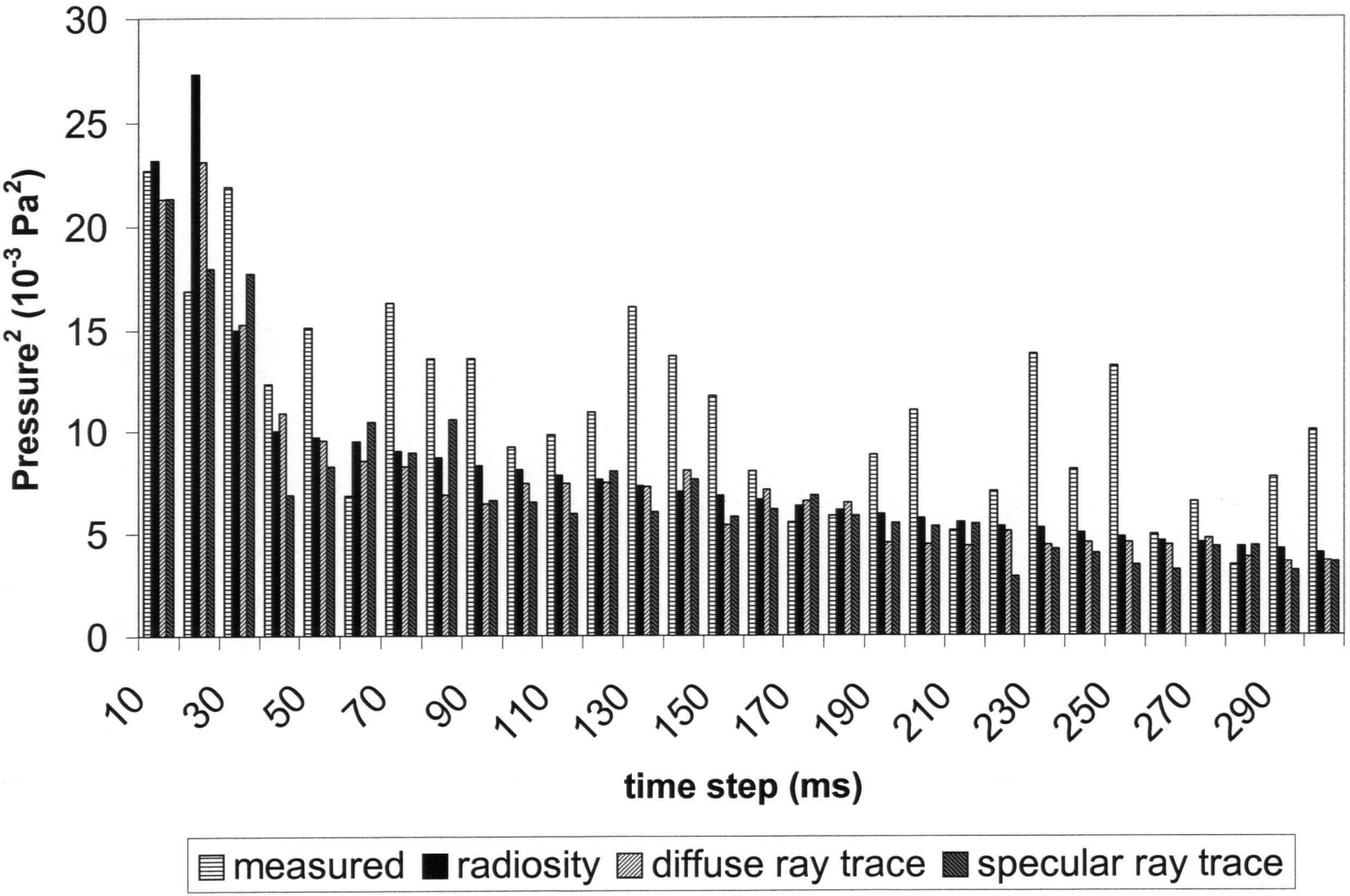

Figure 5.28. Discretized echograms for the Environmental Room at 1 kHz.

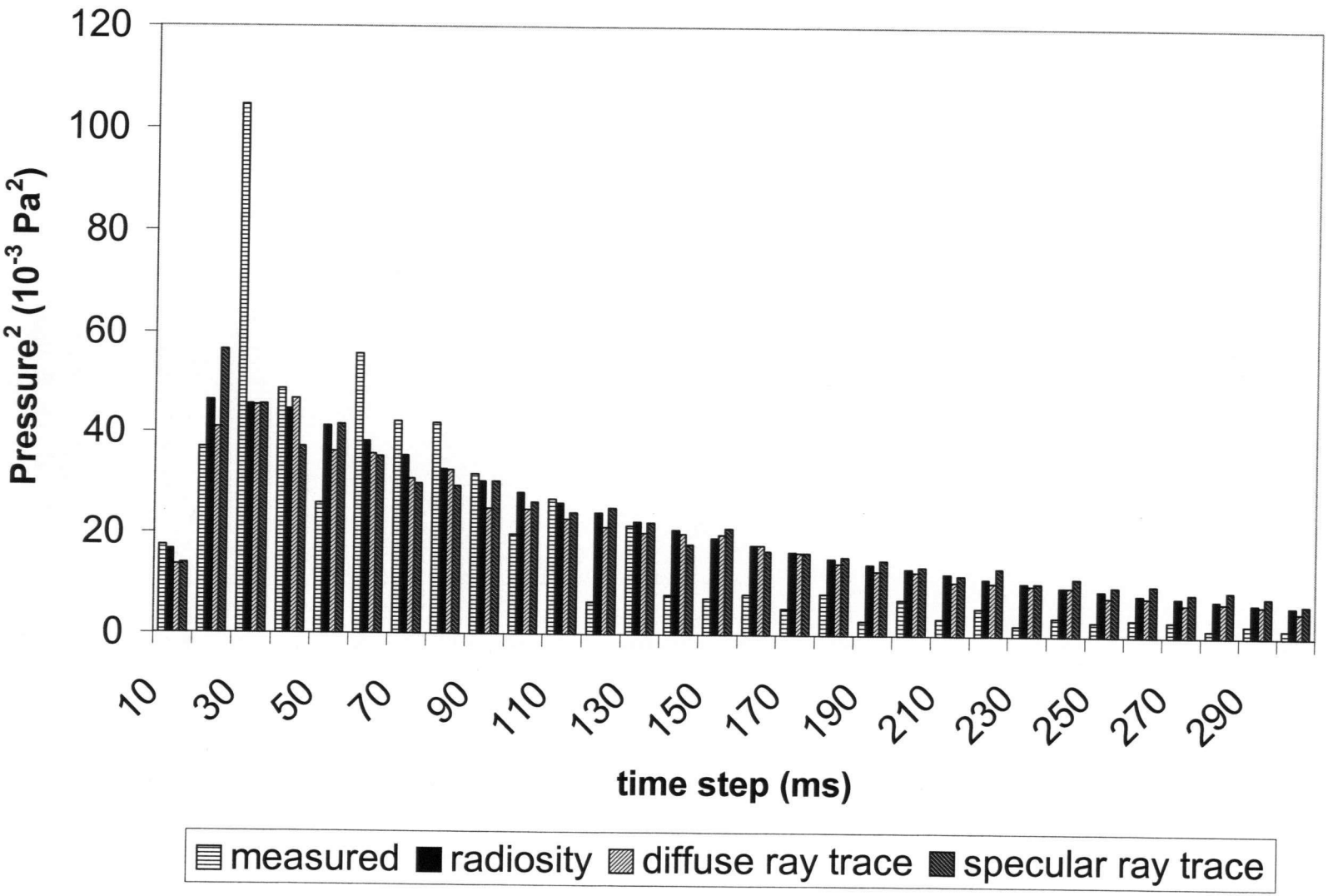

Figure 5.29. Discretized echograms for Hebb 12 at 1 kHz.

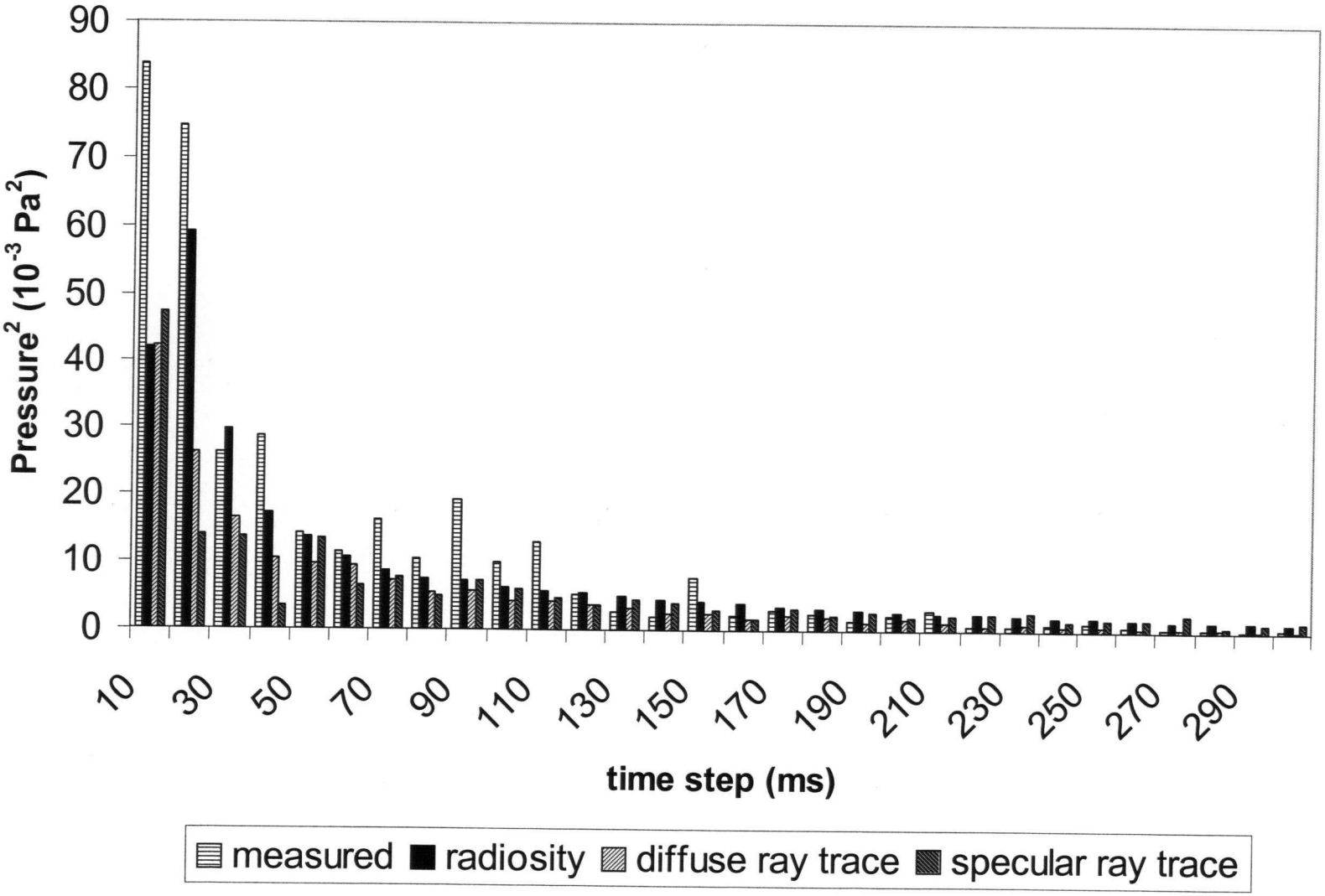

Most clearly seen in the discretized echogram for the squash court, the measured echograms show a fluctuation of energy with time. In particular, pressure levels in the time intervals do not decrease monotonically with time, but rather alternate between decreasing and increasing (with a gradual, overall decrease). These fluctuations are not reproduced in radiosity, for which the decay of energy with increasing time steps is monotonically decreasing. Both versions of ray tracing, particularly with specular reflection, do capture part of the fluctuations, although not nearly to the same extent as is measured. Part of the reason for such fluctuations may be rays, which reflect specularly, bouncing between parallel walls. This would explain why ray tracing captures them to some degree, and why they are lost completely by radiosity. This reason is also consistent with the observation that fluctuations are more pronounced in the squash court, which might be expected to have the most specularly reflecting walls of all the rooms. The fluctuation may also be caused my modal effects, which are lost in both ray tracing and radiosity.

In the discretized echograms of the Environmental Room and of Hebb 12, energy levels in the very early time steps (before 100 ms) are predicted to be much lower than as measured (by both radiosity and ray tracing). This is reversed for time steps later than 100 ms in both rooms, with more energy in the predicted discretized echogram than in the measured. These observations are consistent with observations that can me made about differences in the measured and predicted parameters.

5.5.3 Acoustical parameters

Figure 5.30 shows the measured and predicted parameters at 1 kHz in the squash court for the eight measurement positions (the first being closest to the source, the eight being the farthest, refer again to Figure 5.23). With the exception of reverberation time, all three prediction methods give similar parameter values. Worth noting is that, while radiosity and ray tracing with diffuse reflection predict parameters that tend to vary monotonically (either increasing or decreasing), or stay constant (in the case of *RT*), with distance from the source, parameter values from measurement and ray tracing with specular reflection do not behave this way. Rather, measurement and specular ray tracing parameters fluctuate higher and lower as the receiver is moved away from the source. This effect is evident for all parameters, and may be caused by specularly reflected rays bouncing between parallel walls (as we suggested for the fluctuations in the discretized echograms for the squash court).

Figure 5.30. Parameter values as a function of position in the squash court at 1 kHz.

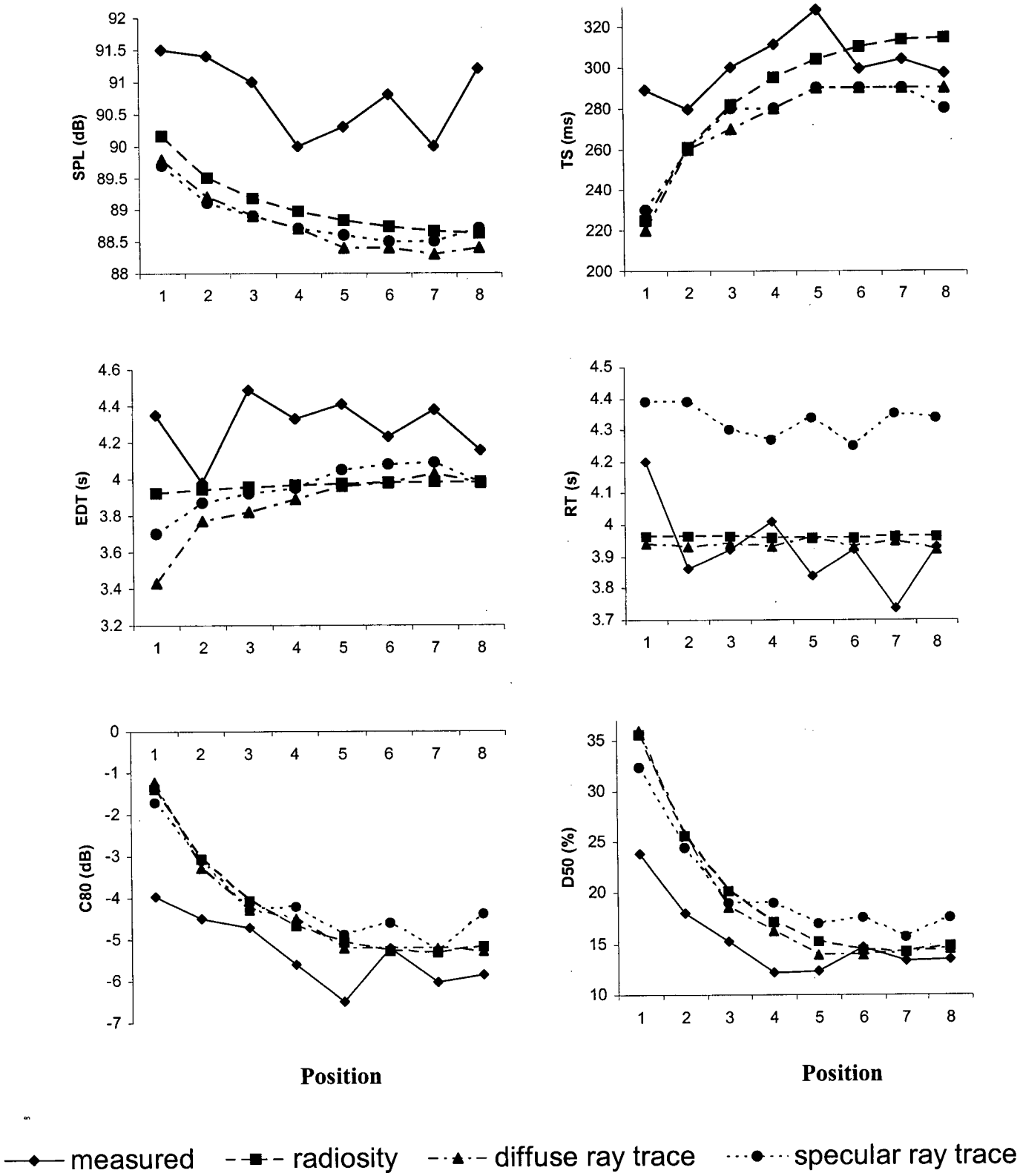

All prediction methods underestimated the steady state sound pressure levels, with radiosity giving the best prediction. The maximum difference between measured and predicted levels (by radiosity) was 2.8 dB. Though this corresponds to only a 3% difference, it is certainly not close, since an increase in *SPL* of 3 dB roughly corresponds to a doubling of source power (by the log in the definition of sound pressure level). The considerably higher measured pressure levels in the discretized echograms for squash court are consistent with the higher measured *SPL*s.

The cause of this large difference in sound pressure levels is not immediately evident. A possible reason is an over-estimation of the absorption coefficients of the walls. This reason is questionable, however, because at some positions (particularly those close to the side walls), predicted *SPL*s were much closer to the measured values, sometimes even higher. Also, this would not be consistent with the predictions for the other parameters (such as low predicted *EDT*s). The difference may alternately be the result of directionality of the source. In particular, the source may not be completely omni-directional as was assumed for the predictions. This might explain why predicted and measured levels are more similar near the side walls. At larger source-receiver distances, however, directionality should not have such a significant effect. Also, if directionality were the cause, we would expect more energy in the first time step in the measured discretized echogram (corresponding to the direct signal from the source), which is not the case. Another possible source of error is in the calibration of the source.

Clarity and definition were both over-estimated by all prediction methods. This can be seen in the discretized echograms, where less energy is measured in the early time steps (before 80 ms) and more in the late time steps (after 80 ms). Differences improved for longer source-receiver distances. Center time was predicted below measured values, expect at the last three receiver positions, where radiosity predicted higher values than measured. This is consistent with the C_{80} and D_{50} predictions and with the discretized echograms; less early energy (measured) results in higher center time.

All prediction methods gave early decay times that were lower than the measured values. Differences between measurement and radiosity predictions were never greater than 12%, while ray tracing had differences up to 23%. Once again, predictions tended to improve with increasing source-receiver distance.

Similar reverberation time predictions by radiosity and ray tracing stayed almost constant with varying receiver position, with measured *RT*s both higher and lower than the predicted values. The difference was always less than 7%. Constant reverberation time with varying position is characteristic of a diffuse field. Worth noting is that RT predicted using Eyring's formula is 3.36 s, which is just 0.3 s lower than the values predicted by radiosity and ray tracing with diffuse reflection. *RT* predictions by ray tracing with specular reflection were notably higher than the other predictions and measurement.

Overall, it seems that measured parameters in the squash court were more closely predicted by radiosity than by either version of ray tracing. This would not necessarily be expected, since the walls of the squash court would be expected to be quite highly specularly reflecting. This observation applies for most measurements made in the squash court, including those made in different octave bands (than 1kHz). These are presented next.

In Figures 5.31-5.33, parameter predictions and measurements in the three rooms are plotted for the 7 octave bands from 125 Hz to 8 kHz. The fifth receiver position in the squash court was taken for these figures. The first thing to note is that there is little consistency in the differences between measurements and prediction methods. For example, we cannot say that, in general, radiosity predicts higher or lower values for some parameters than measured or than predicted by ray tracing, because each case is different. One tentative, general observation that might be suggested is that ray tracing with specular reflection tends to predict higher center, reverberation, and early decay times than any of the other methods. This trend was also apparent in predictions made for the cubical rooms in Section 5.3 for *RT* and *EDT*.

Another such general observation that can be made is that *TS*, *EDT*, and *RT* found by one method were generally all either higher or all lower than another method in a given room (with some exception in the squash court). For example, in the Environmental Room, specular ray tracing predicted the highest *TS*s, *EDT*s, and *RT*s, radiosity the second highest, specular ray tracing the third highest, and measurement the lowest. The same observation can be made about C_{80} and D_{50}. Further, if a method gave higher *TS*, *EDT*, and *RT*, it generally gave lower C_{80} and D_{50}. This can be understood by thinking of higher *TS*, *EDT*, and *RT* as corresponding to slower rate of decay. Slower decay means less early energy and, consequently, lower clarity and definition.

Figure 5.31. Parameter values as a function of frequency (Hz) in the squash court.

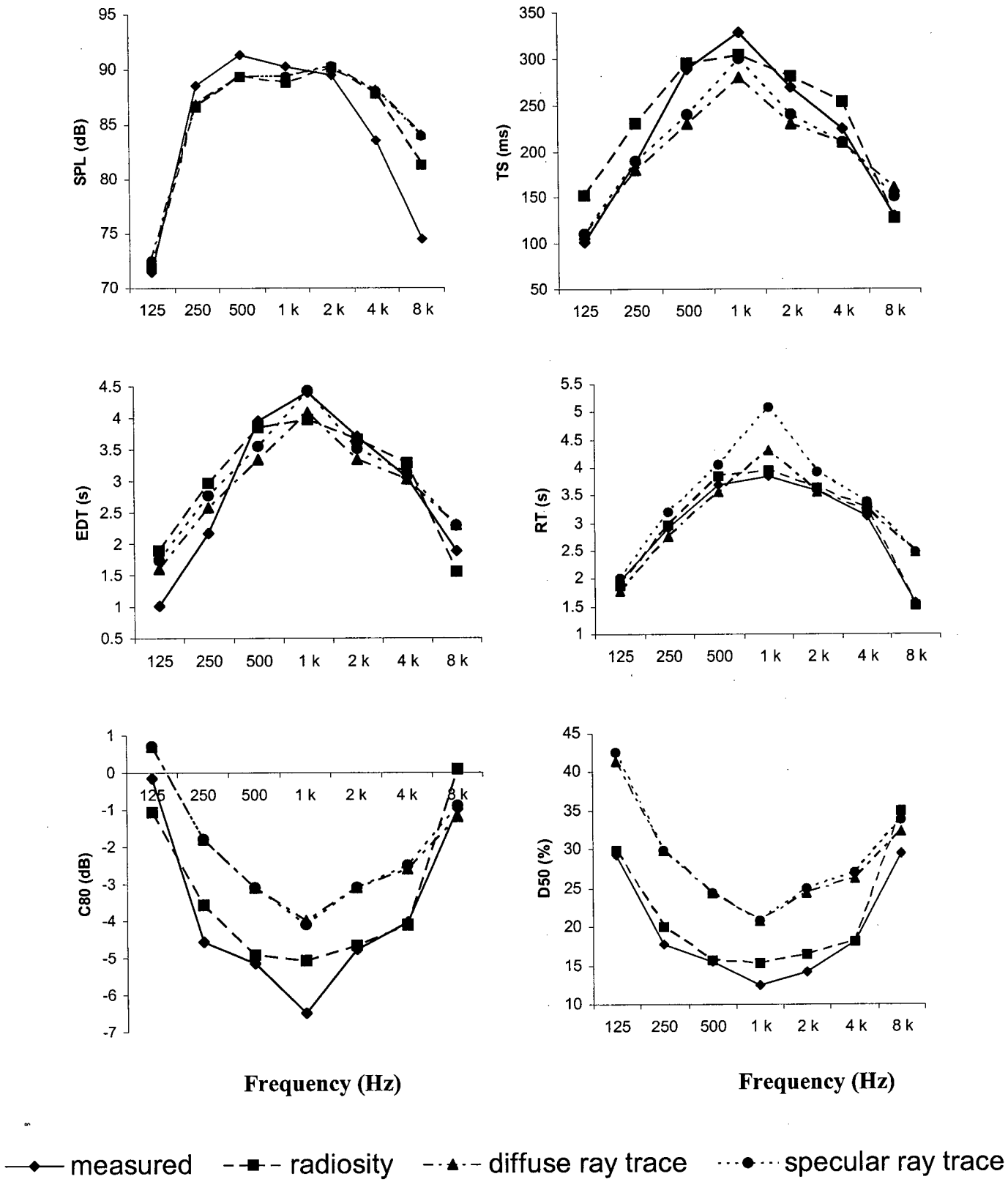

Figure 5.32. Parameter values as a function of frequency (Hz) in the Environmental Room.

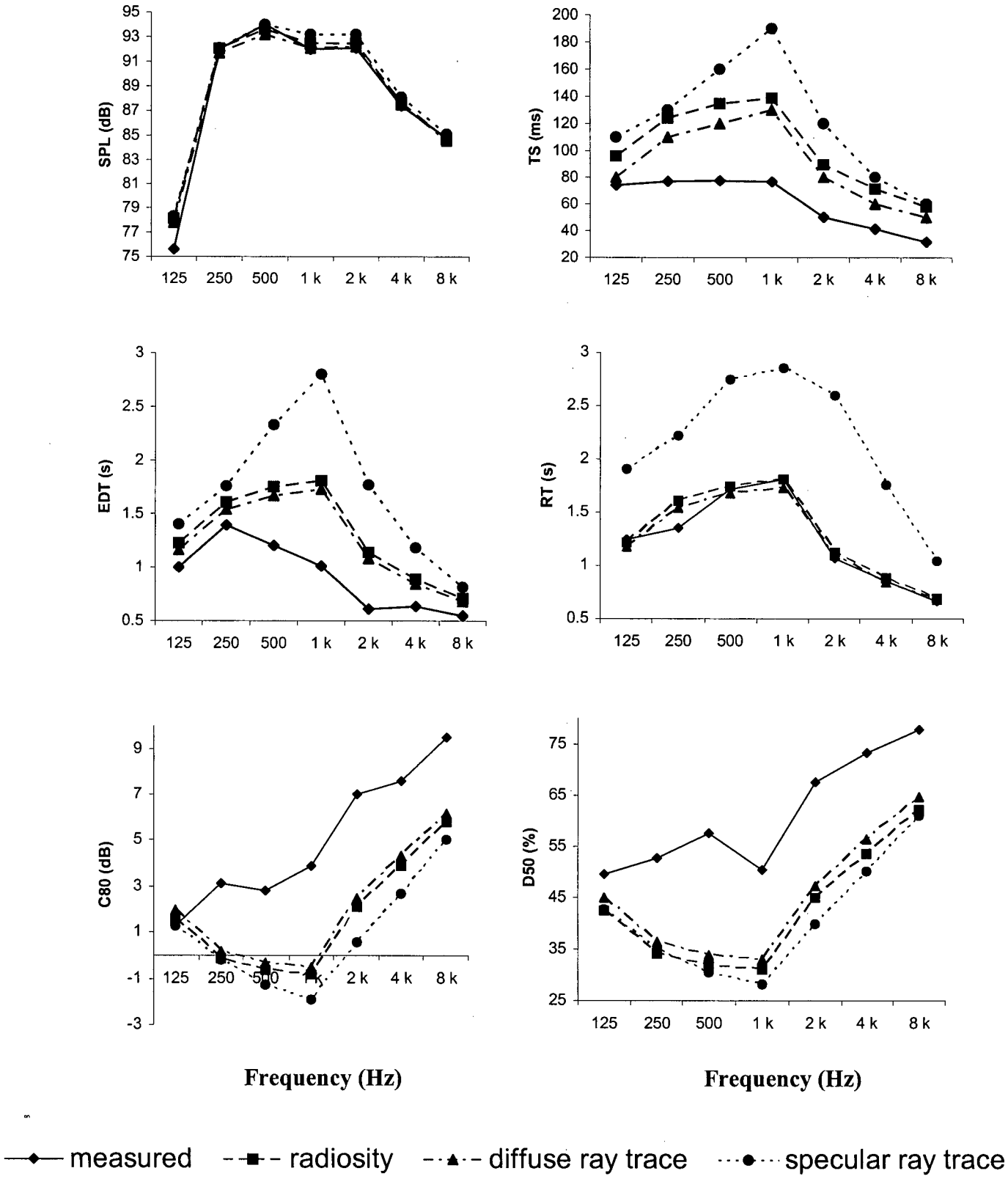

Figure 5.33. Parameter values as a function of frequency (Hz) in Hebb 12.

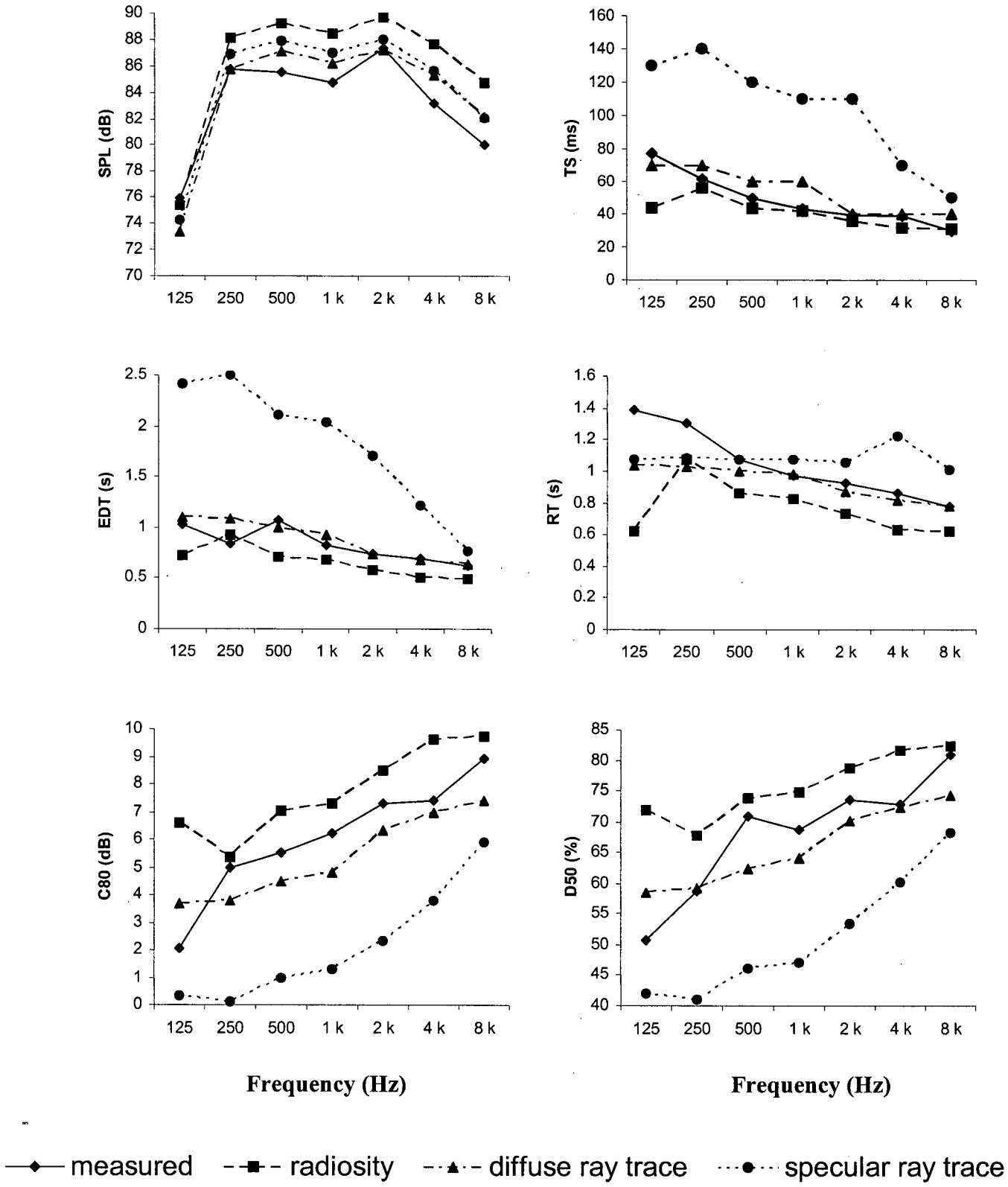

Reference back to the discretized echograms makes it clear why predicted center times, early decay times, and *RT*s are higher than measured values in the Environmental Room. The discretized echogram for this room shows significantly more energy measured than predicted in the early time steps. Also seen in the discretized echogram is more energy in the later time steps for ray tracing with specular reflection, which might explain why predictions of *TS*, *EDT*, and *RT* by this method are so much higher than by other methods or measurement. These observations also explain why predicted clarity and definition values are lower than measured for the Environmental Room. Similar, although not as obvious or convincing, observations can be made for Hebb 12.

Measured sound pressure levels were predicted much more closely (by all prediction methods) in the Environmental Room than in the squash court or in Hebb 12. Radiosity predictions of *SPL* were particularly poor in Hebb 12; radiosity predicted levels up to 3.7 dB higher than measured. As in the *SPL* predictions in the squash court from Figure 5.30, it is not immediately evident why predicted levels are so different from measured levels. Once again, approximation of absorption and its distribution may be partly responsible. This is not immediately obvious, however, since more absorption would be needed to bring the predicted *SPL*s down to measured levels. This would result in lower predicted reverberation and early decay times, which are already lower (when radiosity is used) than measured times. As we have seen from predictions in cubical rooms (in Section 5.3.1.2), absorption distribution has a significant effect on *RT*, thus it is possible that more absorption distributed differently would give more accurate predictions. Once again, calibration of the source may be another source of error.

It is interesting to note that radiosity gave very similar predictions for both *RT* and *EDT* in all rooms. The same observation applies to ray tracing with diffuse reflection. This indicates that the rate of decay in sound pressure level for diffuse reflection is constant, and, correspondingly, that decay curves are linear. This also corresponds to an exponential decay of energy associated with diffuse fields. This is not the case in real rooms, or for specular reflection, as is evident from comparison of measured *RT*s and *EDT*s and those predicted by ray tracing with specular reflection. Indeed, measured *RT*s in the squash court are lower than measured *EDT*s. This indicates slower decay near the beginning of the response and faster decay as time progresses, corresponding to a less steep decay curve at the beginning, and a steeper curve at the

end. Ray tracing with specular reflection predicted the same trend as measured in the squash court. In the Environmental Room and Hebb 12, measured *RT*s were higher than *EDT*s, so that decay cures are steeper at the start. Specular ray tracing also predicted higher *RT* than *EDT* in the Environmental room, although in Hebb 12, *EDT*s were predicted higher than *RT*s. In general, it appears that specular reflections are essential for the correct prediction of decay rate in a room, and that, in this respect, radiosity may only be applicable for later parts of the decay, when the slope of the decay curve has become more constant (equivalently, when energy decay has become exponential).

It is not clear from the data collected here that radiosity (or either of the ray tracing methods) is more accurate at higher frequencies. This observation is mentioned because it might be expected that geometrical prediction methods (such as radiosity or ray tracing) give better predictions for higher frequencies, for which modal effects are not as great.

5.5.4 Conclusions

It is evident that echogram predictions by radiosity are quite different from any measured echograms and from echograms obtained by ray tracing, even ray tracing with diffuse reflection. Overall, radiosity smears energy in time, and eliminates any strong reflections from the echogram. This may make it insufficient for realistic rendering (auralization) of sound fields, in which strong signals have considerable effect on listener perception. The discretized echograms predicted by radiosity are similar to those predicted by ray tracing, but they tend lose much of the information about the distribution of energy in a real room.

Parameter values, although not completely accurate, were reasonably well predicted by radiosity in the three rooms measured, and were often predicted closer to measurement by radiosity than by ray tracing. Ray tracing with specular reflection was particularly poor in predicting center time, early decay time, clarity, and definition in the Environmental Room and in Hebb 12, as well as reverberation time in the Environmental Room. This suggests that diffuse reflection plays a very important roll in characterizing the sound field in a room, and cannot be ignored. Because the diffuse models (radiosity and ray tracing with diffuse reflection) tended to do better than the specular model, we have evidence that an assumption of purely diffuse reflection may be less limiting than an assumption of purely specular reflection.

Radiosity performed particularly well in parameter predictions for the squash court. This is possibly due to the uniform distribution of absorption in the squash court. Uniform distribution helps in two ways. First, uniform distribution creates a more diffuse sound field, since energy is not being drawn (absorbed) out of the enclosure more strongly in any one direction. Since we expect that diffuse reflection, as assumed by radiosity, also results in a more diffuse sound field, radiosity might be expected to perform better in an enclosure with a diffuse sound field and, consequently, in an enclosure with uniform absorption. Secondly, with uniform distribution of absorption, the question of how to distribute absorption is not pertinent; error is not as likely to be introduced because of an inaccurate estimation of the distribution of absorption. As we have seen in Section 5.3.1.2, the distribution has a significant effect on parameters such as reverberation time, and this may explain some of the problems with predictions in the Environmental Room and in Hebb 12.

In general, radiosity is poor at capturing information about the prominent reflections of a sound field, but it can predict the overall energy distribution, particularly in the late part of the decay in which individual reflections are not as prominent, with reasonable accuracy. As with any prediction method, it is often difficult to accurately estimate the physical properties of the system for input into the model.

CHAPTER 6

Conclusion

The objective of this research was to develop a radiosity algorithm for the prediction of sound fields in rooms, to validate it experimentally, and to use this algorithm to gain insight into the applicability and validity of acoustical radiosity in room acoustics. To accomplish this, research was done in several stages.

The first stage was to review literature on radiosity in acoustics, as well as in other fields such as illumination engineering and computer graphics. Literature from other fields was found to be highly comprehensive and developed, but could not be directly applied to acoustics because of the time-independent nature of radiosity in these fields. Research in acoustical radiosity, although begun by Kuttruff in the 1970's, has not been nearly as intense as in the other fields. One possible reason for this lack of research is the seemingly limited application of acoustical radiosity, due to the assumption of diffuse reflection, which is more restrictive at the lower frequencies of sound than it is for light. Also, the time dependence of radiosity in acoustics makes it prohibitively computationally intensive, at least at initial glance. Nevertheless, diffuse reflection may be a less restrictive assumption than specular reflection. Also, the view-independent nature of acoustical radiosity (whereby after one lengthy rendering for a given source position, predictions for varying receiver positions are very fast) makes it a promising model. Further, recent developments in time-dependent radiosity have indicated that it is possible to incorporate specular reflection into acoustical radiosity, and that methods can be (and are being) developed that increase the computational efficiency of acoustical radiosity.

Because a thorough, comprehensive development of acoustical radiosity could not be found in the literature, one was developed and presented in this thesis. It begins with an overview of the assumptions of radiosity, goes through the derivation of the integral equation, and gives

the details of the numerical solution. In the development of the numerical solution, both the enclosure and time are discretized. Enclosure discretization leads to the evaluation of form factors, for which two methods are presented and implemented. The first is an analytical method based on formulas from radiation heat transfer for rectangular rooms discretized by rectangular patches. The second, implemented for use with non-rectangular rooms and non-rectangular patches, uses *Helios FF* (a modified commercial graphics radiosity renderer that uses two-level hierarchy and the cubic tetrahedral method to estimate form factors). The author was not aware of non-rectangular patches having been used elsewhere in literature on acoustical radiosity. If they were, it was not indicated how the integrals over solid angles that arise were evaluated. To evaluate these integrals, a method, given the name 'spherical triangle method', was developed and implemented. An approximation of late radiation densities by an averaging technique was suggested and implemented for the numerical solution. An algorithm, the outline of which is given in the thesis, was developed (in *MATLAB*) to implement the numerical solution. From this solution, methods for finding impulse responses, echograms, and room acoustical parameters were discussed.

The numerical solution to the integral equation and the algorithm were validated by comparison of predictions for a spherical enclosure to analytical solutions for the sphere. Before further predictions were made, a method for analyzing and interpreting echograms called 'echogram discretization' was proposed. Further, theoretical investigation into the effect of predicted impulse response lengths on reverberation time resulted in a criteria for determining the minimum time to which predictions must be made. Predictions then were made for four cubical enclosures using radiosity and ray tracing. From these predictions, it was suggested that 150 patches, discretization periods of 1/4000 s, and impulse responses predicted exactly for slightly over half of the total predicted length of the response (determined from the criteria developed earlier) were sufficient for accurate prediction in these enclosures. Observations about the differences between ray tracing and radiosity, the effects of absorption distribution, the computational requirements of radiosity, and the validity of using *Helios FF* for form factor approximation were also made based on the predictions in the cubical enclosures. Predictions were made by radiosity for three real rooms, and were compared to measurements and to ray tracing predictions made in the same rooms. Echogram comparisons revealed significant differences between measurement and prediction methods, the most striking (although

understandable) of which is the lack of strong reflections in the radiosity echogram. Several suggestions about the applicability and validity of radiosity as a room sound field prediction method were discussed.

The question of the accurate estimation and distribution of absorption in the three measured rooms was raised several times. Certainly, it would be beneficial to be able to compare predictions to measurements made in rooms for which absorption coefficients are known. Further research might attempt to reduce uncertainties about the absorption through the use of in-situ absorption measurements, or by measurements in models built from materials whose absorption coefficients are pre-determined in an anechoic chamber. It would also be very interesting to auralize sound fields predicted by radiosity and compare them to real sound fields or sound fields created by other prediction methods. Similar experiments and analysis to those done in this thesis could be performed in other rooms - particularly non-rectangular rooms - to gain further insights into acoustical radiosity. Other future work might include the validation of hybrid prediction models that use radiosity to predict the late part of the room response, and some other method (which incorporates specular reflection) to predict the early part of the room response. Incorporation of specular reflection directly into radiosity is another approach that warrants research, as do methods for increasing the efficiency of acoustical radiosity.

In summary, an acoustical radiosity method for predicting sound fields in rooms was developed and implemented, for which several new approaches were suggested and used. Validation of the numerical approximations was successful, and the sound fields of several enclosures were predicted. Some insight into acoustical radiosity was gleaned from these predictions by comparison to other prediction methods and to measurement.

BIBLIOGRAPHY

[1] Alarcão, D., and Bento Coelho, J.L. "Fast acoustical modeling of enclosures with diffusely reflecting surfaces," *Proceedings of the Forum Acusticum Sevilla in Seville, Spain, September 16-20, 2002*, by the Spanish Acoustical Society.

[2] Ashdown, I. *Radiosity: A programmer's perspective*, New York: John Wiley & Sons, 1994.

[3] Asvestas, John S., and Englund, David C. "Computing the solid angle subtended by a planar figure", *Optical Engineering* 33(12): 4055-4056, Dec. 1994.

[4] Baines, N.C., *An investigation of the factors which control non-diffuse sound fields in rooms*, PhD thesis, University of Southampton, 1983.

[5] Bass, H.E., Sutherland, L.C., Zuckerwar, A.J., Blackstock, D.T., and Hester, D.M. "Atmospheric absorption of sound: Further developments," *Journal of the Acoustical Society of America* 97(1): 680-683, Jan. 1995.

[6] Beran-Koehn, J., and Pavicic, M.J. "A cubic tetrahedral adaptation of the hemi-cube algorithm," *Graphics Gems II*, ed. James Arvo, (Boston: Academic Press), 299-302, 1991.

[7] Beran-Koehn, J., and Pavicic, M.J. "Delta form-factor calculation for the cubic tetrahedral algorithm," *Graphic Gems III*, (Boston: Academic Press), ed. David Kirk, 324-328, 1992.

[8] Beranek, L.L., *Concert and opera halls – How they sound*, Acoustical Society of America, 1996.

[9] Chekhovskii, I.R., Sirotkin, V.V., Chu-Dun-Chu, Y.V., and Chebanov, V.A. "Determination of radiative view factors for rectangles of different sizes," *High Temperature* 17(1): 97-100, Jan.-Feb. 1979.

[10] Carroll, M.M., and Chien, C.F. "Decay of reverberant sound in a spherical enclosure," *Journal of the Acoustical Society of America* 62(6): 1442–1446, Dec. 1977.

[11] Carroll, M.M., and Miles, R.N. "Steady-state sound in an enclosure with diffusely reflecting boundary," *Journal of the Acoustical Society of America* 64(5): 1424-1428, Nov.1978.

[12] Cohen, M.F., and Wallace, J.R. *Radiosity and realistic image synthesis*, Boston: Academic Press, Inc., 1993.

[13] Cremer, L., and Müller, H.A. *Principles and applications of room acoustics*. Translated by Theodore Schultz. London: Applied Science Publishers, 1982.

[14] Etgen, Garret J. *Salas and Hille's Calculus – Several Variables*, 7th ed. New York: John Wiley & Sons, 1995.

[15] Foley, J., Van Dam, S., Feiner, S., and Hughes, J. *Computer graphics: Principles and practices*, 2nd ed. Boston: Addison-Wesley Publishing Company Inc., 1990.

[16] Franzoni, L.P., Bliss, D.B., and Rouse, J.W. "An acoustic boundary element method based on energy and intensity variables for prediction of high-frequency broadband sound fields," *Journal of the Acoustical Society of America* 110 (6): 3071-3080, Dec. 2001.

[17] Franzoni, L.P., and Rouse, J.W. "An intensity-based boundary element method for analyzing broadband high frequency sound fields in enclosures," *Proceedings of the Forum Acusticum Sevilla in Seville, Spain, September 16-20, 2002*, by the Spanish Acoustical Society.

[18] Gilbert, E.N. "An iterative calculation of reverberation time," *Journal of the Acoustical Society of America* 69(1): 178-184, Jan. 1981.

[19] Gross, U., Spindler, K., and Hahne, E. "Shape-factor equations for radiation heat transfer between plane rectangular surfaces of arbitrary position and size with rectangular surfaces of arbitrary position and size with rectangular boundaries," *Letters in heat mass transfer* 8: 219-227, 1981.

[20] *Helios32* is a registered trademark of *byHeart Consultants Limited*. See www.helios32.com.

[21] Hodgson, M. "Measurements of the influence of fittings and roof pitch on the sound field in panel-roof factories," *Applied Acoustics* 16(5): 369-391, 1983.

[22] Hodgson, M. "Evidence of diffuse surface reflections in rooms," *Journal of the Acoustical Society of America* 89(2): 756-771, 1991.

[23] Hodgson, M. "When is diffuse-field theory applicable," *Applied Acoustics* 49(3): 197-207, 1996.

[24] Howell, J.R., *A catalog of radiation configuration factors*, New York: McGraw-Hill, 1982. Available online at: www.me.utexas.edu/~howell/tablecon.html.

[25] Hsu Chia-Jung. "Shape factor equations for radiant heat transfer between two arbitrary sizes of rectangular planes," *Canadian Journal of Chemical Engineering* 45(1): 58-60, Feb. 1967.

[26] International Organization for Standardization. *Acoustics – Measurement of the reverberation time of rooms with reference to other acoustical parameters*, ISO 3382: 1995(E).

[27] Joyce, W.B. "Sabine's reverberation time and ergodic auditoriums," *Journal of the Acoustical Society of America* 58(3): 643-655, Sept. 1975.

[28] Joyce, W.B. "Exact effect of surface roughness on the reverberation time of a uniformly absorbing spherical enclosure," *Journal of the Acoustical Society of America* 64(5): 1429-1436, Nov. 1978.

[29] Kang, J. "Reverberation in rectangular long enclosures with diffusely reflecting boundaries," *Acta Acustica united with Acustica* 88: 77-87, 2002.

[30] Kuttruff, H. "Simulierte Nachhallkurven in Rechteckräumen mit diffusem Schallfeld," [Simulated reverberation curves in rectangular rooms with diffuse sound fields], *Acustica* 25(6): 333-342, 1971.

[31] Kuttruff, H. "Nachhall nud effective Absorption in Räumen mit diffuser Wanderflexion," [Reverberation and effective absorption in rooms with diffuse wall reflections], *Acustica* 35(3): 141-153, 1976.

[32] Kuttruff, H. "Stationäre Schallausbreitung in Flachräumen," [Stationary sound propagation in flat enclosures], *Acustica* 57, 62-70, (1985).

[33] Kuttruff, H. "Iterative Bestimmung des Schallabsorptionsgrads aus der gemessenen Nachhallzeit beim Hallraumverfahren," [Iterative determination of the sound absorption coefficient from the measured reverberation time in the reverberation room method], *Acustica* 81: 433-438, 1995.

[34] Kuttruff, H. "A simple iteration scheme for the computation of decay constants in enclosures with diffusely reflecting boundaries," *Journal of the Acoustical Society of America* 98(1): 288-293, July 1995.

[35] Kuttruff, H. "Energetic sound propagation in rooms," *Acta Acustica united with Acustica*, 83: 622-628, 1997.

[36] Kuttruff, H. *Room Acoustics*, 4th ed. London: Spon Press, 2000.

[37] Kuttruff, H. "Stationary propagation of sound energy in flat enclosures with partially diffuse surface reflection," *Acta Acustica united with Acustica* (86): 1028 – 1033, 2000.

[38] Kuttruff, H., and Strassen, T. "Zur Abhängigkeit des Raumnachhalls von der Wanddiffusität und von der Raumform," [On the dependence of reverberation time on the "wall diffusion" and on room shape], *Acustica* 45: 246-255, 1980.

[39] LeBot, A. "A functional equation for the specular reflection of rays," *Journal of the Acoustical Society of America* 112 (4): 12761287, Oct. 2002.

[40] LeBot, A., Bocquillet, A. "Comparison of an integral equation on energy and the ray-tracing technique in room acoustics," *Journal of the Acoustical Society of America* 108 (4): 1732-1740, Oct. 2000.

[41] Lewers, T. "A combined beam tracing and radiant exchange computer model of room acoustics," *Applied Acoustics* 38: 161-178, 1993.

[42] Li, J.-F., and Hodgson, M. "In situ experimental determination of surface impedance at oblique incidence using pseudo-random sequences and a single microphone," *Journal of the Acoustical Society of America* 102(4): 2200-2210, 1997.

[43] Lighthill, M.J. *Introduction to Fourier analysis and generalized functions*, London: Cambridge University Press, 1958.

[44] *MATLAB* is a registered trademark of The Math Works, Inc.

[45] Miles, R.N., "Sound field in a rectangular enclosure with diffusely reflecting boundaries," *Journal of Sound and Vibration* 92(2): 203 – 226, 1984.

[46] DRA Laboratories. *MLSSA – Maximum Length Sequence System Analyzer & reference manual version 8.0*, 1987-1992.

[47] Ondet, A.M., and Barbry, J.L. "Modeling of sound propagation in fitted workshops using ray-tracing," *Journal of the Acoustical Society of America* 85(2): 29-46, 1987.

[48] Rathe, E.J., "Note on two common problems of sound propagation," *Journal of Sound and Vibration* 10(3): 472-479 (1969).

[49] Ressel, V. *Room sound field prediction for auralization*, Master's thesis, University of British Columbia, 1997.

[50] Reynolds, D.D. *Engineering principles of acoustics: Noise and vibration control*, Boston, Allyn and Bacon, 1981.

[51] Rindel, J.H. "Modeling in auditorium acoustics – from ripple tank and scale models to computer simulations," *Keynote Lecture, Proceedings of the Forum Acusticum Sevilla in Seville, Spain, September 16-20, 2002*, by the Spanish Acoustical Society.

[52] Rougeron, G., Gaudaire, F., Gabillet, Y., Bouatouch, K. "Simulation of the indoor propagation of a 60 GHz electromagnetic wave with a time-dependent radiosity algorithm," *Computers & Graphics* 26: 125-141, 2002.

[53] Rushmeier, H. *Extending the radiosity method to transmitting and specularly reflecting surfaces*, Master's thesis, Cornell University, 1986.

[54] Schroeder, M.R., and Hackman, D. "Iterative calculation of reverberation time," *Acustica* 45: 269-273, 1980.

[55] Schroeder, M.R., and Kuttruff, H. "On frequency response curves in rooms," *Journal of the Acoustical Society of America* 34(1): 76-80 1962.

[56] Shi, J., Zhang, A., Encarnação, J., and Göbel M. "A modified radiosity algorithm for integrated visual and auditory rendering," *Computers & Graphics* 17 (6): 633-642, 1993.

[57] Siegel, R., and Howell, J. *Thermal radiation heat transfer*, 3rd ed. Washington, DC: Hemisphere Publishing Corporation, 1981.

[58] Sillion, F.X., Arvo, J.R., Westin, S.H., and Greenberg, D.P. "A global illumination solution for general reflectance distributions," *Computer Graphics* 25(4): 187-196, 1991.

[59] Sillion, F., and Puech, C. "A general two-pass method integrating specular and diffuse reflection," *Computer Graphics* 23(3): 335-344, 1989.

[60] Sillion, F.X., and Puech, C. *Radiosity and global illumination*, San Fransisco: Morgan Kaufmann, 1994.

[61] Sotiropoulou, A.G., and Fleming, D.B. "Concert hall acoustic evaluations by ordinary concert-goers. II. Physical room acoustics criteria subjectively significant," *Acustica* 81(1): 10-19, 1995.

[62] Sparrow E., and Cess, R. *Radiation heat transfer*, Washington, DC: Hemisphere Publishing Corporation, 1978.

[63] Tsingos, N. *Simulation de champs sonores de haute qualite pour des applications graphiques interactives*, [Simulating high quality dynamic virtual sound fields for interactive graphics applications], Ph.D. thesis, Universite Joseph Fourier-Grenoble 1, 1998. Download at www-sop.inria.fr/reves/personnel/Nicolas.Tsingos/.

[64] Weeks, J.R. *The shape of space*, 2nd ed. New York: Marcel Dekker Inc., 2002.

[65] Yamauti, Z. "The light flux distribution of a system of interreflecting surfaces," *Journal of the Optical Society of America* 13(5): 561-571, 1926.

APPENDIX A

Definitions

Absorption coefficient (α). The property of a surface that gives the fraction of energy incident on the surface that is absorbed by the surface.

Air absorption coefficient/exponent. The property of a medium that gives the propagation loss in sound energy traveling through the medium. Two forms are used in the literature (see Appendix B for a relationship between the two):

Air absorption coefficient (α_m). The amount that the sound pressure level of a plane wave decreases per meter of propagation:

$$L_p(x) = L_p(0) - \alpha_m x \tag{A.1}$$

where $L_p(x)$ is the sound pressure level at a distance of x meters in the direction of propagation from $x = 0$. Units: dB/m. Strictly speaking, α_m is not really a coefficient, but a constant.

Air absorption exponent (m). The intensity of a plane wave decreases according to:

$$I(x) = I(0)\,\mathrm{e}^{-mx} \tag{A.2}$$

where $I(x)$ is the intensity at a distance of x meters in the direction of propagation from $x = 0$. Units: m^{-1}.

Anechoic Chamber. A room with sound absorbers mounted on the walls, floor, and ceiling so that (almost) no reflections are produced by the boundaries above some cutoff frequency. The sound field in an anechoic chamber simulates free-field conditions.

Average absorption coefficient ($\bar{\alpha}$). If a surface consists of several homogeneous sub-surfaces, then the average absorption coefficient is defined as:

$$\bar{\alpha} = \sum_{i=1}^{n} \alpha_i S_i \Big/ \sum_{i=1}^{n} S_i \tag{A.3}$$

where α_i and S_i are the absorption coefficient and surface area of surface i, respectively, and there are n surfaces.

Center Time (*TS*). A room acoustical parameter defined as the first moment of the pressure-squared impulse response, $g(t)$,

$$TS = \frac{\int_0^\infty t g(t) dt}{\int_0^\infty g(t) dt}. \tag{A.4}$$

Clarity Index (C_n). A room acoustical parameter defined as

$$C_n = 10 \log \left(\frac{\int_0^{n\,\mathrm{ms}} g(t) dt}{\int_{n\,\mathrm{ms}}^\infty g(t) dt} \right) dB \tag{A.5}$$

where n is time in milliseconds and $g(t)$ is the pressure-squared impulse response. The most commonly used clarity index is C_{80}, which is used in this thesis. See Appendix B for the derivation of a relationship between clarity and definition.

Decay curve. The decay of the sound pressure level as a function of time, with $t = 0$ the time of cessation of a continuous sound.

Decay time (*T*). A measure of the rate of decay of reverberant sound in an enclosure [28]. If T exists and has finite value greater than zero, then the decay time, T, is defined as

$$1/T = \lim_{t \to \infty} (N^{-1} dN/dt) \tag{A.6}$$

where $N(t)$ is the total sound energy at time t with $t = 0$ the time of cessation of sound generation. For a perfectly absorbing surface ($\alpha = 1$), both N and dN/dt are identically zero after a finite time, so T is undefined by the equation above. In this case, we define the decay time as

$$T(\alpha = 1) = \lim_{\alpha \to 1} T(\alpha). \tag{A.7}$$

Decibel averaging. For n levels L_i, $i = 1, 2, \ldots, n$, the decibel average level, $\overline{L}$ is given by

$$\overline{L} = 10\log\left[\frac{1}{n}\sum_{i=1}^{n} 10^{L_i/10}\right]. \tag{A.8}$$

Definition (D_n). A room acoustical parameter defined as the ratio (in percent) of the early to total sound energy

$$D_n = \frac{\int_0^{n\,\mathrm{ms}} g(t)dt}{\int_0^{\infty} g(t)dt}\% \tag{A.9}$$

where n is time in milliseconds and $g(t)$ is the pressure-squared impulse response. See Appendix B for the derivation of a relationship between clarity and definition.

Diffuse sound field. A field in which energy is distributed equally in all positions and flows equally in all directions; it is an isotropic, homogeneous distribution of energy. Such a field would result in vanishing net energy flow and is therefore incompatible with any wall absorption, which causes the flow of some energy towards the wall. The assumption of a diffuse field has been established as having limited applicability [23]. Nevertheless, such an assumption affords great simplifications in the predictions of room acoustics, which has made it very popular among practitioners and room acousticians (particularly the Sabine and Eyring formulas).

Diffuse reflection. Reflection according to Lambert's law (see Section 2.2.1). A surface adhering to Lambert's law is called a Lambertian or diffusely reflecting surface.

Dirac delta function ($\delta(t)$). A generalized function defined by two properties. First,

$$\int_{-\infty}^{\infty} \delta(t) = 1.$$

Second, $\delta(t) = 0$ for all $t \neq 0$.

These two properties give

$$\int_{-\infty}^{\infty} s(\tau)\delta(t-\tau)d\tau = s(t) \tag{A.10}$$

for any continuous function of time, $s(t)$. $\delta(t)$ is often considered as being infinite for $t = 0$ and zero for $t \neq 0$. Refer to a text on mathematical physics or Fourier analysis for details [43].

Directivity function (Q). A characteristic of the directional distribution of the intensity of a sound source. $Q(\theta,\xi)$ is the ratio of the energy radiated in the direction θ, in the horizontal plane, and ξ, in the vertical plane, to the average energy radiated over all angles.

Double Lune. Region on a sphere bounded by two great circles. See Figure A.1.

Early Decay Time (*EDT*). A room acoustical parameter defined as six times the time it takes for the energy to reach one tenth of its initial value after the cessation of sound (equivalently, for the sound pressure level to fall 10 dB).

Echogram. A diagram of the pressure squared response $s(t)$ of a room at a receiver position for a given signal. The echogram is made by making a vertical mark of magnitude $s(t)$ at time t (for all times for which $s(t) \neq 0$).

Energy Density. A characterization of the amount of energy contained in one unit volume of a sound field.

Eyring's Formula. A (famous) formula for reverberation time, *RT*, in a room based on the assumption of a diffuse sound field and incoherent phase relationships[36]:

$$RT = \frac{24V\ln(10)}{c(4mV - S\ln(1-\overline{\alpha}))} \approx 0.161\frac{V}{4mV - S\ln(1-\overline{\alpha})} \tag{A.11}$$

Though it is based on the highly questionable assumption of a diffuse sound field, Eyring's formula (along with the similar and equally important Sabine formula) has been widely used by room acousticians for its simplicity.

Figure A.1. Double lune with angle α.

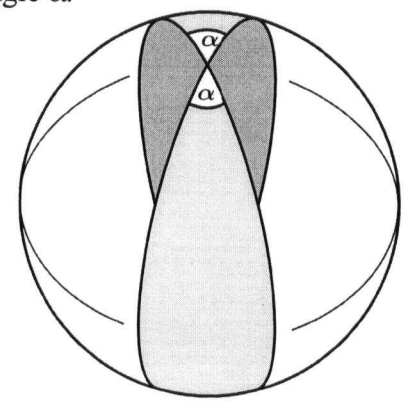

Exponential decay. A common and often accurate assumption that energy in a room decays according to [36]

$$E(t) = E(0)e^{-t/T} \tag{A.12}$$

where T is the decay time and $E(t)$ is the total sound energy in the room at time t.

Free Field. A field with no boundaries; energy propagates without interaction (reflection, transmission, or absorption) with any obstacles. A free field may be simulated in an anechoic chamber.

Great Circle. A circle on a sphere that is as big as possible. See Figure A.2.

Impulse response ($g(t)$). The output signal $g(t)$ at the receiver position in response to an impulsive sound signal represented by a Dirac Delta function. With respect to an input signal $s'(t)$, the output signal $s(t)$ is the convolution of s' and g - i.e.

$$s(t) = \int_{-\infty}^{\infty} g(\tau)s'(t-\tau)d\tau\,. \tag{A.13}$$

In this research, we are concerned with the 'pressure-squared' impulse response which gives the pressure-squared response at the receiver when convolved with the input signal (see Section 4.1.1).

Inter aural cross correlation coefficient ($IACC$). A room acoustical parameter that is a binaural measure of the difference in sound pressure at the two ears.

Intensity (I). Energy passing through a unit of area (projected normal to the direction of flow) per second. Units: W/m^2.

Figure A.2. Great circle and spherical triangle on a sphere.

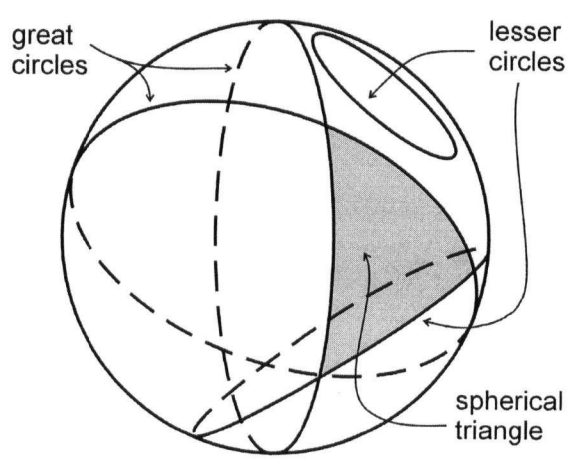

Irradiation density. The rate at which energy is incident on a unit area of surface. Units: W/m^2.

Lateral energy fraction (*LF*). A room acoustical parameter defined as the ratio of the pressure-squared output of a figure-8 microphone (with null directed at source) to the output of a non-directional microphone. The figure-8 microphone weights the energy by $\cos^2(\theta)$, where $\theta = 90^\circ$ is the direction of the sound.

Omni-directional source. A sound source that radiates equal intensity in all directions. It has directivity of one ($Q(\theta,\xi)=1$) in all directions.

Order. $f(n)$ of order $g(n)$ means that there are positive constants c and k such that $0 \le f(n) \le cg(n)$ for all $n \ge k$.

Plane wave. A wave with planar wave front; the direction of propagation is along a single axis.

Point source. Radiates energy as if from a vanishingly small source in space. The resulting waves are spherical.

Power (*W*). A measure of the rate of radiation of sound energy. Power is equal to

$$W = IA \tag{A.14}$$

where A is area in m^2 and I is the intensity. Units: W (watts).

Radiation density (*B*). The rate at which energy leaves a unit area of surface (W/m^2).

Reference power (W_0). Standardized reference power with a value of 10^{-12} W.

Reference pressure (p_0). Standardized reference pressure roughly corresponding to the normal human threshold of hearing at 1000 Hz. It has a value of 2×10^{-5} Pa.

Reflection coefficient (ρ). The property of a surface that gives the fraction of energy incident on the surface that is reflected.

Reverberation time (*RT*). A room acoustical parameter defined as the time it takes for the energy to reach one millionth of its initial value after the cessation of sound (equivalently, for the sound pressure level to fall 60 dB). Refer to Appendix B for reverberation time as a function of decay time.

Root mean square pressure (p_{rms}). The characterization of a stationary signal as the root of the time average of pressure squared over sufficient time

$$p_{rms} = \left(\frac{1}{t_0} \int_0^{t_0} p^2(t)dt \right)^{1/2} Pa. \tag{A.15}$$

Sabine's formula. See definition for Eyring's formula, and substitute the low-absorption approximation $-\ln(1-\overline{\alpha}) \cong \overline{\alpha}$ in Eq. (A.11).

Sound Power Level (*PL*). The characterization of a signal given by

$$PL = 10\log\left(\frac{W}{W_0}\right) dB \tag{A.16}$$

where W_0 is the reference power and W is the power of the signal.

Sound Pressure Level (*SPL*). Used as the characterization of a stationary signal at a receiver position instead of intensity or root mean square pressure, which has too much variance in magnitude for the human threshold of hearing to be of practical use. It is a function of root mean square pressure

$$SPL = 20\log\left(\frac{p_{rms}}{p_0}\right) dB \tag{A.17}$$

where p_0 is the reference pressure.

Specular reflection. Reflection from a surface in a single direction. It follows two laws: (1) the incident ray, the reflected ray, and the perpendicular to the mirror at the point of incidence lie in the same plane; and (2) the angle of incidence (between the incident ray and the surface normal) is equal to the angle of reflection (between the reflected ray and surface normal).

Spherical Polygon. A polygon drawn on a sphere. Each side must be a geodesic; it must be the shortest path along the sphere between its two vertices. Each side is thus the arc of a great circle. A spherical triangle is just a spherical polygon with three edges (see Figure A.2). The angle on a sphere between two straight (geodesic) lines is defined as the angle between the planes passing through the great circles formed by extending the lines (alternately, the planes passing through two points on each line and the center of the sphere).

Spherical waves. Waves with wave fronts that are concentric spheres.

Strength (*G*). A room acoustical parameters defined as the difference between the steady state sound pressure level in the room at the receiver position and the steady state sound pressure level in an anechoic room at 10 m from the source. In both cases, the same omni-directional sound source is used. In equations,

$$G = 10\log\left(\frac{\int_0^\infty g(t)dt}{\int_0^\infty g_A(t)dt}\right) \tag{A.18}$$

where $g(t)$ is the pressure-squared impulse response and $g_A(t)$ is the pressure-squared impulse response in an anechoic chamber at 10 m from the source.

Transmission coefficient (τ). The property of a surface that gives the fraction of total energy incident on the surface that is transmitted through the surface.

APPENDIX B

Relationships

The relationships between some values are derived in this Appendix.

B.1 Reverberation and decay time

To find reverberation time, RT, as a function of decay time, T, assume exponential decay according to Eq. (A.12). This gives

$$E(RT) = E(0)e^{-RT/T}$$

We want

$$E(RT) = 10^{-6}E(0)$$

$$\Rightarrow \quad 10^6 = e^{RT/T}$$

$$\Rightarrow \quad \ln(10^6) = \frac{RT}{T}$$

$$\Rightarrow \quad RT = 6T\ln(10) \approx 13.82T \tag{B.1}$$

B.2 Clarity and definition

To find a simple relationship between clarity and definition, let $E = \int_0^{n\,\mathrm{ms}} g(t)dt$, $L = \int_{n\,\mathrm{ms}}^{\infty} g(t)dt$, and $T = \int_0^{\infty} g(t)dt$ (where E, L, and T stand for early, late, and total, respectively).

Then

$$T = E + L \tag{B.2}$$

By the definitions of clarity, C_n, and definition, D_n, we have

$$C_n = 10\log(E/L) \quad \text{and} \quad D_n = E/T$$

$$\Rightarrow \quad E = L10^{C_n/10} \quad \text{and} \quad E = D_n T$$

so, by Eq. (B.2),

$$L10^{C_n/10} = D_n(E+L)$$

$$\Rightarrow \quad L\left(10^{C_n/10} - D_n\right) = D_n E$$

$$\Rightarrow \quad \frac{E}{L} = \frac{10^{C_n/10} - D_n}{D_n}$$

$$\Rightarrow \quad 10^{C_n/10} = \frac{10^{C_n/10} - D_n}{D_n}$$

$$\Rightarrow \quad C_n = 10\log\left(\frac{D_n}{1-D_n}\right) \quad \text{and} \quad D_n = \frac{10^{C_n/10}}{10^{C_n/10}+1} \tag{B.3}$$

B.3 Absorption, transmission, and reflection coefficients

If ρ is the reflection coefficient, α is the absorption coefficient, and τ is the transmission coefficient, then

$$\rho + \alpha + \tau = 1 \tag{B.4}$$

B.4 Air absorption coefficients and exponents

To find a relationship between the air absorption coefficient, α_m, and the air absorption exponent, m, of a medium, recall (Eq. (A.2)) that

$$I(x) = I(0)e^{-mx}$$

hence, by Eq. (2.14) $\quad p^2(x) = p^2(0)e^{-mx}$.

Taking logs and multiplying by 10 gives

$$L_p(x) = L_p(0) + 10\log(e^{-mx}) = L_p(0) - \left[10m\log(e)\right]x$$

so, by definition of air absorption coefficient,

$$\alpha_m = 10m\log(e) \tag{B.5}$$

APPENDIX C

Theorems

C.1 Girard's Theorem

The solid area of a spherical triangle with angles $\alpha, \beta,$ and θ (measured in radians) is

$$A = a^2(\alpha + \beta + \theta - \pi) \tag{C.1}$$

where a is the radius of the sphere.

This theorem first appeared in 1629 in the book "Invention nouvelle en l'Algebre" by Albert Girard. A proof, based on an outline and figures given by Weeks in [64] is as follows.

Proof

Let A_l be the area of the double lune (see definitions) with angle α on a sphere of radius a. For $\alpha = \pi$, the double lune fills the entire sphere, so $A_l = 4\pi a^2$. Keeping the ratio of α to A_l constant, the double lune with arbitrary angle α must fill α / π of the surface area of the sphere - i.e.

$$A_l = \frac{\alpha}{\pi} 4\pi a^2 = 4\alpha r^2. \tag{C.2}$$

For the spherical triangle with angles $\alpha, \beta,$ and θ, we extend the edges of the triangle around the sphere to form three great circles (see Figure C.1). Each pair of great circles gives a double lune. There are three such pairs, each with angles $\alpha, \beta,$ and θ (see Figure C.2). By Eq. (C.2), these double lunes have respective areas $4\alpha a^2, 4\beta a^2,$ and $4\theta a^2$.

If all three double lunes are filled in simultaneously, the whole sphere is covered at least once, with the original and antipodal spherical triangles filled three times (see Figure C.3).

Figure C.1. Extending the edges of a spherical triangle to form 3 great circles.

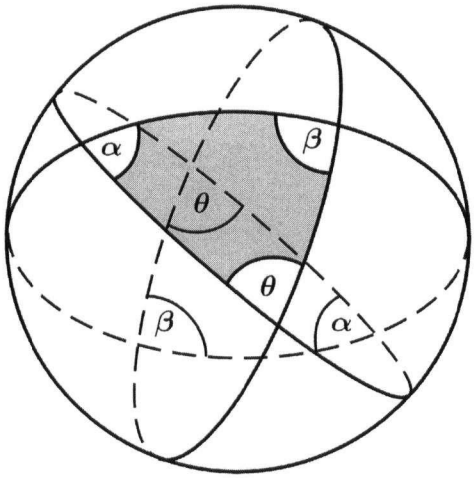

Figure C.2. Three double lunes defined by a spherical triangle.

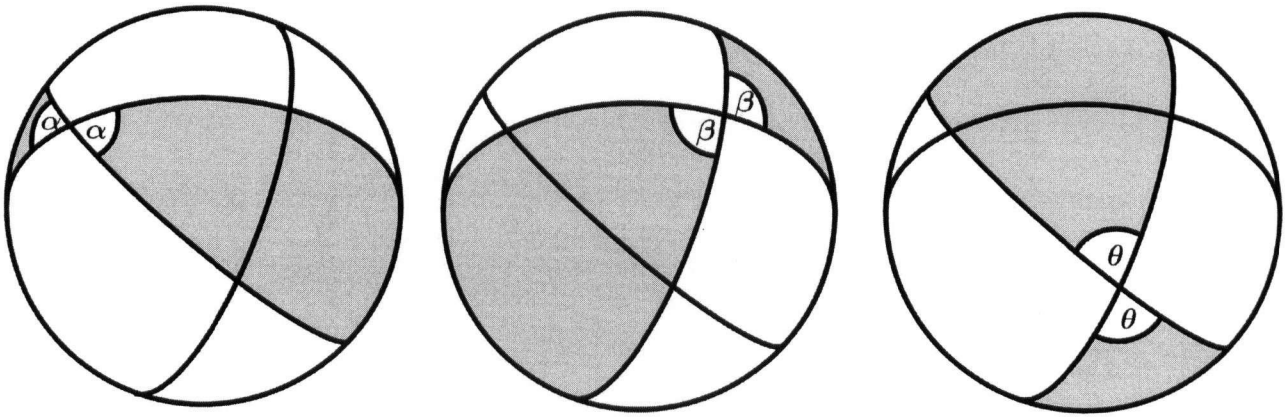

Figure C.3. Covering the sphere by three lunes.

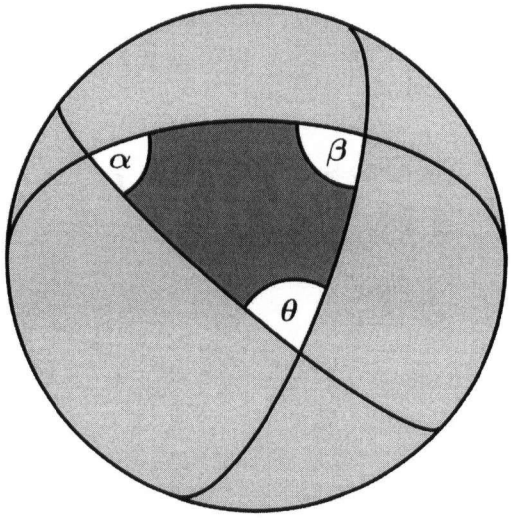

Hence, the sum of the areas of the three double lunes must equal the area of the sphere plus four times the area of the spherical triangle - i.e.

$$4\alpha a^2 + 4\beta a^2 + 4\theta a^2 = 4\pi a^2 + 4A.$$

It follows that

$$a^2(\alpha + \beta + \theta) = \pi a^2 + A$$

$$\Rightarrow \qquad A = a^2(\alpha + \beta + \theta - \pi)$$

■

C.2 Generalization of Girard's theorem to arbitrary polygons

The surface area of an N-sided spherical convex polygon with angles $\alpha_1, \alpha_2, ..., \alpha_N$ (measured in radians) is

$$A = a^2\left(\sum_{i=1}^{N} \alpha_i + (2-N)\pi\right) \tag{C.3}$$

where a is the radius of the sphere.

Proof

Pick an interior point inside the polygon and form N spherical triangles, each with two vertices along the same edge of the polygon and the third vertex as the central point P. Then the area of the spherical polygon is the sum of the areas of these N spherical triangles.

Let γ_i $(i = 1, 2, ..., N)$ be an angle of spherical triangle i at one of the vertices other than P, let η_i be the angle at the other non-P vertex of triangle i, and let β_i be the angle at P of triangle i. Then

$$\sum_{i=1}^{N} (\gamma_i + \eta_i) = \sum_{i=1}^{N} \alpha_i$$

and

$$\sum_{i=1}^{N} \beta_i = 2\pi .$$

Also, by Girard's theorem, the area of spherical triangle i is

$$A_i = a^2(\gamma_i + \eta_i + \beta_i - \pi).$$

It follows that the area of the spherical polygon

$$
\begin{aligned}
A &= \sum_{i=1}^{N} A_i \\
&= \sum_{i=1}^{N} a^2(\gamma_i + \eta_i + \beta_i) \\
&= a^2\left(\sum_{i=1}^{N}(\gamma_i + \eta_i) + \sum_{i=1}^{N}\beta_i - N\pi\right) \\
&= r^2\left(\sum_{i=1}^{N}\alpha_i + 2\pi - N\pi\right) \\
&= a^2\left(\sum_{i=1}^{N}\alpha_i + (2-N)\pi\right)
\end{aligned}
$$

■

C.3 Theorem

Define a room, receiver position, and source position. Then for two impulsive (omni-directional, point) signals defined by

$$s_1'(t) = \begin{cases} W_1 & \text{for } t = 0 \\ 0 & \text{for } t \neq 0 \end{cases} \quad \text{and} \quad s_2'(t) = \begin{cases} W_2 & \text{for } t = 0 \\ 0 & \text{for } t \neq 0 \end{cases}$$

the corresponding radiation densities, $B_1(r,t)$ and $B_2(r,t)$ (from the solution to Eq. (2.7)) are related as $B_2(r,t) = kB_1(r,t)$, where $k = \dfrac{W_1}{W_2}$ (for $t \geq 0$).

Proof (by strong induction)

The theorem holds for $t = 0$ since $B_1(r,t) = 0 = B_2(r,t)$. This is clear from the fact that, with the source inside the room, sound energy has not had time to travel to any part of the boundary of the enclosure.

It is clear, from Eq. (2.11), that

$$B_{d_2}(r,t) = kB_{d_1}(r,t) \text{ for all } t \geq 0 \tag{C.4}$$

Let $t_0 > 0$ and assume that the theorem holds for all t such that $0 \leq t < t_0$ - i.e. assume $B_2(r,t) = kB_1(r,t)$ for all $0 \leq t < t_0$. Then

$$B_2(r,t_0) = \frac{\rho(r)}{\pi}\int_S B_2(r',t_0 - R/c)e^{-mR}\frac{\cos\theta\cos\theta'}{R^2}dS' + B_{d_2}(r,t_0)$$

$$= \frac{\rho(r)}{\pi}\int_S kB_1(r',t_0 - R/c)e^{-mR}\frac{\cos\theta\cos\theta'}{R^2}dS' + kB_{d_1}(r,t_0)$$

$$= k\left[\frac{\rho(r)}{\pi}\int_S B_1(r',t_0 - R/c)e^{-mR}\frac{\cos\theta\cos\theta'}{R^2}dS' + B_{d_1}(r,t_0)\right] = kB_1(r,t_0)$$

as required.

■

APPENDIX D

Code

The numerical solution to the integral equation was implemented in *MATLAB* [44] Version 6 Release 12. The *MATLAB* M-files that were written to give the solution can be categorized into three modules, which are outlined below. The first module is used to input and read the room specifications and conditions. The second module finds the radiation densities of the patches and is independent of the receiver. The third module completes the solution by finding signal responses and parameters, and plots the results for the receiver position. The M-Files are run in the order presented in Table D.1, with each routine using the output from the previous files.

Table D.1. List and description of *MATALB* M-files.

Module	M-File	Description
1	radiosity_input.m	Used to specify the time discretization resolution and the maximum time, source position and power, air absorption exponent, and the speed of sound
	helios_read.m	Reads the output from *HeliosFF* into *MATLAB*. Patch and element vertices, centers, areas, normals, and reflection coefficients are read, as well as patch-to-element form factors.
2	source.m	Calculates the direct contribution of the source to the element radiation densities as given by Eq. (3.5).
	radiosity_network.m	Calculates the radiation densities of the elements by the algorithm outlined in Sections 3.4.
3	receive.m	Uses the second algorithm in Section 3.4 to calculate the pressure squared response at a given receiver position.
	parameters.m	The output from receive.m is used to get the impulse response, echogram, and decay curve, as well as *SPL*, T_{60}, *EDT*, C_{80}, D_{50}, *TS*, and *G* (see Chapter 4).
	figures.m	Plots the echogram and the decay curve.

One other M-File, named 'solid_angles.m', is called by 'source.m' and 'receive.m' to find the solid angles subtended by the source/receiver and the elements. It makes use of the method outlined in Section 3.3.